DESIGN AND OPTIMIZATION OF NANOANTENNAS FOR NANO-OPTICAL APPLICATIONS

A THESIS SUBMITTED TO
THE GRADUATE SCHOOL OF NATURAL AND APPLIED SCIENCES
OF
MIDDLE EAST TECHNICAL UNIVERSITY

BY

GÖKTUĞ IŞIKLAR

IN PARTIAL FULFILLMENT OF THE REQUIREMENTS
FOR
THE DEGREE OF MASTER OF SCIENCE
IN
ELECTRICAL AND ELECTRONICS ENGINEERING

SEPTEMBER 2020

Approval of the thesis:

DESIGN AND OPTIMIZATION OF NANOANTENNAS FOR NANO-OPTICAL APPLICATIONS

submitted by **GÖKTUĞ IŞIKLAR** in partial fulfillment of the requirements for the degree of **Master of Science in Electrical and Electronics Engineering Department, Middle East Technical University** by,

Prof. Dr. Halil Kalıpçılar
Dean, Graduate School of **Natural and Applied Sciences** _____

Prof. Dr. İlkay Ulusoy
Head of Department, **Electrical and Electronics Engineering** _____

Assoc. Prof. Dr. Özgür Ergül
Supervisor, **Electrical and Electronics Engineering, METU** _____

Examining Committee Members:

Prof. Dr. Mustafa Kuzuoğlu
Electrical and Electronics Engineering, METU _____

Assoc. Prof. Dr. Özgür Ergül
Electrical and Electronics Engineering, METU _____

Prof. Dr. Gülbin Dural
Electrical and Electronics Engineering, METU _____

Prof. Dr. Özlem Aydın Çivi
Electrical and Electronics Engineering, METU _____

Prof. Dr. Vakur Behçet Ertürk
Electrical and Electronics Engineering, Bilkent University _____

Date: 02.09.2020

I hereby declare that all information in this document has been obtained and presented in accordance with academic rules and ethical conduct. I also declare that, as required by these rules and conduct, I have fully cited and referenced all material and results that are not original to this work.

Name, Surname: Göktuğ Işıklar

Signature :

ABSTRACT

DESIGN AND OPTIMIZATION OF NANOANTENNAS FOR NANO-OPTICAL APPLICATIONS

Işıklar, Göktuğ
M.S., Department of Electrical and Electronics Engineering
Supervisor: Assoc. Prof. Dr. Özgür Ergül

September 2020, 105 pages

In this study, design and simulation of plasmonic nanoantenna structures to obtain high power enhancement capabilities at optical frequencies, as well as utilization of nanoantennas for imaging and sensing applications are presented. Plasmonic characteristics of nanoantennas, which depend on many parameters, such as material, frequency, geometry, and size, are investigated in detail via computational analyses of various nanoantenna structures. Numerical solutions of electromagnetic problems are performed by using surface-integral-equation formulations that are suitable for plasmonic objects, while the simulations are accelerated, where necessary, by employing the multilevel fast multipole algorithm. Various nanoantenna designs, including slitted structures and novel geometries obtained via shape optimization, are studied and compared with each other and with examples from the literature. Numerical analyses demonstrate superior properties of different nanoantenna designs depending on the frequency. In order to exemplify the applications that nanoantennas can be used for practical purposes, plasmonics structures with high optical sensitivities are designed by using bowtie geometries for particle sensing and nano-optical imaging applications. In this context, computational analyses of detection of nanoparticles

with different shapes, sizes, and electrical properties are presented. Numerical results demonstrate the feasibility of particle detection and identification with both nanoantenna arrays and improved nano-holes.

Keywords: Nanoantennas, Plasmonics, Nano-Optical Sensors, Nano-Optical Imaging, Electromagnetic Scattering, Method of Moments, Multilevel Fast Multipole Algorithm, Genetic Algorithms

ÖZ

NANO-OPTİK UYGULAMALAR İÇİN NANOANTEN TASARIMI VE OPTİMİZASYONU

Işıklar, Göktuğ
Yüksek Lisans, Elektrik ve Elektronik Mühendisliği Bölümü
Tez Yöneticisi: Doç. Dr. Özgür Ergül

Eylül 2020 , 105 sayfa

Bu çalışmada, plazmonik nanoanten yapılarının optik frekanslarında yüksek güç artırımı kabiliyetinin elde edilmesi doğrultusudan tasarımları ve benzetimleriyle birlikte, nanoantenlerin görüntüleme ve algılama uygulamaları için kullanılması sunulmuştur. Malzeme, frekans, geometri ve boyut gibi birçok parametreye bağlı olan nanoantenlerin plazmonik özellikleri, çeşitli nanoanten yapıların hesaplamalı analizleriyle araştırılmıştır. Elektromanyetizma problemlerinin sayısal çözümleri plazmonik nesneler için uygun olan yüzey integral denklemi formülasyonlarıyla gerçekleştirilirken, gerektiğinde benzetimlerin hızlandırılması çok seviyeli hızlı çoklu kutup algoritması ile sağlanmıştır. Kesikli yapılar ve şekil optimizasyonu ile elde edilen özgün geometriler de dahil olmak üzere çeşitli nanoanten tasarımları ele alınmış, bu yapılar hem birbirleriyle hem de literatürdeki mevcut tasarımlarla karşılaştırılmıştır. Sayısal analizler, frekansa bağlı olarak, farklı nanoanten tasarımlarının üstün özelliklerini göstermektedir. Nanoantenlerin pratik olarak kullanıldığı uygulamalara örnek olarak, parçacık algılama ve nano-optik görüntüleme için uygun ve optik hassasiyeti yüksek, papyon geometrilerden oluşan plazmonik yapılar tasarlanmıştır. Bu kapsamda, farklı şekil,

boyut ve elektriksel özelliklere sahip nanoparçacıkların saptanmasının hesaplamalı analizleri sunulmuştur. Sayısal sonuçlar, hem nanoanten dizileriyle hem de iyileştirilmiş nano-delik tasarımlarıyla parçacık algılama ve tanımlamanın mümkün olduğunu göstermektedir.

Anahtar Kelimeler: Nanoantenler, Plazmonik, Nano-Optik Sensörler, Nano-Optik Görüntüleme, Elektromanyetik Saçılım, Momentler Yöntemi, Çok Seviyeli Hızlı Çokkutup Yöntemi, Genetik Algoritmalar

to my beloved family...

ACKNOWLEDGMENTS

First of all, I would like to thank my supervisor, Assoc. Prof. Dr. Özgür Ergül for his support, guidance, and assistance during my thesis studies. It has been a great privilege for me to work with him, and I will always be grateful for everything I have learned from my mentor throughout the master studies.

I would also like to thank Prof. Dr. Mustafa Kuzuoğlu, Prof. Dr. Gülbin Dural, Prof. Dr. Özlem Aydın Çivi, and Prof. Dr. Vakur Behçet Ertürk for their participation in my thesis committee, valuable comments, and suggestions.

I would like to thank TÜBİTAK for 2210-A scholarship program as the financial support during my Master's study.

I would like to express my gratitude to all CEMMETU group members for their great collaboration, inspiration, and support. Special thanks go to Sadri Güler, Barışcan Karaosmanoğlu, Hande İbili, Özgür Eriş, Gökhan Karaova, Şirin Yazar, Zeina El-Ahdab, Aşkın Altınoklu, Türker Dolapçı, Gülten Onay, Mustafa Algun, İsa Can Çetin, and Burak Cihan.

I would like to thank Cengiz Özbek for his constant support and encouragement. I would also like to thank Furkan Özdemircan, Mert Belörenoğlu, and Kaan Arda for their great companionship.

My last thanks go to my mother and father. Words are not enough to express my gratitude for their endless support, encouragement, and love.

TABLE OF CONTENTS

ABSTRACT v

ÖZ vii

ACKNOWLEDGMENTS x

TABLE OF CONTENTS xi

LIST OF TABLES xiv

LIST OF FIGURES xv

LIST OF ABBREVIATIONS xxiii

CHAPTERS

1 INTRODUCTION 1

2 SIMULATIONS OF NANOANTENNAS 7

2.1 Simulation Method 7

2.1.1 Surface Integral Equations 7

2.1.2 Surface Formulations 12

2.1.3 Method of Moments and Discretization 14

2.1.4 Multilevel Fast Multipole Algorithm 17

2.2 Modeling Plasmonic Structures 19

2.2.1 Metals at Optical Frequencies 19

2.2.2 Comparison of SIE Formulations for Plasmonic Structures . . 20

2.3 Concluding Remarks 25

3 DESIGN AND SIMULATION OF NANOANTENNAS FOR HIGH POWER ENHANCEMENT CHARACTERISTICS 27

3.1 Simulation Techniques 27

3.1.1 Details of Simulation Environment 27

3.1.2 Implementation of Genetic Algorithms for Shape Optimization 29

3.2 Numerical Analyses of Design Parameters 30

3.2.1 The Effect of the Material Used 31

3.2.2 The Effect of the Nanoantenna Shape 32

3.2.3 The Effect of Smoothing 33

3.2.4 The Effect of the Gap Size 34

3.2.5 The Effect of the Thickness 35

3.2.6 The Effect of the Size 36

3.2.7 The Effect of the Substrate 39

3.3 Numerical Analysis of Slitted Nanoantenna Designs with Multiband Characteristics 40

3.4 Shape Optimization of Nanoantennas 44

3.5 Comparison of Nanoantenna Designs 57

3.6 Concluding Remarks 62

4 DESIGN AND SIMULATION OF NANOANTENNA-BASED PLASMONIC STRUCTURES FOR IMAGING AND SENSING APPLICATIONS 67

4.1 Nanoantenna Arrays for Particle Detection 67

4.1.1 Simulation Environment 68

4.1.2 Periodicity of Elements 68

4.1.3 Plasmonic Nanoparticle Detection 69

4.1.4 Detection of Dielectric Particles 73

4.1.5 Improved Identification of Dielectric Particles by Background Substraction 77

4.2 Improved Nano-optical Traps for Single-Particle Sensing Applications 83

4.2.1 Simulations of Nano-Holes 83

4.2.2 Improved Nano-hole Designs 83

4.3 Concluding Remarks 95

5 CONCLUSION 97

REFERENCES 101

LIST OF TABLES

TABLES

Table 2.1 Real and imaginary parts of relative permittivity values of Ag obtained by Lorentz-Drude model with respect to frequency. 23

Table 3.1 Design parameters of simple bowtie and square nanoantenna geometries, and their frequency-dependent power enhancing characteristics. . 61

Table 3.2 Design parameters of optimum bowtie nanoantenna geometries, and their frequency-dependent power enhancing characteristics. 62

Table 3.3 Design parameters of optimum square nanoantenna geometries, and their frequency-dependent power enhancing characteristics. 63

Table 3.4 Design parameters of slitted bowtie nanoantenna geometries, and their frequency-dependent power enhancing characteristics. 64

Table 3.5 Design parameters of nanoantenna geometries taken from the literature, and their frequency-dependent power enhancing characteristics.. . . 65

LIST OF FIGURES

FIGURES

Figure 2.1 Relative complex permittivity of Ag with respect to frequency. . 21

Figure 2.2 Relative complex permittivity of Au with respect to frequency. . 22

Figure 2.3 Bistatic far-zone electric field values scattered from a Ag sphere with λ diameter from 250 THz to 750 THz. The relative permittivity of Ag changes from $-60.6667 + 4.3025i$ to $-3.3030 + 0.5769i$. 23

Figure 2.4 The relative error (in percentage) in the numerical solutions depicted in Figure 2.3 with respect to the corresponding Mie-series solutions (left) and the required number of GMRES iterations (right). 24

Figure 3.1 A bowtie nanoantenna (left) and power enhancement factor at its gap when different materials are used (right). 31

Figure 3.2 Power enhancement factor with respect to the frequency is given when different nanoantenna shapes are used. 32

Figure 3.3 Curved bowtie geometries ($100 \times 100 \times 20$ nm arms and 10 nm gap size) with minimum and maximum ROC values (left) and frequency-dependent enhancement factor values for Ag nanoantennas with $2, 3, 4,$ and 5 nm ROC values (right). 33

Figure 3.4 Curved bowtie geometries ($100 \times 100 \times 20$ nm arms, 2 nm ROC, and 10 nm gap size) with minimum and maximum gap sizes (left) and frequency-dependent enhancement factor values for Ag nanoantennas with $10, 15, 20,$ and 25 nm gap sizes (right). 34

Figure 3.5 Frequency-dependent enhancement factor values for Ag bowtie nanoantennas with $20, 30,$ and 40 nm thicknesses. 35

Figure 3.6 Bowtie geometries B1, B2, and B3 with single arm dimensions of $100 \times 100 \times 20$ nm, $125 \times 125 \times 20$ nm, and $150 \times 150 \times 20$ nm, respectively. The gap size is fixed to 30 nm. 37

Figure 3.7 Frequency-dependent enhancement factor values of Au (solid lines) and Ag (dashed line) bowtie nanoantenna geometries B1, B2, and B3. 37

Figure 3.8 The generic shape of square nanoantennas (left) and frequency-dependent enhancement factor curves for Au and Ag S1, S2, and S3 designs (right). 38

Figure 3.9 B1 nanoantenna geometry ($100 \times 100 \times 20$ nm) with silicon substrate ($300 \times 300 \times 50$ nm) and chrome layer ($100 \times 100 \times 2$ nm. . 39

Figure 3.10 Frequency-dependent enhancement factors of Au bowtie nanoantennas B1, B2, and B3 with silicon substrates and chrome layers. 40

Figure 3.11 Slitted B1 geometry with varying slit width (left) and frequency-dependent enhancement factor values of slitted and ordinary Ag B1 geometries (right). 41

Figure 3.12 Slitted B1 geometry with varying slit positions (left) and frequency-dependent enhancement factor values of slitted and ordinary Ag B1 geometries (right). 42

Figure 3.13 Same-side slitted (BSS1) and opposite-side slitted (BOS1) geometries (left) and frequency-dependent enhancement factor values of slitted Ag and Au B1, B2, and B3 geometries (right). 43

Figure 3.14 Opposite-side slitted square geometry SS1 and double-side slitted square geometry SDS (left), and frequency-dependent enhancement factor values of slitted Au SS1, SS2, SS3, and SDS geometries and Ag SS1, SS2, and SS3 geometries (right). 44

Figure 3.15 Selected deformation surfaces; upper surface at $z = 10$ nm shown with orange color for B1 (left) and side surface at $y = -50$ nm shown with orange color for S1 (right). 46

Figure 3.16 Cost function values versus generations for three optimization sets at 360 THz (left); trimetric and side views of the optimal geometries BO_{11}, BO_{21}, and BO_{31}, respectively, from top to bottom (right). 47

Figure 3.17 Cost function values versus generations for three optimization sets at 415 THz (left); trimetric and side views of the optimal geometries BO_{12}, BO_{22}, and BO_{32}, respectively, from top to bottom (right). 47

Figure 3.18 Cost function values versus generations for three optimization sets at 500 THz (left); trimetric and side views of the optimal geometries BO_{13}, BO_{23}, and BO_{33}, respectively, from top to bottom (right). 48

Figure 3.19 Cost function values versus generations for three optimization sets at 400-430 THz (left); trimetric and side views of the optimal geometries BO_{14}, BO_{24}, and BO_{34}, respectively, from top to bottom (right). 49

Figure 3.20 Frequency-dependent enhancement factor values for optimal geometries of the first optimization set (left), the second optimization set (middle), and the third optimization set (right) , in comparison to the enhancement of the original B1 geometry. 50

Figure 3.21 Trimetric views of the optimal geometries SO_1, SO_2, and SO_3 (top); cost function values with respect to generations for the optimal geometries with the same order (bottom). 51

Figure 3.22 Trimetric views of the optimal geometries SO_4, SO_5, SO_6, and SO_7 (top); cost function values with respect to generations for the optimal geometries with the same order (bottom). 53

Figure 3.23 Frequency-dependent enhancement factor values for the optimal geometries of the single-frequency optimization trials (left) and the optimal geometries of the multi-frequency optimization trials (right) on the original S1 geometry. 54

Figure 3.24 Near-zone enhancement characteristics of B1, BO_{31}, BO_{34}, BO_{32}, and BO_{33} geometries at $360, 400, 415, 430$, and 500 THz. 55

Figure 3.25 Near-zone enhancement characteristics of S1, SO_1, SO_2, and SO_3 geometries at $360, 415$, and 500 THz. 56

Figure 3.26 Near-zone enhancement characteristics of S1, SO_5, SO_6, SO_4, and SO_7 geometries at $350, 380, 400, 430, 450, 480$, and 560 THz. 57

Figure 3.27 Top view of geometries LD24, LD26, and LD26-2 (top) frequency-dependent enhancement factor values (bottom). 58

Figure 3.28 Top view of geometries LB33, LB37, and LD7 (top) frequency-dependent enhancement factor values (bottom). 59

Figure 3.29 Top view of geometries LB14, LD14, LD18, and LD18-2 (top) frequency-dependent enhancement factor values (bottom). 59

Figure 3.30 Top view of geometries LD13, LB3, LBD3-2, and LB11 (top) frequency-dependent enhancement factor values (bottom). 60

Figure 4.1 Frequency-dependent enhancement factor at the gap of an Ag bowtie nanoantenna, when another identical nanoantenna is placed at different nearby locations. 69

Figure 4.2 Frequency-dependent enhancement factor at the gap of an Ag bowtie nanoantenna in an arrangement of 2×2 nanoantennas with different periodicities. 70

Figure 4.3 Near-zone characteristics of an array of 3×3 nanoantennas when Ag particles with different sizes are located in the array plane. The periodicity of the array is 500 nm, while the particle diameter changes from 50 nm to 300 nm (for the first three locations) or from 50 nm to 250 nm (for the last two locations). 71

Figure 4.4 Movement of a spherical particle of diameter 600 nm above a 5×5 array of nanoantennas with 475 nm periodicity. Moving on a path between two rows (left). Moving on a path above the first row of nanoantennas (right). 72

Figure 4.5 Near-zone characteristics of an array of 5×5 nanoantennas when an Ag particle of diameter 600 nm moves above the array as described in Figure 4.5 (left). The periodicity of the array is 475 nm. The bottom of the particle is 10 nm away from the top surface of the nanoantennas. . 72

Figure 4.6 Near-zone characteristics of an array of 5×5 nanoantennas when an Ag particle of diameter 600 nm moves above the array as described in Figure 4.5 (right). The periodicity of the array is 475 nm. The bottom of the particle is 10 nm away from the top surfaces of the nanoantennas. 73

Figure 4.7 Near-zone characteristics of an array of 3×3 nanoantennas when dielectric particles of diameter 300 nm are located above the array. The periodicity of the array is 475 nm. The particles are 90 nm away from the top surfaces of the nanoantennas. 74

Figure 4.8 Near-zone characteristics of an array of 3×3 nanoantennas when dielectric particles with different sizes (25-300 nm diameter) and permittivity values of 4,6, and 8 are located above the array between middle and bottom rows. The distance between the particles and surfaces of nanoantennas is 20 nm. 75

Figure 4.9 Near-zone characteristics of an array of 3×3 nanoantennas when dielectric particles (with $\epsilon_r = 3, 6, 10$) of diameter 300 nm are located above the array. The periodicity of the array is 475 nm. The particles are 90 nm away from the top surfaces of the nanoantennas. 76

Figure 4.10 An array of 3×3 nanoantennas when dielectric particles with sphere, cube, cylinder, cone 1, cone 2, and star shapes are located above the array. 77

Figure 4.11 Near-zone characteristics of an array of 3×3 nanoantennas when dielectric particles with different shapes are located above the array. The periodicity of the array is 475 nm. The particles are 50 nm away from the top surfaces of the nanoantennas, while their relative permittivity is 8. 77

Figure 4.12 Dielectric particle located above an array of 3×3 nanoantennas and the sampling planes located at $z = -20$ nm and $z = 400$ nm. 78

Figure 4.13 Intensity, density, enhancement, and difference factor distributions on the $z = -20$ nm plane for the scenarios depicted in Figure 4.10. 79

Figure 4.14 Intensity, density, enhancement, and difference factor distributions on the $z = 400$ nm plane for the scenarios depicted in Figure 4.10. 80

Figure 4.15 Difference factor distributions (on the $z = 400$ nm and $z = -20$ planes) for sphere particles with different relative permittivities above an 3×3 nanoantenna array (such as depicted in Figure 4.12). 81

Figure 4.16 Difference factor distributions (on the $z = 400$ nm and $z = -20$ planes) for sphere particles with different sizes above an 3×3 nanoantenna array (such as depicted in Figure 4.12). 82

Figure 4.17 Difference factor distributions (on the $z = 400$ nm and $z = -20$ planes) for sphere particles with different positions above an 3×3 nanoantenna array (such as depicted in Figure 4.12). 82

Figure 4.18 Six different improved nano-hole designs that are sensitive to nanoparticles. 84

Figure 4.19 Frequency-dependent power enhancement factors for the six different nano-hole designs in Figure 4.18. 85

Figure 4.20 Cylindrical nanoparticles located at the gap locations of Design 1, Design 3, and Design 4. 86

Figure 4.21 Far-zone electric field intensity with respect to frequency scattered from Design 1, Design 3, and Design 4, with and without cylindrical Ag nanoparticles. In addition to backscattered intensity values (first row), results for 30° off-axis side-scattering (second row) are considered. 87

Figure 4.22 Electric field intensity values with and without cylindrical Ag nanoparticles for Design 3 and for a circular nano-hole. For each nano-hole, in addition to backscattering values (left), difference values (right) that are obtained by taking the difference of backscattering values obtained with and without the nanoparticle are shown. 88

Figure 4.23 Electric field intensity values with and without cylindrical dielectric nanoparticles for Design 3 and a circular nano-hole. For both nano-holes, in addition to backscattering values (left), difference values (right) that are obtained by taking the difference of backscattering values obtained with and without the nanoparticle are shown. 89

Figure 4.24 Electric field intensity values with and without cylindrical dielectric nanoparticles for Design 3. Three different permittivity values are considered. 89

Figure 4.25 Electric field intensity values with and without dielectric nanoparticles for Design 3. Two different geometries are considered, while the relative permittivity is set to 8. 90

Figure 4.26 Electric field intensity values with and without the off-center-located dielectric nanoparticles for Design 3 (nanotrap) and circular nano-hole. Two different particles are considered, while the refractive index is set to 2. 91

Figure 4.27 Intensity difference values for dielectric nanoparticles that are located off-center inside Design 3 (nanotrap) and circular nano-hole. Two different particles are considered, while the refractive index is set to 2. 92

Figure 4.28 Three different particles that can fit into a cylinder of 60 nm height and 8 nm diameter, and the setups to detect them. 93

Figure 4.29 Electric field intensity values with and without Particle 1, Particle 2, and Particle 3 for Design 3. For each case, in addition to backscattering values (left), difference values (right) that are obtained by evaluating the difference of backscattering values obtained with and without the nanoparticles are shown. 93

Figure 4.30 Near-zone electric field characteristics of the improved nano-hole structure (Design 3) without particle (top row), Particle 1 (second row), Particle 2 (third row), and Particle 3 (last row). The particles are located at the center. 94

Figure 4.31 Near-zone electric field intensity difference characteristics of the improved nano-hole structure (Design 3) with Particle 1 (top row), Particle 2 (second row), and Particle 3 (last row). The particles are located at the center. 95

LIST OF ABBREVIATIONS

CTF	Combined tangential formulation
EFIE	Electric-field integral equation
GA	Genetic algorithm
GMRES	Generalized minimal residual
JMCFIE	Electric and magnetic current combined-field integral equation
MCTF	Modified combined tangential formulation
MFIE	Magnetic-field integral equation
MLFMA	Multilevel fast multipole algorithm
MOM	Method of moments
PMCHWT	Poggio-Miller-Chang-Harrington-Wu-Tsai
ROC	Radius of curvature
RWG	Rao-Wilton-Glisson
SIE	Surface integral equation

CHAPTER 1

INTRODUCTION

When light interacts with metallic structures, strong oscillations occur due to the movement of free electrons on metals. These oscillations, known as localized surface plasmons, are studied extensively in the science of plasmonics. In recent years, the increasing interest in plasmonics has been accompanied by rapid developments in fabrication techniques, leading to a widespread study of unique characteristics of nanostructures [1]. Thanks to their extensive ability of trapping and focusing electromagnetic waves in subwavelength regions, nanoantennas have been among the most attractive of such metallic structures to manipulate light [2]. This light manipulation can take two forms: Enhancing the localized electromagnetic field intensity on metallic surfaces, i.e., creating hot spots, or emitting light waves in particular directions. Plasmonic nanoantennas can be used in many applications, such as energy harvesting [3, 4], nano-optical focusing [5, 6], nano-optical wireless networks [7, 8], as well as bio-sensing [9, 10, 11, 12]. Since nanoantennas' structural properties to achieve desired plasmonic effects, while considering fabrication cost and feasibility are not well known, extensive studies are needed to design them for given applications. In this study, various nanoantennas are designed to obtain strong enhancement in hot spots in the near-infrared and visible-light spectra.

Although nanoantennas are named after the conventional antennas due to their similarities, there are many fundamental differences between them. Similar to their radio-frequency counterparts, nanoantennas successfully achieve electromagnetic transmission in both near-field and far-field regimes. Besides, some well-known antenna shapes can be used to design nanoantennas with similar operational properties. For example, Yagi-Uda nanoantennas have the ability of directional radiation [5], while

bowtie-shaped nanoantennas are used for wideband responses [13]. On the other hand, at optical frequencies, metals do not behave as perfect electric conductors [14]. Therefore, nanoantennas should be considered, analyzed, and modeled as penetrable structures, unlike radio-frequency antennas. In addition, the penetrable model itself depends on the frequency, which further complicates nanoantenna analyses. For example, scaling a nanoantenna causes a shift in its resonance frequency, as in conventional antennas, while it is not easy to predict its actual response due to rapid changes in the electrical properties of metals with respect to the frequency. Consequently, numerous simulations are required to design optimal nanoantennas; however, their sensitive electromagnetic responses make nanoantennas challenging to analyze via computational methods.

Considering the challenges briefly mentioned above, a full-wave electromagnetic solver is developed in this study to simulate plasmonic behaviors of metals at optical frequencies. Lorentz-Drude model [15] is used to represent metals as penetrable structures with varying permittivity values in the frequency domain. Scattering problems are analyzed by using surface-integral-equation (SIE) formulations considering piecewise homogeneous models of plasmonic materials. Among various formulations, the modified combined tangential formulation (MCTF), which was developed for accurate analyses of penetrable objects with negative real permittivity, stands out in terms of both accuracy and computational cost [16]. Nanoantenna geometries and MCTF are discretized by using the Rao-Wilton-Glisson (RWG) basis functions [17] to obtain matrix equations. The multilevel fast multipole algorithm (MLFMA) [18] is employed for accelerating solutions of problems involving large numbers of unknowns. By means of accurate simulations of finite structures, various design parameters, such as material, geometry, and dimensions, are investigated in detail for reaching optimal nanoantenna configurations.

Optimal arrangements of nanoantennas strongly depend on the selected shape, size, and material of each nanoantenna, as well as the operating frequency [19]. In these arrangements, it is usually aimed to increase the enhancement factor, which is defined as the ratio of the power density localized inside a subwavelength region in the vicinity of a nanoantenna to the power density of the incident light wave. Due to

their easier fabrication, basic bowtie structures are frequently used in the literature. In fact, despite their relatively simple geometries, bowtie nanoantennas can create intense hot spots at their feed gaps, thanks to their symmetrically located sharp tips [20]. The chosen material and size of a nanoantenna directly affect the resonance frequency range, where electromagnetic fields are sharply focused. In the case of bowtie nanoantennas, the gap size between the tips is one of the main factors for the intensity of hot spots. Although the principal purpose is to produce sharp-tip bowties, curved tips are often encountered in fabricated samples, leading to deteriorated enhancement factors. In addition to high enhancement factors that are commonly studied in the literature, multiband and wideband frequency responses of nanoantennas are further investigated in this study. Such nanoantennas with multiband or wideband characteristics can provide extensive ability in molecule labeling for bio-sensing and in energy harvesting for solar-cell applications. We show that, among alternative designs, slitted structures demonstrate excellent multiband responses. Effects of slit position and width on frequency responses are particularly investigated for better performance. As a major contribution of this thesis, shape optimization is used to generate superior designs with high enhancement factors for both single-frequency and multi-frequency (including wideband) operations. For this purpose, the developed solver is integrated into an in-house implementation of genetic algorithms.

Nanoantennas can be excellent tools to detect metallic and dielectric nanoparticles for imaging and sensing applications [21]. Specifically, with their strong near-zone coupling properties, nanoantennas may enable tracking single nanoparticles, even of subwavelength sizes, at optical frequencies. Basically, the electromagnetic field intensity in the hot spot of a nanoantenna can be sensitive to a nearby particle in the same environment. Therefore, detection of a particle can be possible by observing fluctuations in the hot spots. In this study, we present computational analyses of nanoantenna arrays when they are used to detect and identify nearby nanoparticles. Similar to single nanoantenna problems mentioned above, solutions of frequency-domain scattering problems are performed by using a SIE formulation that is suitable for composite structures involving metallic, dielectric, and/or plasmonic objects. Acceleration is further achieved via MLFMA developed for composite structures. Besides the main parameters that affect the enhancement of a nanoantenna, the periodic-

ity in the arrangements of multiple nanoantennas is one of the most important factors when designing effective arrays for detection. Hence, a nanoantenna design with a fixed geometry and material is used to examine distances between nanoantennas to construct small-scale arrays. Numerical results demonstrate the feasibility of particle detection and identification, even with sparse arrays with relatively large periodicities.

In typical single-particle sensing applications, it is desired to detect relatively low-density nanoparticles, which can be achieved optically using scattering properties. Unsurprisingly, in the literature, plasmonic properties of some metals at optical frequencies have been used for this purpose to design highly sensitive nano-optical sensors [22, 23]. For example, nanoantennas with strong power enhancement abilities can be employed to detect nanoparticles entering into their focus regions [2, 9, 11, 12]. In dynamic and uncontrolled scenarios, however, such a sensing structure should be physically convenient for nanoparticles to be collected at the desired locations with reasonable probabilities. For example, a bowtie nanoantenna can provide very high enhancement factors inside the gap between its tips, while it may be difficult to locate nanoparticles at high-enhancement positions. Therefore, researchers are attracted to dual structures, i.e., nano-optical traps, and their arrays to improve the reliability of single-particle sensing. In this thesis, besides nanoantennas, computational design and simulations of effective nano-optical traps are presented. Nano-holes that are not only physically suitable for trapping but also optically sensitive to nanoparticles are designed. This way, a nanoparticle trapped in a designed nano-hole leads to remarkable changes in its electromagnetic responses so that it can easily be detected and even be identified. Extensive numerical simulations show that nano-holes with triangular tips provide excellent results, in comparison to the conventional circular holes [24].

This thesis is divided into chapters according to the studies briefly described above. In Chapter 2, derivations of SIE formulations from Maxwell's equations, their discretizations to obtain matrix equations, and their solutions via MLFMA are explained. Plasmonic modeling of metals at optical frequencies is considered and studied by comparing numerical results of the conventional formulations in terms of accuracy and efficiency. In Chapter 3, effects of nanoantenna design parameters, like material,

shape, and size, on their performances are demonstrated through three-dimensional computational simulations. Multiband characteristics of novel nanoantenna designs achieved by slitting techniques are presented. In addition, shape optimization via genetic algorithms is discussed, together with the resulting nanoantenna designs that provide superior enhancement properties. To demonstrate their favorable properties, our novel designs are further compared against available designs in the literature. In Chapter 4, particle sensing using nanoantenna arrays and nano-hole structures is detailed. Finally, in Chapter 5, we summarize the whole study and emphasize potential future works.

CHAPTER 2

SIMULATIONS OF NANOANTENNAS

The details of the numerical solver to analyze electromagnetic problems involving nanoantennas are presented in this chapter. For rigorous simulations of nanoantennas, the most suitable techniques to model plasmonic structures are discussed.

2.1 Simulation Method

In this section, SIE formulations for three-dimensional problems involving penetrable structures are derived from Maxwell's equations. To model nanoantennas in the frequency domain, the use of effective complex permittivity values of metals at optical frequencies are discussed. Furthermore, fundamental concepts related to the discretization of SIE formulations, MOM, and MLFMA are explained.

2.1.1 Surface Integral Equations

Maxwell's equations in time domain can be written in differential forms as

$$\nabla \times \boldsymbol{E}(\boldsymbol{r}, t) = -\frac{\partial \boldsymbol{B}(\boldsymbol{r}, t)}{\partial t} \tag{2.1}$$

$$\nabla \times \boldsymbol{H}(\boldsymbol{r}, t) = \frac{\partial \boldsymbol{D}(\boldsymbol{r}, t)}{\partial t} + \boldsymbol{J}(\boldsymbol{r}, t) \tag{2.2}$$

$$\nabla \cdot \boldsymbol{D}(\boldsymbol{r}, t) = \rho_e(\boldsymbol{r}, t) \tag{2.3}$$

$$\nabla \cdot \boldsymbol{B}(\boldsymbol{r}, t) = 0, \tag{2.4}$$

where $\boldsymbol{E}(\boldsymbol{r}, t)$ and $\boldsymbol{H}(\boldsymbol{r}, t)$ are electric and magnetic field intensities, $\boldsymbol{D}(\boldsymbol{r}, t)$ and $\boldsymbol{B}(\boldsymbol{r}, t)$ are electric and magnetic flux densities, $\boldsymbol{J}(\boldsymbol{r}, t)$ is the electric current density,

and $\rho_e(\boldsymbol{r}, t)$ is the electric charge density. In these expressions, $\boldsymbol{r}$ represents the position vector, while t represents time. Using the identity $\nabla \cdot \nabla \times \boldsymbol{f} = 0$, the continuity equation can be verified by taking the divergence of Equation 2.2 as

$$\nabla \cdot \boldsymbol{J}(\boldsymbol{r}, t) = -\frac{\partial \rho_e(\boldsymbol{r}, t)}{\partial t}. \tag{2.5}$$

For an isotropic, linear, and homogeneous medium, the relationships between flux densities and field intensities can be expressed as

$$\boldsymbol{D}(\boldsymbol{r}, t) = \epsilon \boldsymbol{E}(\boldsymbol{r}, t) \tag{2.6}$$

$$\boldsymbol{B}(\boldsymbol{r}, t) = \mu \boldsymbol{H}(\boldsymbol{r}, t). \tag{2.7}$$

Maxwell's equations can be written only in terms of field intensities by using constitutive relations given in Equations 2.6 and 2.7 as

$$\nabla \times \boldsymbol{E}(\boldsymbol{r}, t) = -\mu \frac{\partial \boldsymbol{H}(\boldsymbol{r}, t)}{\partial t} \tag{2.8}$$

$$\nabla \times \boldsymbol{H}(\boldsymbol{r}, t) = \epsilon \frac{\partial \boldsymbol{E}(\boldsymbol{r}, t)}{\partial t} + \boldsymbol{J}(\boldsymbol{r}, t) \tag{2.9}$$

$$\nabla \cdot \boldsymbol{E}(\boldsymbol{r}, t) = \frac{1}{\epsilon} \rho_e(\boldsymbol{r}, t) \tag{2.10}$$

$$\nabla \cdot \boldsymbol{H}(\boldsymbol{r}, t) = 0. \tag{2.11}$$

In the frequency domain, assuming $\exp(-i\omega t)$ time convention, Maxwell's equations and continuity equation are given in terms of phasor quantities as

$$\nabla \times \boldsymbol{E}(\boldsymbol{r}) = i\omega\mu \boldsymbol{H}(\boldsymbol{r}) \tag{2.12}$$

$$\nabla \times \boldsymbol{H}(\boldsymbol{r}) = -i\omega\epsilon \boldsymbol{E}(\boldsymbol{r}) + \boldsymbol{J}(\boldsymbol{r}) \tag{2.13}$$

$$\nabla \cdot \boldsymbol{E}(\boldsymbol{r}) = \frac{1}{\epsilon} \rho_e(\boldsymbol{r}) \tag{2.14}$$

$$\nabla \cdot \boldsymbol{H}(\boldsymbol{r}) = 0 \tag{2.15}$$

$$\nabla \cdot \boldsymbol{J}(\boldsymbol{r}) = i\omega \rho_e(\boldsymbol{r}). \tag{2.16}$$

Maxwell's equations can be extended by adding the magnetic current density $\boldsymbol{M}(\boldsymbol{r})$ and the magnetic charge density $\boldsymbol{\rho}_m(\boldsymbol{r})$ as

$$\nabla \times \boldsymbol{E}(\boldsymbol{r}) = i\omega\mu \boldsymbol{H}(\boldsymbol{r}) - \boldsymbol{M}(\boldsymbol{r}) \tag{2.17}$$

$$\nabla \times \boldsymbol{H}(\boldsymbol{r}) = -i\omega\epsilon \boldsymbol{E}(\boldsymbol{r}) + \boldsymbol{J}(\boldsymbol{r}) \tag{2.18}$$

$$\nabla \cdot \boldsymbol{E}(\boldsymbol{r}) = \frac{1}{\epsilon} \rho_e(\boldsymbol{r}) \tag{2.19}$$

$$\nabla \cdot \boldsymbol{H}(\boldsymbol{r}) = \frac{1}{\mu} \rho_m(\boldsymbol{r}). \tag{2.20}$$

Then, the continuity equations can be expressed for both electric and magnetic sources as

$$\nabla \cdot \boldsymbol{J}(\boldsymbol{r}) = i\omega\rho_e(\boldsymbol{r}) \tag{2.21}$$

$$\nabla \cdot \boldsymbol{M}(\boldsymbol{r}) = i\omega\rho_m(\boldsymbol{r}). \tag{2.22}$$

The field intensities can be written in terms of vector and scalar potentials as

$$\boldsymbol{E}(\boldsymbol{r}) = i\omega\boldsymbol{A}_m(\boldsymbol{r}) - \nabla\phi_e(\boldsymbol{r}) - \frac{1}{\epsilon}\nabla \times \boldsymbol{A}_e(\boldsymbol{r}) \tag{2.23}$$

$$\boldsymbol{H}(\boldsymbol{r}) = i\omega\boldsymbol{A}_e(\boldsymbol{r}) - \nabla\phi_m(\boldsymbol{r}) - \frac{1}{\mu}\nabla \times \boldsymbol{A}_m(\boldsymbol{r}). \tag{2.24}$$

Using the Lorentz gauge, i.e.,

$$\nabla \cdot \boldsymbol{A}_m(\boldsymbol{r}) = i\omega\epsilon\mu\phi_e(\boldsymbol{r}) \tag{2.25}$$

$$\nabla \cdot \boldsymbol{A}_e(\boldsymbol{r}) = i\omega\mu\epsilon\phi_m(\boldsymbol{r}), \tag{2.26}$$

Helmholtz equations for potentials are obtained as

$$\nabla^2\phi_e(\boldsymbol{r}) + k^2\phi_e(\boldsymbol{r}) = -\frac{1}{\epsilon}\rho_e(\boldsymbol{r}) \tag{2.27}$$

$$\nabla^2\phi_m(\boldsymbol{r}) + k^2\phi_m(\boldsymbol{r}) = -\frac{1}{\mu}\rho_m(\boldsymbol{r}) \tag{2.28}$$

$$\nabla^2\boldsymbol{A}_e(\boldsymbol{r}) + k^2\boldsymbol{A}_e(\boldsymbol{r}) = -\epsilon\boldsymbol{M}(\boldsymbol{r}) \tag{2.29}$$

$$\nabla^2\boldsymbol{A}_m(\boldsymbol{r}) + k^2\boldsymbol{A}_m(\boldsymbol{r}) = -\mu\boldsymbol{J}(\boldsymbol{r}), \tag{2.30}$$

where $k = \omega\sqrt{\epsilon\mu} = 2\pi/\lambda$ is the wavenumber and λ is the wavelength. Solutions of these equations for point sources lead to the homogeneous-space Green's function given as

$$g(\boldsymbol{r} - \boldsymbol{r}') = \frac{\exp\left(ik|\boldsymbol{r} - \boldsymbol{r}'|\right)}{4\pi|\boldsymbol{r} - \boldsymbol{r}'|}, \tag{2.31}$$

where $\boldsymbol{r}$ and $\boldsymbol{r}'$ represent observation and source points, respectively. Using the Green's function as a kernel, scalar and vector potentials can be written in terms of sources as

$$\phi_e(\boldsymbol{r}) = \frac{1}{\epsilon}\int d\boldsymbol{r}' g(\boldsymbol{r}, \boldsymbol{r}')\rho_e(\boldsymbol{r}') \tag{2.32}$$

$$\phi_m(\boldsymbol{r}) = \frac{1}{\mu}\int d\boldsymbol{r}' g(\boldsymbol{r}, \boldsymbol{r}')\rho_m(\boldsymbol{r}') \tag{2.33}$$

$$\boldsymbol{A}_e(\boldsymbol{r}) = \epsilon\int d\boldsymbol{r}' g(\boldsymbol{r}, \boldsymbol{r}')\boldsymbol{M}(\boldsymbol{r}') \tag{2.34}$$

$$\boldsymbol{A}_m(\boldsymbol{r}) = \mu\int d\boldsymbol{r}' g(\boldsymbol{r}, \boldsymbol{r}')\boldsymbol{J}(\boldsymbol{r}'). \tag{2.35}$$

Substituting the potential expressions above into Equations 2.23 and 2.24, and with the help of continuity equations, field intensities can be obtained in terms of sources as

$$\boldsymbol{E}(\boldsymbol{r}) = ik\eta \int d\boldsymbol{r}' \left[\boldsymbol{J}(\boldsymbol{r}') + \frac{1}{k^2} \nabla' \cdot \boldsymbol{J}(\boldsymbol{r}') \nabla \right] g(\boldsymbol{r}, \boldsymbol{r}') - \int d\boldsymbol{r}' \nabla g(\boldsymbol{r}, \boldsymbol{r}') \times \boldsymbol{M}(\boldsymbol{r}') \tag{2.36}$$

$$\boldsymbol{H}(\boldsymbol{r}) = ik\eta^{-1} \int d\boldsymbol{r}' \left[\boldsymbol{M}(\boldsymbol{r}') + \frac{1}{k^2} \nabla' \cdot \boldsymbol{M}(\boldsymbol{r}') \nabla \right] g(\boldsymbol{r}, \boldsymbol{r}') + \int d\boldsymbol{r}' \nabla g(\boldsymbol{r}, \boldsymbol{r}') \times \boldsymbol{J}(\boldsymbol{r}'), \tag{2.37}$$

where $\eta = \sqrt{\mu}/\sqrt{\epsilon}$ is the intrinsic impedance. Integro-differential operators can be defined as

$$\boldsymbol{\mathcal{T}}\{\boldsymbol{X}\}(\boldsymbol{r}) = ik \int d\boldsymbol{r}' \left[\boldsymbol{X}(\boldsymbol{r}') + \frac{1}{k^2} \nabla' \cdot \boldsymbol{X}(\boldsymbol{r}') \nabla \right] g(\boldsymbol{r}, \boldsymbol{r}') \tag{2.38}$$

$$\boldsymbol{\mathcal{K}}\{\boldsymbol{X}\}(\boldsymbol{r}) = \int d\boldsymbol{r}' \boldsymbol{X}(\boldsymbol{r}') \times \nabla' g(\boldsymbol{r}, \boldsymbol{r}'), \tag{2.39}$$

leading to more compact expressions for field intensities as

$$\boldsymbol{E}(\boldsymbol{r}) = \eta \boldsymbol{\mathcal{T}}\{\boldsymbol{J}\}(\boldsymbol{r}) - \boldsymbol{\mathcal{K}}\{\boldsymbol{M}\}(\boldsymbol{r}) \tag{2.40}$$

$$\boldsymbol{H}(\boldsymbol{r}) = \eta^{-1} \boldsymbol{\mathcal{T}}\{\boldsymbol{M}\}(\boldsymbol{r}) + \boldsymbol{\mathcal{K}}\{\boldsymbol{J}\}(\boldsymbol{r}). \tag{2.41}$$

The equivalence principle can be used to divide an electromagnetic scattering problem involving penetrable and metallic parts into subproblems by defining equivalence currents on surfaces. Artificial surfaces can be defined on actual surfaces and boundaries in order to benefit from physical boundary conditions. Consider a homogeneous region D_u with permittivity ϵ_u and permeability μ_u, bounded by a surface S_u. The equivalence currents on the surface are defined to support the continuity of the tangential fields as

$$-\boldsymbol{M}_u = \hat{\boldsymbol{n}}_u \times \boldsymbol{E}_u(\boldsymbol{r}) = \hat{\boldsymbol{n}}_u \times \boldsymbol{E}_u^{inc}(\boldsymbol{r}) + \hat{\boldsymbol{n}}_u \times \boldsymbol{E}_u^{sec}(\boldsymbol{r}) \tag{2.42}$$

$$\boldsymbol{J}_u = \hat{\boldsymbol{n}}_u \times \boldsymbol{H}_u(\boldsymbol{r}) = \hat{\boldsymbol{n}}_u \times \boldsymbol{H}_u^{inc}(\boldsymbol{r}) + \hat{\boldsymbol{n}}_u \times \boldsymbol{H}_u^{sec}(\boldsymbol{r}), \tag{2.43}$$

where $\hat{\boldsymbol{n}}_u$ represents the unit vector on the surface, $\boldsymbol{E}_u^{inc}(\boldsymbol{r})$ and $\boldsymbol{H}_u^{inc}(\boldsymbol{r})$ are incident fields created by external sources, and $\boldsymbol{E}_u^{sec}(\boldsymbol{r})$ and $\boldsymbol{H}_u^{sec}(\boldsymbol{r})$ are secondary fields due to the equivalence currents. In these expressions, the secondary electric and magnetic

field intensities can be written in terms of the integro-differential operators as

$$-\boldsymbol{M}_u = \hat{\boldsymbol{n}}_u \times \boldsymbol{E}_u^{inc}(\boldsymbol{r}) + \eta_u \hat{\boldsymbol{n}}_u \times \boldsymbol{\mathcal{T}}_u\{\boldsymbol{J}_u\}(\boldsymbol{r}) - \hat{\boldsymbol{n}}_u \times \boldsymbol{\mathcal{K}}_u\{\boldsymbol{M}_u\}(\boldsymbol{r}) \tag{2.44}$$

$$\boldsymbol{J}_u = \hat{\boldsymbol{n}}_u \times \boldsymbol{H}_u^{inc}(\boldsymbol{r}) + \eta_u^{-1} \hat{\boldsymbol{n}}_u \times \boldsymbol{\mathcal{T}}_u\{\boldsymbol{M}_u\}(\boldsymbol{r}) + \hat{\boldsymbol{n}}_u \times \boldsymbol{\mathcal{K}}_u\{\boldsymbol{J}_u\}(\boldsymbol{r}). \tag{2.45}$$

We note that the integro-differential operators in Equations 2.44 and 2.45 related to region D_u can be written as

$$\boldsymbol{\mathcal{T}}_u\{\boldsymbol{X}\}(\boldsymbol{r}) = ik_u \int_{S_u} d\boldsymbol{r}' \left[\boldsymbol{X}(\boldsymbol{r}') + \frac{1}{k_u^2} \nabla' \cdot \boldsymbol{X}(\boldsymbol{r}') \nabla \right] g_u(\boldsymbol{r}, \boldsymbol{r}') \tag{2.46}$$

$$\boldsymbol{\mathcal{K}}_u\{\boldsymbol{X}\}(\boldsymbol{r}) = \boldsymbol{\mathcal{K}}_u^{PV}\{\boldsymbol{X}\}(\boldsymbol{r}) - \frac{4\pi - \Omega_u}{4\pi} \hat{\boldsymbol{n}}_u \times \boldsymbol{X}(\boldsymbol{r}) \tag{2.47}$$

$$\boldsymbol{\mathcal{K}}_u^{PV}\{\boldsymbol{X}\}(\boldsymbol{r}) = \int_{PV, S_u} d\boldsymbol{r}' \boldsymbol{X}(\boldsymbol{r}') \times \nabla' g_u(\boldsymbol{r}, \boldsymbol{r}'), \tag{2.48}$$

where Ω_u is the integral solid angle. In Equation 2.47, the limit part of the $\boldsymbol{\mathcal{K}}$ operator is extracted, and PV indicates the principal value of the integral. By inserting these operators into Equations 2.44 and 2.45, SIEs are obtained as

$$\begin{aligned} -\boldsymbol{M}_u &= \hat{\boldsymbol{n}}_u \times \boldsymbol{E}_u^{inc}(\boldsymbol{r}) + \eta_u \times \hat{\boldsymbol{n}}_u \boldsymbol{\mathcal{T}}_u\{\boldsymbol{J}_u\}(\boldsymbol{r}) \\ &\quad - \hat{\boldsymbol{n}}_u \times \boldsymbol{\mathcal{K}}_u^{PV}\{\boldsymbol{M}_u\}(\boldsymbol{r}) + \hat{\boldsymbol{n}}_u \times \frac{4\pi - \Omega_u}{4\pi} \hat{\boldsymbol{n}}_u \times \boldsymbol{M}_u(\boldsymbol{r}) \qquad (2.49) \\ &= \hat{\boldsymbol{n}}_u \times \boldsymbol{E}_u^{inc}(\boldsymbol{r}) + \eta_u \hat{\boldsymbol{n}}_u \times \boldsymbol{\mathcal{T}}_u\{\boldsymbol{J}_u\}(\boldsymbol{r}) \\ &\quad - \hat{\boldsymbol{n}}_u \times \boldsymbol{\mathcal{K}}_u^{PV}\{\boldsymbol{M}_u\}(\boldsymbol{r}) - \boldsymbol{M}_u(\boldsymbol{r}) - \frac{\Omega_u}{4\pi} \boldsymbol{M}_u(\boldsymbol{r}) \qquad (2.50) \end{aligned}$$

$$\begin{aligned} \boldsymbol{J}_u &= \hat{\boldsymbol{n}}_u \times \boldsymbol{H}_u^{inc}(\boldsymbol{r}) + \eta_u^{-1} \times \hat{\boldsymbol{n}}_u \boldsymbol{\mathcal{T}}_u\{\boldsymbol{M}_u\}(\boldsymbol{r}) \\ &\quad + \hat{\boldsymbol{n}}_u \times \boldsymbol{\mathcal{K}}_u^{PV}\{\boldsymbol{J}_u\}(\boldsymbol{r}) - \hat{\boldsymbol{n}}_u \times \frac{4\pi - \Omega_u}{4\pi} \hat{\boldsymbol{n}}_u \times \boldsymbol{J}_u(\boldsymbol{r}) \qquad (2.51) \\ &= \hat{\boldsymbol{n}}_u \times \boldsymbol{H}_u^{inc}(\boldsymbol{r}) + \eta_u^{-1} \hat{\boldsymbol{n}}_u \times \boldsymbol{\mathcal{T}}_u\{\boldsymbol{M}_u\}(\boldsymbol{r}) \\ &\quad + \hat{\boldsymbol{n}}_u \times \boldsymbol{\mathcal{K}}_u^{PV}\{\boldsymbol{J}_u\}(\boldsymbol{r}) + \boldsymbol{J}_u(\boldsymbol{r}) - \frac{\Omega_u}{4\pi} \boldsymbol{J}_u(\boldsymbol{r}). \qquad (2.52) \end{aligned}$$

By rearranging the terms in Equations 2.50 and 2.52, normal electric-field integral equation (N-EFIE) and normal magnetic-field integral equation (N-MFIE) can be found respectively as

$$\begin{aligned} \eta_u \hat{\boldsymbol{n}}_u \times \boldsymbol{\mathcal{T}}_u\{\boldsymbol{J}_u\}(\boldsymbol{r}) - \hat{\boldsymbol{n}}_u \times \boldsymbol{\mathcal{K}}_u^{PV}\{\boldsymbol{M}_u\}(\boldsymbol{r}) \\ + \frac{\Omega_u}{4\pi} \boldsymbol{M}_u(\boldsymbol{r}) = -\hat{\boldsymbol{n}}_u \times \boldsymbol{E}_u^{inc}(\boldsymbol{r}) \qquad (2.53) \end{aligned}$$

$$\begin{aligned} \eta_u^{-1} \hat{\boldsymbol{n}}_u \times \boldsymbol{\mathcal{T}}_u\{\boldsymbol{M}_u\}(\boldsymbol{r}) + \hat{\boldsymbol{n}}_u \times \boldsymbol{\mathcal{K}}_u^{PV}\{\boldsymbol{J}_u\}(\boldsymbol{r}) \\ - \frac{\Omega_u}{4\pi} \boldsymbol{J}_u(\boldsymbol{r}) = -\hat{\boldsymbol{n}}_u \times \boldsymbol{H}_u^{inc}(\boldsymbol{r}). \qquad (2.54) \end{aligned}$$

By evaluating cross products of $-\hat{\boldsymbol{n}}_u$ with Equations 2.53 and 2.54, tangential electric-field integral equation (T-EFIE) and tangential magnetic-field integral equation (T-MFIE) are derived as

$$-\eta_u \hat{\boldsymbol{n}}_u \times \hat{\boldsymbol{n}}_u \times \boldsymbol{\mathcal{T}}_u\{\boldsymbol{J}_u\}(\boldsymbol{r}) + \hat{\boldsymbol{n}}_u \times \hat{\boldsymbol{n}}_u \times \boldsymbol{\mathcal{K}}_u^{PV}\{\boldsymbol{M}_u\}(\boldsymbol{r}) - \frac{\Omega_u}{4\pi}\hat{\boldsymbol{n}}_u \times \boldsymbol{M}_u(\boldsymbol{r}) = \hat{\boldsymbol{n}}_u \times \hat{\boldsymbol{n}}_u \times \boldsymbol{E}_u^{inc}(\boldsymbol{r}) \quad (2.55)$$

$$-\eta_u^{-1} \hat{\boldsymbol{n}}_u \times \hat{\boldsymbol{n}}_u \times \boldsymbol{\mathcal{T}}_u\{\boldsymbol{M}_u\}(\boldsymbol{r}) - \hat{\boldsymbol{n}}_u \times \hat{\boldsymbol{n}}_u \times \boldsymbol{\mathcal{K}}_u^{PV}\{\boldsymbol{J}_u\}(\boldsymbol{r}) + \frac{\Omega_u}{4\pi}\hat{\boldsymbol{n}}_u \times \boldsymbol{J}_u(\boldsymbol{r}) = \hat{\boldsymbol{n}}_u \times \hat{\boldsymbol{n}}_u \times \boldsymbol{H}_u^{inc}(\boldsymbol{r}). \quad (2.56)$$

2.1.2 Surface Formulations

Four integral equations derived in the previous part can be combined in many different ways to form alternative surface formulations. In general, surface formulations can be divided into three groups, i.e., tangential, normal, and mixed formulations. A combination of T-EFIE and/or T-MFIE lead to a tangential formulation, while a combination of N-EFIE and/or N-MFIE constructs a normal formulation. Mixed formulations can be constructed by combining at least one tangential SIE and one normal SIE.

Consider a penetrable structure (region D_i) represented by electrical parameters (ϵ_i, μ_i) in a host medium (region D_o) with electrical parameters (ϵ_o, μ_o), where the excitation exists. Since there is no source in region D_i, the right-hand sides of Equations 2.53−2.56 are zero for this region. Combination of tangential and normal integral equations with scalar coefficients can be shown in the most general form as

$$\begin{bmatrix} a\text{T-EFIE-O} + b\text{T-EFIE-I} + e\text{N-MFIE-O} - f\text{N-MFIE-I} \\ c\text{T-MFIE-O} + d\text{T-MFIE-I} - g\text{N-EFIE-O} + h\text{N-EFIE-I} \end{bmatrix}, \quad (2.57)$$

Where EFIEs and MFIEs for both D_i and D_o are considered. Considering operators, this general form of formulations can be written in a compact form as

$$\begin{bmatrix} \boldsymbol{\mathcal{Z}}_{11} & \boldsymbol{\mathcal{Z}}_{12} \\ \boldsymbol{\mathcal{Z}}_{21} & \boldsymbol{\mathcal{Z}}_{22} \end{bmatrix} \cdot \begin{bmatrix} \boldsymbol{J} \\ \boldsymbol{M} \end{bmatrix} (\boldsymbol{r}) = \begin{bmatrix} \boldsymbol{w}_1 \\ \boldsymbol{w}_2 \end{bmatrix} (\boldsymbol{r}), \quad (2.58)$$

where

$$\boldsymbol{\mathcal{Z}}_{11} = -a\eta_o\hat{\boldsymbol{n}} \times \hat{\boldsymbol{n}} \times \boldsymbol{\mathcal{T}}_o - b\eta_i\hat{\boldsymbol{n}} \times \hat{\boldsymbol{n}} \times \boldsymbol{\mathcal{T}}_i$$
$$+ e\hat{\boldsymbol{n}} \times \boldsymbol{\mathcal{K}}_o^{PV} - f\hat{\boldsymbol{n}} \times \boldsymbol{\mathcal{K}}_i^{PV} - (e+f)\boldsymbol{\mathcal{I}}/2 \tag{2.59}$$
$$\boldsymbol{\mathcal{Z}}_{12} = a\hat{\boldsymbol{n}} \times \hat{\boldsymbol{n}} \times \boldsymbol{\mathcal{K}}_o^{PV} + b\hat{\boldsymbol{n}} \times \hat{\boldsymbol{n}} \times \boldsymbol{\mathcal{K}}_i^{PV}$$
$$- (a-b)\hat{\boldsymbol{n}} \times \boldsymbol{\mathcal{I}}/2 + e\eta_o^{-1}\hat{\boldsymbol{n}} \times \boldsymbol{\mathcal{T}}_o - f\eta_i^{-1}\hat{\boldsymbol{n}} \times \boldsymbol{\mathcal{T}}_i \tag{2.60}$$
$$\boldsymbol{\mathcal{Z}}_{21} = -c\hat{\boldsymbol{n}} \times \hat{\boldsymbol{n}} \times \boldsymbol{\mathcal{K}}_o^{PV} - d\hat{\boldsymbol{n}} \times \hat{\boldsymbol{n}} \times \boldsymbol{\mathcal{K}}_i^{PV}$$
$$+ (c-d)\hat{\boldsymbol{n}} \times \boldsymbol{\mathcal{I}}/2 - g\eta_o\hat{\boldsymbol{n}} \times \boldsymbol{\mathcal{T}}_o + h\eta_i\hat{\boldsymbol{n}} \times \boldsymbol{\mathcal{T}}_i \tag{2.61}$$
$$\boldsymbol{\mathcal{Z}}_{22} = -c\eta_o^{-1}\hat{\boldsymbol{n}} \times \hat{\boldsymbol{n}} \times \boldsymbol{\mathcal{T}}_o - d\eta_i^{-1}\hat{\boldsymbol{n}} \times \hat{\boldsymbol{n}} \times \boldsymbol{\mathcal{T}}_i$$
$$+ g\hat{\boldsymbol{n}} \times \boldsymbol{\mathcal{K}}_o^{PV} - h\hat{\boldsymbol{n}} \times \boldsymbol{\mathcal{K}}_i^{PV} - (g+h)\boldsymbol{\mathcal{I}}/2 \tag{2.62}$$
$$\boldsymbol{w}_1 = a\hat{\boldsymbol{n}} \times \hat{\boldsymbol{n}} \times \boldsymbol{E}^{inc}(\boldsymbol{r}) - e\hat{\boldsymbol{n}} \times \boldsymbol{H}^{inc}(\boldsymbol{r}) \tag{2.63}$$
$$\boldsymbol{w}_2 = c\hat{\boldsymbol{n}} \times \hat{\boldsymbol{n}} \times \boldsymbol{H}^{inc}(\boldsymbol{r}) + g\hat{\boldsymbol{n}} \times \boldsymbol{E}^{inc}(\boldsymbol{r}). \tag{2.64}$$

In the above, $\eta_i = \sqrt{\mu_i/\epsilon_i}$ and $\eta_o = \sqrt{\mu_o/\epsilon_o}$ are intrinsic impedances of the inner and outer regions, $\hat{\boldsymbol{n}}$ is the outward unit vector for the inner medium, and $\boldsymbol{\mathcal{I}}$ is the identity operator. In addition, the observation points are assumed to be located on smooth surfaces so that the solid angle is set to 2π. Different SIE formulations can be derived by selecting scalar coefficients; some examples of conventional formulations for penetrable structures can be written as follows.

- Poggio-Miller-Chang-Harrington-Wu-Tsai (PMCHWT) formulation [25, 26, 27]:
  $a = 1, b = 1, c = 1, d = 1, e = 0, f = 0, g = 0, h = 0$
- Combined tangential formulation (CTF) [28]:
  $a = \eta_o^{-1}, b = \eta_i^{-1}, c = \eta_o, d = \eta_i, e = 0, f = 0, g = 0, h = 0$
- Modified combined tangential formulation (MCTF) [16]:
  $a = 1, b = 1, c = \eta_o\eta_i, d = \eta_o\eta_i, e = 0, f = 0, g = 0, h = 0$
- Electric-magnetic current combined-field integral equation (JMCFIE) [29]:
  $a = \eta_o^{-1}, b = \eta_i^{-1}, c = \eta_o, d = \eta_i, e = 1, f = 1, g = 1, h = 1$

PMCHWT formulation has both tangential and normal forms; however, only the tangential one gives stable results by using the Galerkin scheme [18]. Since the Galerkin

discretization is used in this study, T-PMCHWT formulation is presented in the above. Using low-order discretizations, PMCHWT formulation is an accurate formulation, especially compared to mixed and normal formulations, due to the cancellation of the identity operator. Unfortunately, it suffers from ill-conditioning because of unbalanced diagonal blocks [30]. CTF has a better-conditioned system than PMCHWT thanks to its identical diagonal blocks, making it very suitable for ordinary penetrable structures. However, CTF has inaccuracy issues for plasmonic cases, particularly as the negative permittivity increases. JMCFIE leads to fast iterative convergences but relatively poor accuracy due to the dominant identity operator in this formulation. MCTF contains well-balanced diagonal blocks with reasonably balanced nondiagonal blocks, making it more resistant to the negative permittivity values in comparison to CTF, while it is also more efficient than PMCHWT in terms of iterative solutions.

2.1.3 Method of Moments and Discretization

Numerical techniques can be used to solve electromagnetic scattering problems involving arbitrary geometries. Equivalent currents can be expanded with basis functions by the discretization of both geometry and surface integral equations. Using MOM [31, 32], matrix equations are constructed and solved in order to obtain unknown coefficients of basis functions.

Any SIE formulations can be considered in a general form as

$$\boldsymbol{\mathcal{L}}\{\boldsymbol{f}\}(\boldsymbol{r}) = \boldsymbol{g}(\boldsymbol{r}), \tag{2.65}$$

where $\boldsymbol{\mathcal{L}}$ is a linear operator, $\boldsymbol{f}(\boldsymbol{r})$ is the unknown vector function, and $\boldsymbol{g}(\boldsymbol{r})$ is the known vector function. In this equation, the integro-differential and identity operators can be considered to form the linear operator, while the excitation is included in the known vector function. In addition, the unknown vector function represents equivalent currents to be solved. The unknown vector function can be expanded in a series of known basis functions $\boldsymbol{b}_n (n = 1, 2, ..., N)$ as

$$\boldsymbol{f}(\boldsymbol{r}) \approx \sum_{n=1}^{N} \boldsymbol{a}[n]\boldsymbol{b}_n(\boldsymbol{r}), \tag{2.66}$$

where N is the number of discretization functions and $a[n]$ represents the unknown cofficient of nth basis function. Using this expansion, Equation 2.65 can be rewritten as

$$\sum_{n=1}^{N} \boldsymbol{a}[n]\boldsymbol{\mathcal{L}}\{\boldsymbol{b}_n(\boldsymbol{r})\} = \boldsymbol{g}(\boldsymbol{r}). \tag{2.67}$$

Using a set of linearly independent testing functions $\boldsymbol{t}_m (m = 1, 2, ..., N)$, Equation 2.67 can be tested as

$$\int d\boldsymbol{r}\boldsymbol{t}_m(\boldsymbol{r}) \cdot \sum_{n=1}^{N} \boldsymbol{a}[n]\boldsymbol{\mathcal{L}}\{\boldsymbol{b}_n(\boldsymbol{r})\} = \int d\boldsymbol{r}\boldsymbol{t}_m(\boldsymbol{r}) \cdot \boldsymbol{g}(\boldsymbol{r}). \tag{2.68}$$

By rearranging the order of the summation and integration in Equation 2.68, we obtain

$$\sum_{n=1}^{N} \boldsymbol{a}[n] \int d\boldsymbol{r}\boldsymbol{t}_m(\boldsymbol{r}) \cdot \boldsymbol{\mathcal{L}}\{\boldsymbol{b}_n(\boldsymbol{r})\} = \int d\boldsymbol{r}\boldsymbol{t}_m(\boldsymbol{r}) \cdot \boldsymbol{g}(\boldsymbol{r}). \tag{2.69}$$

This equation can be expressed in a matrix form as

$$\sum_{n=1}^{N} \boldsymbol{a}[n]\bar{\boldsymbol{Z}}[m, n] = \boldsymbol{w}[m], \quad (m = 1, 2, ...N), \tag{2.70}$$

where

$$\bar{\boldsymbol{Z}}[m, n] = \int d\boldsymbol{r}\boldsymbol{t}_m(\boldsymbol{r}) \cdot \boldsymbol{\mathcal{L}}\{\boldsymbol{b}_n(\boldsymbol{r})\} \tag{2.71}$$

$$\boldsymbol{w}[m] = \int d\boldsymbol{r}\boldsymbol{t}_m(\boldsymbol{r}) \cdot \boldsymbol{g}(\boldsymbol{r}). \tag{2.72}$$

In electromagnetics, $\bar{\boldsymbol{Z}}$ is usually known as impedance matrix, which includes electromagnetic interactions between discretization elements, $\boldsymbol{a}$ is a vector of unknown coefficients of basis to expand equivalent currents, and $\boldsymbol{w}$ is called excitation vector that represents sources.

As a common option for the discretization of three-dimensional objects, the Rao-Wilton-Glisson (RWG) [17] functions can be defined on triangular domains. For this purpose, all surfaces of an object can be discretized by using relatively small triangles with respect to wavelength. An RWG function is defined on a triangle pair as

$$\boldsymbol{b}_n(\boldsymbol{r}) = \begin{cases} \dfrac{l_n}{2A_{n1}}(\boldsymbol{r} - \boldsymbol{r}_{n1}), & \boldsymbol{r} \in S_{n1} \\ \dfrac{l_n}{2A_{n2}}(\boldsymbol{r}_{n2} - \boldsymbol{r}), & \boldsymbol{r} \in S_{n2} \\ 0, & \boldsymbol{r} \notin S_n, \end{cases} \tag{2.73}$$

where l_n represents the length of the main edge, and A_{n1} and A_{n2} are the areas of first (S_{n1}) and second (S_{n2}) triangles associated with the edge. The RWG functions are divergence conforming and their divergence is finite everywhere, i.e.,

$$\nabla \cdot \boldsymbol{b}_n(\boldsymbol{r}) = \begin{cases} \dfrac{l_n}{A_{n1}}, & \boldsymbol{r} \in S_{n1} \\ -\dfrac{l_n}{A_{n2}}, & \boldsymbol{r} \in S_{n2} \\ 0, & \boldsymbol{r} \notin S_n. \end{cases} \tag{2.74}$$

The discretization of the tangentially and rotationally tested integro-differential operators can be written as

$$\begin{aligned} \bar{\boldsymbol{T}}_u^T[m,n] &= ik_u \int_{S_m} d\boldsymbol{r}\boldsymbol{t}_m(\boldsymbol{r}) \cdot \int_{S_n} d\boldsymbol{r}' g_u(\boldsymbol{r},\boldsymbol{r}')\boldsymbol{b}_n(\boldsymbol{r}') \\ &\quad + \frac{i}{k_u} \int_{S_m} d\boldsymbol{r}\boldsymbol{t}_m(\boldsymbol{r}) \cdot \int_{S_n} d\boldsymbol{r}' \nabla g_u(\boldsymbol{r},\boldsymbol{r}')\nabla' \cdot \boldsymbol{b}_n(\boldsymbol{r}') \end{aligned} \tag{2.75}$$

$$\begin{aligned} \bar{\boldsymbol{T}}_u^N[m,n] &= ik_u \int_{S_m} d\boldsymbol{r}\boldsymbol{t}_m(\boldsymbol{r}) \cdot \hat{\boldsymbol{n}} \times \int_{S_n} d\boldsymbol{r}' g_u(\boldsymbol{r},\boldsymbol{r}')\boldsymbol{b}_n(\boldsymbol{r}') \\ &\quad + \frac{i}{k_u} \int_{S_m} d\boldsymbol{r}\boldsymbol{t}_m(\boldsymbol{r}) \cdot \hat{\boldsymbol{n}} \times \int_{S_n} d\boldsymbol{r}' \nabla g_u(\boldsymbol{r},\boldsymbol{r}')\nabla' \cdot \boldsymbol{b}_n(\boldsymbol{r}') \end{aligned} \tag{2.76}$$

$$\bar{\boldsymbol{K}}_{PV,u}^T[m,n] = \int_{S_m} d\boldsymbol{r}\boldsymbol{t}_m(\boldsymbol{r}) \cdot \int_{PV,S_n} d\boldsymbol{r}' \boldsymbol{b}_n(\boldsymbol{r}') \times \nabla' g_u(\boldsymbol{r},\boldsymbol{r}') \tag{2.77}$$

$$\bar{\boldsymbol{K}}_{PV,u}^N[m,n] = \int_{S_m} d\boldsymbol{r}\boldsymbol{t}_m(\boldsymbol{r}) \cdot \hat{\boldsymbol{n}} \times \int_{PV,S_n} d\boldsymbol{r}' \boldsymbol{b}_n(\boldsymbol{r}') \times \nabla' g_u(\boldsymbol{r},\boldsymbol{r}'). \tag{2.78}$$

Using the divergence-conforming RWG functions, we can modify Equations 2.75, 2.77, and 2.78 as

$$\begin{aligned} \bar{\boldsymbol{T}}_u^T[m,n] &= ik_u \int_{S_m} d\boldsymbol{r}\boldsymbol{t}_m(\boldsymbol{r}) \cdot \int_{S_n} d\boldsymbol{r}' g_u(\boldsymbol{r},\boldsymbol{r}')\boldsymbol{b}_n(\boldsymbol{r}') \\ &\quad - \frac{i}{k_u} \int_{S_m} d\boldsymbol{r} \nabla \cdot \boldsymbol{t}_m(\boldsymbol{r}) \int_{S_n} d\boldsymbol{r}' g_u(\boldsymbol{r},\boldsymbol{r}')\nabla' \cdot \boldsymbol{b}_n(\boldsymbol{r}') \end{aligned} \tag{2.79}$$

$$\bar{\boldsymbol{K}}_{PV,u}^T[m,n] = \int_{S_m} d\boldsymbol{r}\boldsymbol{t}_m(\boldsymbol{r}) \cdot \boldsymbol{b}_n(\boldsymbol{r}) \times \int_{PV,S_n} d\boldsymbol{r}' \nabla' g_u(\boldsymbol{r},\boldsymbol{r}') \tag{2.80}$$

$$\bar{\boldsymbol{K}}_{PV,u}^N[m,n] = \int_{S_m} d\boldsymbol{r}\,(\boldsymbol{t}_m(\boldsymbol{r}) \times \hat{\boldsymbol{n}}) \cdot \boldsymbol{b}_n(\boldsymbol{r}) \times \int_{PV,S_n} d\boldsymbol{r}' \nabla' g_u(\boldsymbol{r},\boldsymbol{r}'). \tag{2.81}$$

Also, the identity operator can be discretized by employing the RWG functions as

$$\bar{\boldsymbol{I}}^T[m,n] = \int_{S_m} d\boldsymbol{r}\boldsymbol{t}_m(\boldsymbol{r}) \cdot \boldsymbol{b}_n(\boldsymbol{r}) \tag{2.82}$$

$$\bar{\boldsymbol{I}}^N[m,n] = \int_{S_m} d\boldsymbol{r}\boldsymbol{t}_m(\boldsymbol{r}) \cdot \hat{\boldsymbol{n}} \times \boldsymbol{b}_n(\boldsymbol{r}). \tag{2.83}$$

Consider the interaction of two half RWG functions; testing function t_{ma}^{RWG} related to the ath triangle of the mth edge and basis function b_{nb}^{RWG} related to the bth triangle of the nth edge. Equations 2.75–2.83 can be rewritten as

$$\begin{aligned}\bar{\boldsymbol{T}}_u^T[m,n,a,b] &= ik_u\mathcal{A}_{ma,nb}\int_{S_{ma}} d\boldsymbol{r}(\boldsymbol{r}-\boldsymbol{r}_{ma})\cdot\boldsymbol{I}_u^{(\boldsymbol{r}'-\boldsymbol{r}_{nb})} \\ &\quad -\frac{4i}{k_u}\mathcal{A}_{ma,nb}\int_{S_{ma}} d\boldsymbol{r}I_u^1 \end{aligned} \tag{2.84}$$

$$\begin{aligned}\bar{\boldsymbol{T}}_u^N[m,n,a,b] &= ik_u\mathcal{A}_{ma,nb}\int_{S_{ma}} d\boldsymbol{r}(\boldsymbol{r}-\boldsymbol{r}_{ma})\cdot\hat{\boldsymbol{n}}\times\boldsymbol{I}_u^{(\boldsymbol{r}'-\boldsymbol{r}_{nb})} \\ &\quad -\frac{2i}{k_u}\mathcal{A}_{ma,nb}\int_{S_{ma}} d\boldsymbol{r}(\boldsymbol{r}-\boldsymbol{r}_{ma})\cdot\hat{\boldsymbol{n}}\times\boldsymbol{I}_u^{\nabla'} \end{aligned} \tag{2.85}$$

$$\bar{\boldsymbol{K}}_{PV,u}^T[m,n,a,b] = \mathcal{A}_{ma,nb}\int_{S_{ma}} d\boldsymbol{r}(\boldsymbol{r}-\boldsymbol{r}_{ma})\cdot(\boldsymbol{r}-\boldsymbol{r}_{nb})\times\boldsymbol{I}_u^{\nabla'} \tag{2.86}$$

$$\bar{\boldsymbol{K}}_{PV,u}^N[m,n,a,b] = \mathcal{A}_{ma,nb}\int_{S_{ma}} d\boldsymbol{r}(\boldsymbol{r}-\boldsymbol{r}_{ma})\times\hat{\boldsymbol{n}}\cdot(\boldsymbol{r}-\boldsymbol{r}_{nb})\times\boldsymbol{I}_u^{\nabla'} \tag{2.87}$$

$$\bar{\boldsymbol{I}}^T[m,n,a,b] = \mathcal{A}_{ma,nb}\delta_{ma,nb}\int_{S_{ma}} d\boldsymbol{r}(\boldsymbol{r}-\boldsymbol{r}_{ma})\cdot(\boldsymbol{r}-\boldsymbol{r}_{nb}) \tag{2.88}$$

$$\bar{\boldsymbol{I}}^N[m,n,a,b] = \mathcal{A}_{ma,nb}\delta_{ma,nb}\int_{S_{ma}} d\boldsymbol{r}(\boldsymbol{r}-\boldsymbol{r}_{ma})\cdot\hat{\boldsymbol{n}}\times(\boldsymbol{r}-\boldsymbol{r}_{nb}), \tag{2.89}$$

where

$$\mathcal{A}_{ma,nb} = \frac{l_m l_n}{4A_{ma}A_{nb}}\gamma_{ma}\gamma_{nb}, \tag{2.90}$$

and

$$I_u^1 = \int_{S_{nb}} d\boldsymbol{r}' g(\boldsymbol{r},\boldsymbol{r}') \tag{2.91}$$

$$\boldsymbol{I}_u^{(\boldsymbol{r}'-\boldsymbol{r}_{nb})} = \int_{S_{nb}} d\boldsymbol{r}' g(\boldsymbol{r},\boldsymbol{r}')(\boldsymbol{r}'-\boldsymbol{r}_{nb}) \tag{2.92}$$

$$\boldsymbol{I}_u^{\nabla'} = \int_{S_{nb}} d\boldsymbol{r}'\nabla' g(\boldsymbol{r},\boldsymbol{r}'). \tag{2.93}$$

In these equations, l_m and l_n represent the lengths of the mth and nth edges, A_{ma} and A_{nb} represent the areas of the triangles, and $\gamma_{nb}, \gamma_{ma} = \pm 1$, depending on the direction of the testing and basis functions on triangles. Finally, $\delta_{ma,nb}$ represents the Kronecker delta.

2.1.4 Multilevel Fast Multipole Algorithm

MOM provides accurate numerical solutions of electromagnetic scattering and radiation problems. However, the cost of these solutions can be prohibitive in terms of sim-

ulation time and memory usage due to the dense matrix equations obtained by the discretization of SIE formulations. These matrix equations involving $\mathcal{O}(N)$ unknowns can be solved iteratively, and the required matrix-vector multiplications (MVM) for iterative solutions can be performed directly with $\mathcal{O}(N^2)$ complexity. Consequently, MOM becomes inefficient as the number of unknowns grows, i.e., when an object is electrically large and/or it is densely discretized. In this study, MOM can still be used for nanoantenna design and optimization trials for single nanoantennas, due to typically small problem size. For the relatively larger problems, i.e., nanoantenna arrays, MVMs must be improved in terms of efficiency due to limitations in computational power and time. As well known in the literature, the fast multipole method (FMM)[33] can provide more efficient solutions in comparison to the direct MOM, by reducing the complexity per MVM to $\mathcal{O}(N^{3/2})$. As an improved method, MLFMA [34] employs FMM recursively, reducing the complexity to $\mathcal{O}(N \log N)$ [18] and enabling the solution of larger problems with limited computational resources and time.

An impedance matrix includes all interactions between basis and testing functions; however, MLFMA categorizes these interactions in two groups as near-field interactions and far-field interactions. While near-field interactions are calculated directly, MLFMA calculates far-field interactions in a group-by-group manner without storing them in the memory. These calculations of far-field interactions are based on the Gegenbauer's addition theorem, which is used to factorize the Green's function. In order to organize interactions, the object (scatterer) is placed into a cubic box and recursively divided into sub-boxes to construct a tree structure of $L = \mathcal{O}(\log N)$ levels. The recursive division of boxes continues until the desired box size is reached, while all empty boxes are omitted during this process. The smallest boxes at the lowest level are usually chosen proportional to the wavelength.

The group-by-group scheme for calculating far-field interactions has three stages: aggregation, translation, and disaggregation. These stages are performed consecutively on the multilevel tree structure for each MVM. In the aggregation operation, radiated fields of boxes are calculated in a level-by-level manner. At the lowest level, radiation patterns of basis functions are shifted to the centers of the associated boxes. The radiated field of a box at a higher level is calculated by the combination of radiated fields

of its sub-boxes. Once they are complete, radiated fields are transformed into incoming fields by the translation operation. In the disaggregation, total incoming fields are shifted from the highest to the lowest level. For each box, which is not located at the highest level, the total incoming field involves both translated fields and the ones shifted from its parent box. As the final process of disaggregation, total incoming fields at the lowest level are received by testing functions.

2.2 Modeling Plasmonic Structures

In order to perform accurate and efficient computational analyses of nanoantennas, the unique plasmonic properties of metals must be modeled very carefully. Material properties required for penetrable modeling can be extracted from measurement data available in the literature. Then, SIE formulations can be utilized to solve benchmark problems to examine the performances of the solvers for different material properties. As shown below with selected examples, we consider accuracy and efficiency of solutions with different formulations in detail before attempting realistic nanoantenna simulations.

2.2.1 Metals at Optical Frequencies

Harmonic oscillator models can be used to explain optical properties of different materials. Among these, Drude model is usually used to define intraband electron conductions in metals. This model is often extended by Lorentz oscillation model, leading to Lorentz-Drude model, to obtain expressions for both intraband effect and interband transition. Complex electrical permittivity derived by using Drude model can be written as

$$\epsilon_D(\omega) = 1 - \frac{\omega_p^2}{\omega^2 + i\gamma\omega^2}, \tag{2.94}$$

where ω_p is the angular plasma frequency of the given material, while γ represents the damping effect. Using Lorentz-Drude model, this expression can be modified as

$$\epsilon_{LD}(\omega) = 1 - \frac{\omega_p^2}{\omega^2 + i\gamma\omega^2} + \sum_{k=2}^{N} \frac{f(k)\omega_p^2}{\omega_k^2 - \omega^2 - i\gamma_k\omega}, \tag{2.95}$$

where N is the total number of higher-energy mode oscillators, $f(k)$ represents weighting coefficients, and γ_k is the damping coefficient of the kth resonant mode. Drude and Lorentz-Drude model parameters can be extracted from the paper of Rakic et al [15].

Silver (Ag) and gold (Au) are often used as nanoantenna materials as they enable high power enhancements. Complex relative permittivities ($\epsilon_r = \epsilon_{Rr} + i\epsilon_{Ir}$) of Ag and Au are computed by using harmonic oscillator models (Drude and Lorentz-Drude models). In order to compare the models, complex relative permittivities of Ag and Au with respect to frequency obtained by using Drude and Lorentz-Drude models are compared with measurement results from a well-known paper [35], as shown in Figures 2.1 and 2.2. As the oscillation frequency approaches the plasma frequency of Ag ($f_p^{Ag} = 2178.6$ THz) and Au ($f_p^{Au} = 2183.4$ THz), the real part of the relative permittivity for both Au and Ag goes to one, as expected. In these figures, both models provide promising results that are consistent with the measured values for the real part of complex permittivity; yet, Lorentz-Drude model provides a better fit for the imaginary part for both Au and Ag. As a general trend, when the frequency drops, the real part of the permittivity becomes increasingly negative, while the imaginary part increases, becoming consistent with the perfectly conducting models. However, for small-scale objects, like nanoantennas, it is not obvious where PEC models could be used; in fact, for the nanoantennas considered in this study, we reach the conclusion that penetrable models must be used in the entire range of the optical spectrum.

2.2.2 Comparison of SIE Formulations for Plasmonic Structures

Strong frequency dependency of optical properties of metals makes the selection of SIE formulations critical for accurate and efficient simulations. Conventional SIE formulations mentioned in the previous part are generally utilized for ordinary penetrable materials. Nevertheless, these formulations can directly be turned into plasmonic solvers by rigorous selections of branches, considering complex wavenumber and intrinsic impedance values. Unfortunately, large negative real permittivities of metals, not seen in the ordinary materials, constitute a numerical challenge that must be handled. In this section, some canonical problems are analyzed by using a selected

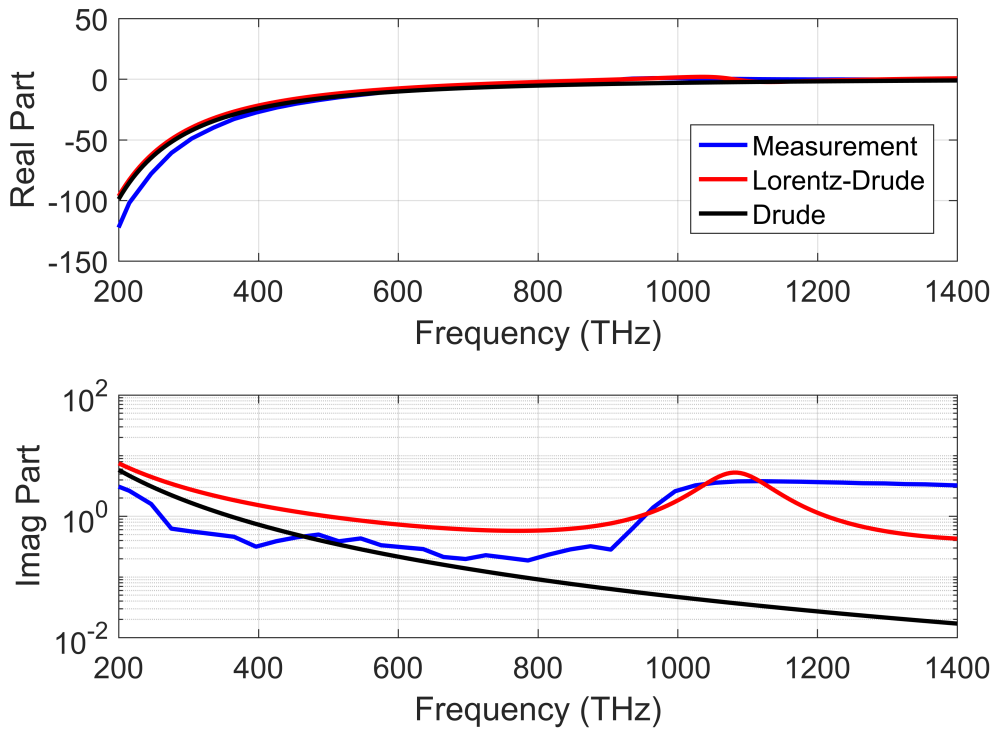

Figure 2.1: Relative complex permittivity of Ag with respect to frequency.

set of traditional SIE formulations. Accuracy and efficiency of simulations are discussed in the context of varying plasmonic properties of metals at optical frequencies.

As the benchmark scenario, a scattering problem involving a metallic (Ag) sphere located in free space is considered. The sphere is illuminated by an x-polarized plane wave with 1 V/m electric field intensity propagating in z direction. Excitation frequencies in the range from 250 THz to 750 THz are considered in numerical simulations. Frequency-dependent complex permittivity values of Ag, which possesses strong plasmonic properties, are found by using Lorentz-Drude model. In order to observe the effect of numerical modeling, the electrical size of the sphere is fixed, i.e., its diameter set to λ, while the mesh size is selected as $\lambda/20$ at each frequency. The constructed MOM matrix equations are solved iteratively by using the generalized minimal residual (GMRES) method with no preconditioner or restart, and the target residual error is chosen as 10^{-4}.

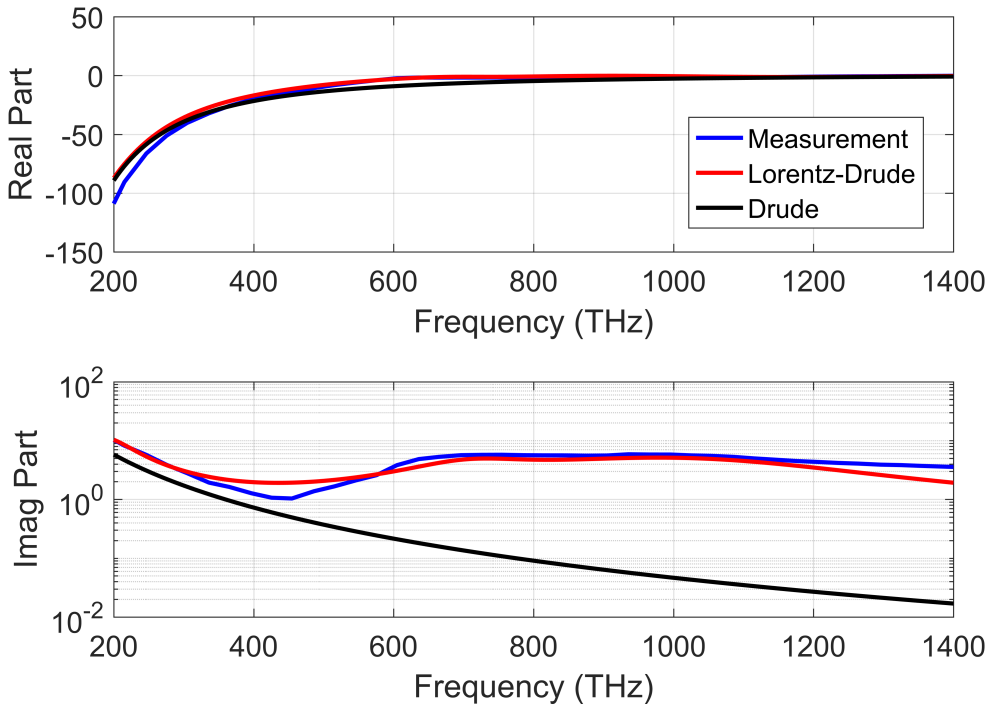

Figure 2.2: Relative complex permittivity of Au with respect to frequency.

For the scattering problems described above, unknown equivalent surface currents are computed by using PMCHWT, CTF, MCTF, and JMCFIE. Then, far-zone electric field values are calculated as $\boldsymbol{E}^{far}(\theta,\phi) = \lim_{\boldsymbol{R}\to\infty}\{\boldsymbol{R}\times\boldsymbol{E}(R,\theta,\phi)\}$ for each formulation, and the results obtained on the z-x plane are compared with analytical Mie-series solutions. Far-zone electric field values obtained at frequencies from 250 THz and 750 THz with 50 THz steps are depicted in Figure 2.3, while the relative permittivity values at simulation frequencies are listed in Table 2.1 in the form of $\epsilon_r(f) = \epsilon_{Rr}(f) + \epsilon_{Ir}(f)$. For a quantitative comparison of the formulations, the relative error in far-zone electric field is defined as

$$RE = \frac{||E^{far}_{Comp} - E^{far}_{Mie}||_2}{||E^{far}_{Mie}||_2}, \tag{2.96}$$

where E^{far}_{Comp} and E^{far}_{Mie} are electric field vectors of values at 360 samples in the z-x plane, and $||\cdot||_2$ represents l^2 norm. Figure 2.4 includes these error values, along with the number of GMRES iterations required in simulations. Based on the results in Figures 2.3 and 2.4, we have the following comments on the accuracy and iterative efficiency of the formulations.

Table 2.1: Real and imaginary parts of relative permittivity values of Ag obtained by Lorentz-Drude model with respect to frequency.

$f(THz)$	ϵ_{rR}	ϵ_{iR}	$f(THz)$	ϵ_{rR}	ϵ_{iR}
250	-60.6667	4.3025	550	-9.7990	0.8388
300	-41.1725	2.8175	600	-7.6164	0.7298
350	-29.3884	2.0096	650	-5.8881	0.6529
400	-21.7165	1.5226	700	-4.4815	0.6024
450	-16.4347	1.2067	750	-3.3030	0.5769
500	-12.6344	0.9911			

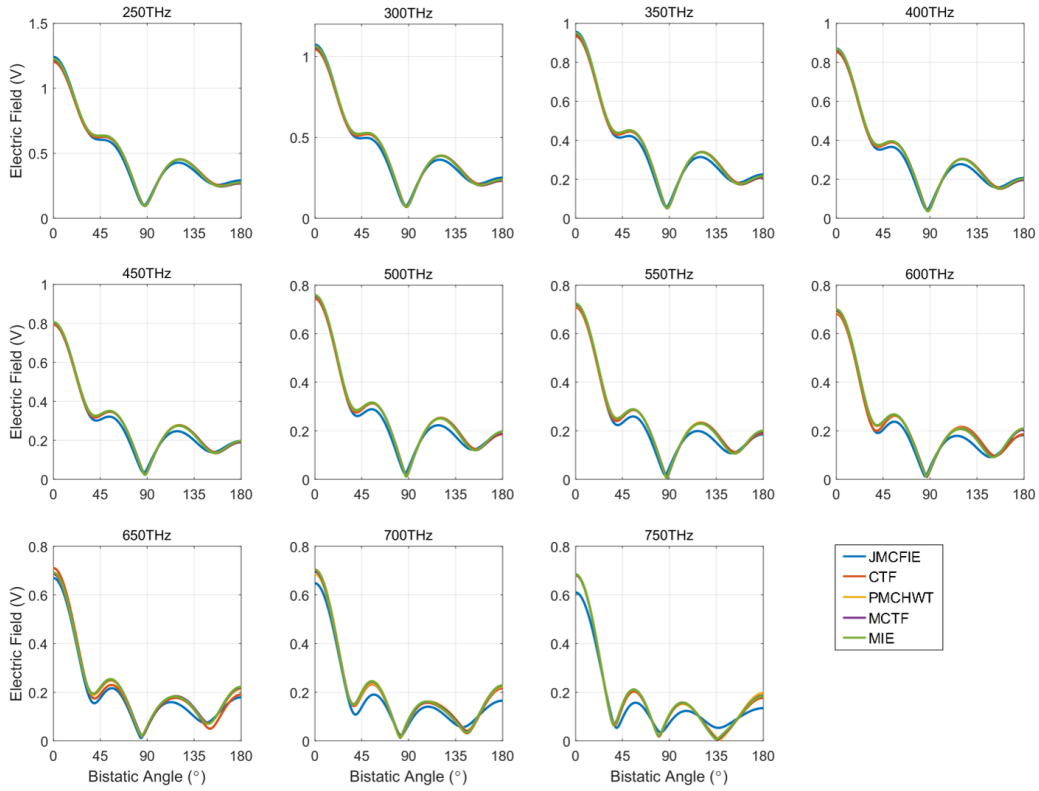

Figure 2.3: Bistatic far-zone electric field values scattered from a Ag sphere with λ diameter from 250 THz to 750 THz. The relative permittivity of Ag changes from $-60.6667 + 4.3025i$ to $-3.3030 + 0.5769i$.

- Among the four formulations considered in these numerical tests, JMCFIE is the only combined formulation, involving the identity operator in the related

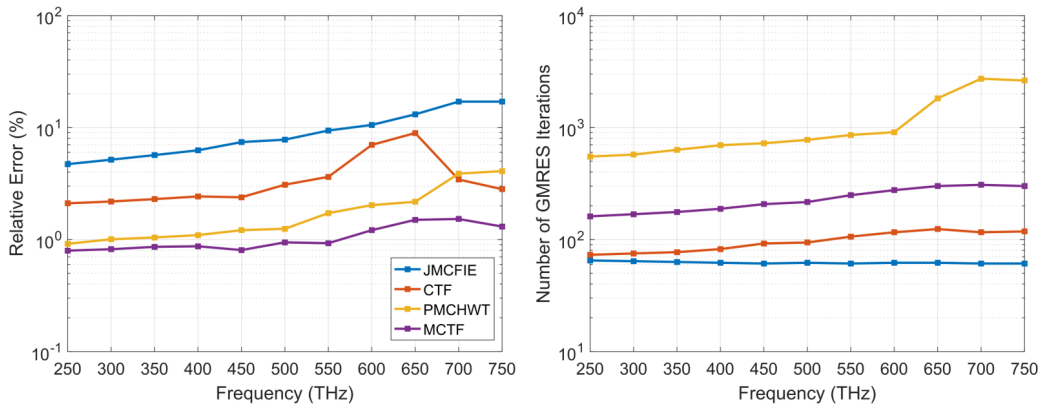

Figure 2.4: The relative error (in percentage) in the numerical solutions depicted in Figure 2.3 with respect to the corresponding Mie-series solutions (left) and the required number of GMRES iterations (right).

impedance matrices. Therefore, at any frequency, the fastest iterative convergence is achieved by this formulation, as expected. On the other hand, the presence of the identity operator decreases accuracy [36]. This is clearly visible as error values even higher than 10% at some frequencies, which is particularly dramatic considering the canonical nature of the problems.

- CTF behaves very differently, in comparison to its performance for ordinary materials. This formulation is theoretically a first-kind integral equation, leading to slow iterative convergence together with good accuracy. Interestingly, for plasmonic problems, CTF is dominated by the inner T operator that converges into an identity operator [16]. Consequently, this formulation becomes iteratively efficient but inaccurate, similar to JMCFIE.

- An average error rate of 1.85% and a maximum error rate of 4% makes PMCHWT suitable for accurate results. Unfortunately, the computational cost of PMCHWT is beyond affordable as a result of the ill-conditioned nature of its impedance matrices.

- MCTF has a remarkably good accuracy as this formulation was particularly developed for plasmonic problems; the error rate of this formulation remains below 1% in the majority of the frequency range. MCTF is also much more efficient than PMCHWT, making this formulation suitable for accurate simula-

tions of nanoantennas.

2.3 Concluding Remarks

This chapter is devoted to full-wave simulations of three-dimensional problems involving metallic nanoantennas, which behave as plasmonic structures at optical frequencies. Starting from Maxwell's equations, SIEs (EFIE and MFIE) are obtained by employing equivalence surface currents. Surface formulations are derived by different combinations of tangential and normal EFIE and MFIE. Unknown surface currents are expanded by using the RWG functions to construct MOM matrix equations. FMM and MLFMA methods are introduced to accelerate iterative solutions of dense matrix systems involving large numbers of unknowns.

Although metals at lower frequencies can be modeled as PECs, nanoscale metals should be modeled as penetrable objects in the visible light spectrum. The complex electrical permittivity values for the conventional metals, such as Au and Ag, can be extracted from measurement data or harmonics oscillator models. In order to solve the resulting electromagnetic scattering problems involving metals with unique electrical properties, surface formulations frequently used in the literature are implemented. Surface formulations are compared in terms of computational cost and accuracy on canonical problems. As shown in the sample results, JMCFIE provides the fastest iterative convergence; but MCTF, which can achieve the most accurate results with a moderate computational requirements, stands out as the most suitable formulation for nanoantennas.

CHAPTER 3

DESIGN AND SIMULATION OF NANOANTENNAS FOR HIGH POWER ENHANCEMENT CHARACTERISTICS

Nanoantennas with different properties in terms of material, shape, and size, are analyzed with the help of three-dimensional computational simulations. In these analyses, we examine the effects of various design parameters on the power enhancement ratio. Furthermore, wideband and multiband characteristics for strong hot spots are investigated. In addition to manual design procedures, we present shape optimization via genetic algorithms to obtain superior designs that achieve desired electromagnetic responses.

3.1 Simulation Techniques

The details of the numerical solver used for the simulation of three-dimensional nanoantenna structures and the genetic algorithm mechanism used for the shape optimization are described in this section.

3.1.1 Details of Simulation Environment

In this chapter, all simulations and optimization processes are performed by using MOM in the frequency domain, since all nanoantenna designs are relatively small with respect to wavelength. Problems including three-dimensional nanoantenna structures with plasmonic properties are formulated via SIEs, particularly with MCTF for accurate analyses. Nanoantenna structures and formulations are discretized with the RWG functions defined on triangular domains. Consider a computational problem

involving $U+1$ regions labeled as D_u for $u = 0, 1, 2, ...$, where $u = 0$ is the host medium, $u = 1$ is the plasmonic nanoantenna, and $u = 2, 3, ...$ represent additional substrate layers that may be required for layers in composite models. Then, the constructed matrix equations (using MCTF) can be written in the form of

$$\begin{bmatrix} \boldsymbol{Z}_{11}^{MCTF} & \boldsymbol{Z}_{12}^{MCTF} \\ \boldsymbol{Z}_{21}^{MCTF} & \boldsymbol{Z}_{22}^{MCTF} \end{bmatrix} \cdot \begin{bmatrix} \boldsymbol{a}_J \\ \boldsymbol{a}_M \end{bmatrix} = \begin{bmatrix} \boldsymbol{v} \\ \boldsymbol{w} \end{bmatrix}, \tag{3.1}$$

where

$$\boldsymbol{Z}_{11}^{MCTF} = \sum_{u=0}^{U} \eta_u \boldsymbol{T}_u^T, \qquad \boldsymbol{Z}_{12}^{MCTF} = -\sum_{u=0}^{U} \boldsymbol{K}_u^T \tag{3.2}$$

$$\boldsymbol{Z}_{21}^{MCTF} = \sum_{u=0}^{U} \eta_u \eta_{u'} \boldsymbol{K}_u^T, \qquad \boldsymbol{Z}_{22}^{MCTF} = \sum_{u=0}^{U} \eta_{u'} \boldsymbol{T}_u^T \tag{3.3}$$

$$\boldsymbol{v} = \sum_{u=0}^{U} v_u, \qquad \boldsymbol{w} = \sum_{u=0}^{U} w_u. \tag{3.4}$$

In the above, $\boldsymbol{a}_J$ and $\boldsymbol{a}_M$ are arrays of expansion coefficients for equivalent electric and magnetic currents, respectively, while $\eta_u = \sqrt{\mu_u}/\sqrt{\epsilon_u}$ is the characteristic impedance of medium u. In addition, u' represents the domain that shares the interface with domain u, at which the testing operation is applied. The expressions for the discretized tangential operators $\boldsymbol{T}_u^T$ and $\boldsymbol{K}_u^T$ for medium u are given in the previous chapter [spesifically in Equations (2.79) and (2.80)]. Contributions to the excitation vectors in Equation 3.4 can be written as

$$\boldsymbol{v}_u = -\gamma_{m,u} \int_{S_m} d\boldsymbol{r} \boldsymbol{t}_m(\boldsymbol{r}) \cdot \boldsymbol{E}_u^{inc}(\boldsymbol{r}) \tag{3.5}$$

$$\boldsymbol{w}_u = -\eta_u \eta_{u'} \gamma_{m,u} \int_{S_m} d\boldsymbol{r} \boldsymbol{t}_m(\boldsymbol{r}) \cdot \boldsymbol{H}_u^{inc}(\boldsymbol{r}), \tag{3.6}$$

where $\boldsymbol{t}_m(\boldsymbol{r})$ is the testing function, $\gamma_{m,u} = \pm 1$ represents orientation of testing function, and $\boldsymbol{E}_u^{inc}(\boldsymbol{r})$ and $\boldsymbol{H}_u^{inc}(\boldsymbol{r})$ represent the incident electric and magnetic field intensity created by external sources located inside D_u.

3.1.2 Implementation of Genetic Algorithms for Shape Optimization

In electromagnetism, optimization tools are often used in design procedures to obtain optimal shapes and configurations that can provide the required electromagnetic responses. As nature-inspired techniques, genetic algorithms (GAs) [37][38] provide excellent flexibility for optimization procedures and they can easily be implemented within electromagnetic solvers. On the other hand, an extensive number of trials may be required to obtain desired results when using GAs. Since optimization problems involve single nanoantennas, the benefits of GAs outweigh their drawbacks in this study.

In this study, shape optimization of nanoantenna structures for high power enhancement responses at desired frequency or frequencies (in multiband and wideband applications) is presented. The iterative MOM solver is combined with an in-house GA implementation to reach optimal geometries. A multigrid scheme is implemented to deal with huge optimization spaces, where coarse details in a nanoantenna design are transformed into fine details by utilizing grids. Specifically, as a grid is refined, the effective optimization space is systematically expanded. Systematic expansion of the optimization space enables easier observations of nanoantenna performances with node movements. Moreover, the resulting nanoantenna designs are typically more suitable for fabrication using the multigrid technique instead of a brute-force (single-grid) technique.

The main purpose of an optimization trial is to deform a selected surface of the given nanoantenna in a way that the enhancement factor at the gap center increases. As the starting point, the surface to be deformed and the deformation limits are selected. Consider a multigrid optimization involving G grids, where $g = 1, 2, ..., G$ are performed consecutively. Then, each GA individual has a chromosome of bN_g bits, where N_g is the number of grid nodes and b is the number of bits used to encode the position of each grid node. The deformation range is divided into $2^{(b-1)}$ intervals, while 2^{bN_g} corresponds to the total number of candidate solutions in the optimization space. After computing equivalent currents represented by an individual (using MOM, as previously mentioned), the corresponding cost function is chosen as the

enhancement factor [see Equation (3.7)]. This cost function is used for evaluating the success of the individual with respect to others. The selection process for the best individual continues until the given number of maximum generations is reached. Once an optimization process for a grid (that is not the finest one) is completed, nodal representations of the most successful individual or individuals are constructed for the fine grid ($g + 1$). In these constructions, new nodes are introduced by dividing each grid triangle into four subtriangles. Incrementation in the number of grid nodes (N_g) leads to longer chromosomes, while the optimization space expands accordingly. When an optimization for a last grid is completed, the overall optimization is considered to be completed with the output of the most successful individual. Then, various post-processing analyses are performed, including a frequency sweep to examine the overall frequency characteristics of the optimal geometry.

3.2 Numerical Analyses of Design Parameters

We examine various nanoantenna design parameters in the context of achieving high power enhancement capabilities in a range of frequencies. Particularly the effect of the used material, shape, size, and substrate are investigated by the numerical solver described above. Unless stated otherwise, the same simulation parameters are used in the numerical simulations. Mesh sizes in discretizations are usually chosen as 8 nm, i.e., $\lambda/50$ at the highest frequency of the considered range (750 THz). Frequency-dependent complex permittivity values of metals are extracted from the Lorentz-Drude model. GMRES is used as the iterative solver, while the target residual error for a satisfactory iterative convergence is set to 0.0001 in all simulations. Nanoantennas are symmetrically located on the x-y plane (bottom/top surfaces are at $z = \mp$ thickness$/2$), while they are excited by light sources from top. A light excitation is modeled as 1 V/m linearly polarized plane wave (the electric field intensity is polarized in the direction of the nanoantenna under exposure). Given an observation point $\boldsymbol{r}$, the pointwise enhancement factor is calculated as

$$enh(\boldsymbol{r}) = \frac{|\boldsymbol{S}(\boldsymbol{r})|}{\left|\boldsymbol{S}^{inc}(\boldsymbol{r})\right|} = \frac{|\boldsymbol{E}(\boldsymbol{r}) \times [\boldsymbol{H}(\boldsymbol{r})]^*|}{\left|\boldsymbol{E}^{inc}(\boldsymbol{r}) \times \left[\boldsymbol{H}^{inc}(\boldsymbol{r})\right]^*\right|}, \tag{3.7}$$

where $\boldsymbol{S}(\boldsymbol{r})$ represents the total complex power density, $\boldsymbol{S}^{inc}(\boldsymbol{r})$ is the complex power density of incident light wave, and * represents the complex conjugate operation. We

note that the pointwise enhancement factor tends to be singular at the edges of a nanoantenna, while we particularly consider gap centers, as in realistic scenarios, which do not possess any numerical difficulty.

3.2.1 The Effect of the Material Used

As it is well known, the material type is a crucial factor for the enhancement ability of a nanoantenna. For the nanoantenna geometry depicted on the left-hand side of Figure 3.1, the effect of the material is briefly considered on the right-hand side of the same figure. The enhancement factor is found at the gap of the nanoantenna, when the material is selected as Ag, Al, Au, Cu, and Pt. Without strong plasmonic responses, Al and Pt are not very suitable to obtain high power enhancement factors, while the best performance in terms of achievable maximum enhancement is obtained with Ag. We note that, Au may be preferred depending on the frequency, e.g., it provides more than 40 enhancement factor at 400 THz, while the corresponding value is around 30 if Ag is used at the same frequency.

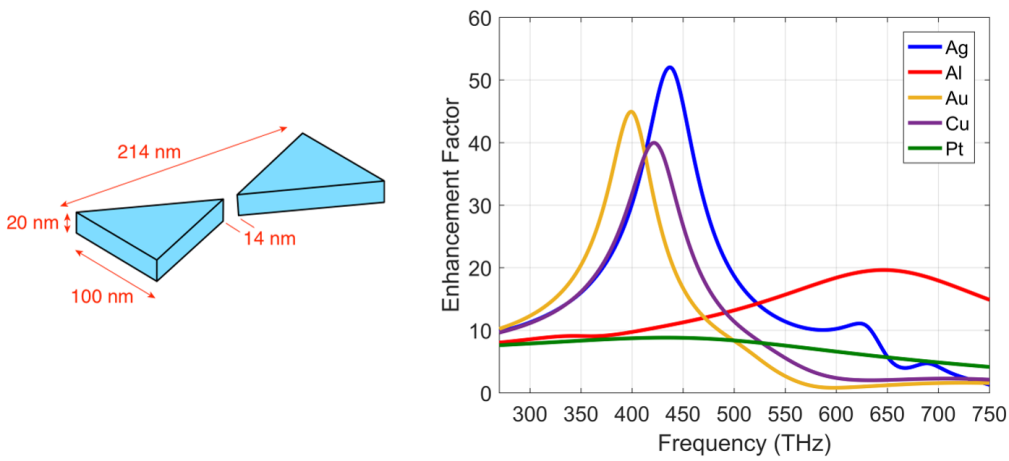

Figure 3.1: A bowtie nanoantenna (left) and power enhancement factor at its gap when different materials are used (right).

3.2.2 The Effect of the Nanoantenna Shape

Commonly used nanoantenna geometries with fixed size and material (Ag) are considered in order to analyze the effect of the nanoantenna shape on the enhancement capability. Each arm of nanoantenna geometries can fit in a box with $100 \times 100 \times 20$ nm dimensions, while the gap size (distance between the elements) is set to 14 nm. Four different nanoantennas with triangular (leading to bowtie), cylindrical, hexagonal, and square elements and their frequency-dependent enhancement factors are presented in Figure 3.2. Each nanoantenna geometry has a different resonance frequency, in addition to their different enhancement factor values. Clearly, the bowtie nanoantenna is the most successful design, considering the maximum power enhancement capability. However, cylindrical and hexagonal nanoantennas can be used at the higher frequency ranges specifically above 470 and 490 THz, respectively. Although the square nanoantenna seems to perform worse than other designs, it can still be preferred in some applications due to its easier fabrication.

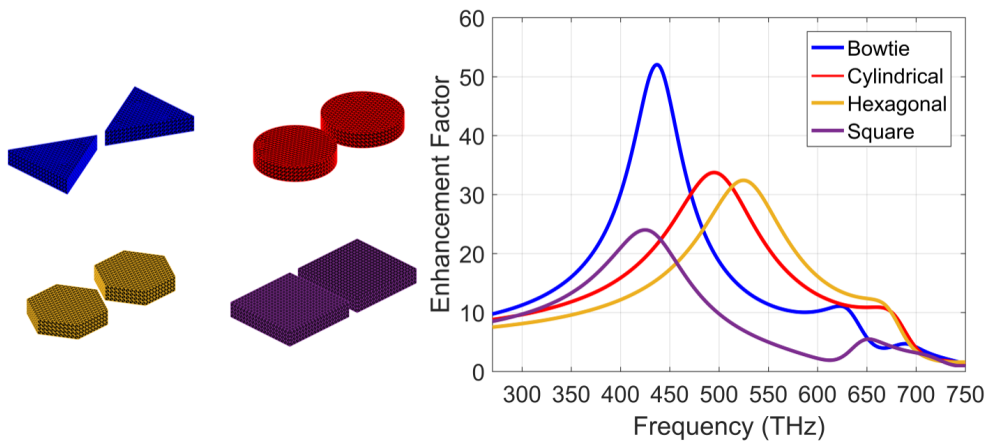

Figure 3.2: Power enhancement factor with respect to the frequency is given when different nanoantenna shapes are used.

3.2.3 The Effect of Smoothing

In the previous examples, bowtie nanoantenna geometries have sharp edges, which contribute to create powerful hot spots. Unfortunately, in realistic scenarios, it may not be possible to achieve such sharp edges. We now consider the effect of these unavoidable curved edges, which may occur involuntarily in fabricated samples, on the enhancement factor. As an example, Ag bowtie nanoantenna with 10 nm gap size, depicted in Figure 3.1, is considered. The edge blending process and the obtained enhancement factor values with respect to frequency for each radius of curvature (ROC) are shown in Figure 3.3. We observe that an increase in the ROC value leads to a decrease in the maximum enhancement factor, as expected. Besides, the resonance tends to shift to higher frequencies. However, the geometry with 2 nm curvature still outperforms the other geometries in Figure 3.2, even at their resonance frequencies. The results in Figure 3.3 clearly demonstrates the importance of fabrication to achieve high enhancement factors with classical types of nanoantennas.

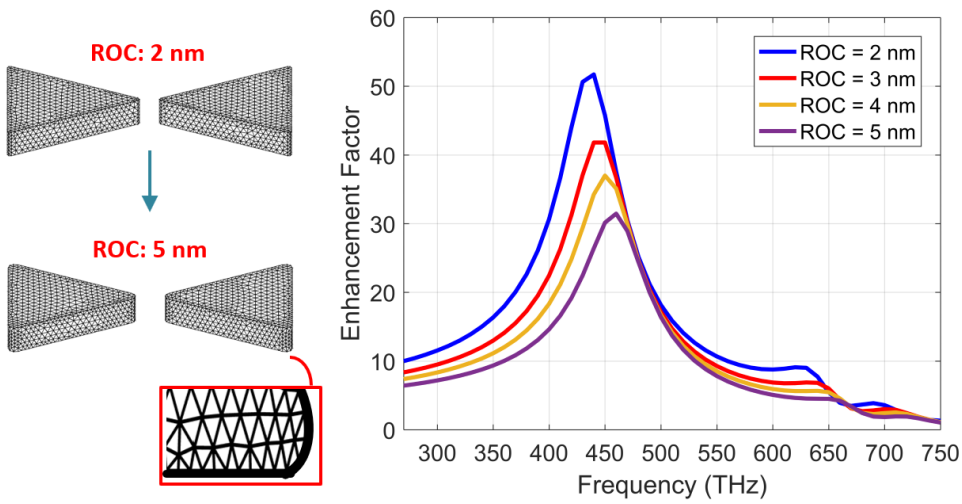

Figure 3.3: Curved bowtie geometries ($100 \times 100 \times 20$ nm arms and 10 nm gap size) with minimum and maximum ROC values (left) and frequency-dependent enhancement factor values for Ag nanoantennas with $2, 3, 4$, and 5 nm ROC values (right).

3.2.4 The Effect of the Gap Size

Nanoantennas typically involve symmetrically located sharp tips with strong electromagnetic interactions, leading to high power enhancements at the gaps between them. Consequently, the size of a gap is a crucial factor in obtaining powerful hot spots. The effect of the gap size on the enhancement factor is investigated by using the Ag bowtie nanoantenna with 2 nm ROC shown in Figure 3.3. The gap size is changed from 10 nm to 25 nm, and the corresponding enhancement factors computed at gap centers are presented in Figure 3.4. The results are similar to those obtained for curved edges; the highest power enhancement factor values are obtained for the shortest apertures, as expected. On the other hand, nanoantenna designs with different gap sizes have similar resonance frequencies, i.e., gap size has little effect on the frequency range of operation. As the results clearly indicate, the gap size should be as small as possible to achive the best enhancement performance; unfortunately, the achievable gap size can be very limited in typical fabrication setups.

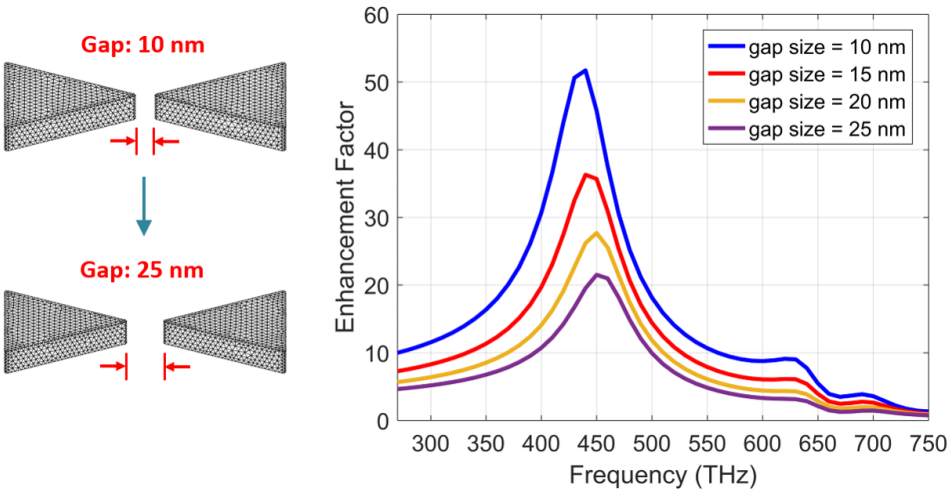

Figure 3.4: Curved bowtie geometries ($100 \times 100 \times 20$ nm arms, 2 nm ROC, and 10 nm gap size) with minimum and maximum gap sizes (left) and frequency-dependent enhancement factor values for Ag nanoantennas with $10, 15, 20,$ and 25 nm gap sizes (right).

3.2.5 The Effect of the Thickness

The thickness of a metallic structure is an essential factor for its plasmonic properties, e.g., plasmonic effects may disappear with increasing thickness. However, quite thin metallic nanostructures an easily be fabricated with today's technology, making it possible to produce high-quality nanoantennas. Ag nanoantennas with 2 nm ROC, 10 nm gap size, and $20, 30$, and 40 nm thickness values are used to demonstrate the effect of thickness on the enhancement factor. A visualization of the thickening process and the obtained enhancement factor values with respect to frequency are shown in Figure 3.5. Unsurprisingly, the maximum enhancement factor decreases as the thickness increases, while the resonance frequency is shifted by more than 30 THz towards the blue-light frequencies as the thickness is doubled. Even though their maximum enhancement values are smaller, the geometries with 30 nm and 40 nm thicknesses seem to be more suitable for applications using 460-480 THz and 480-630 THz ranges, respectively.

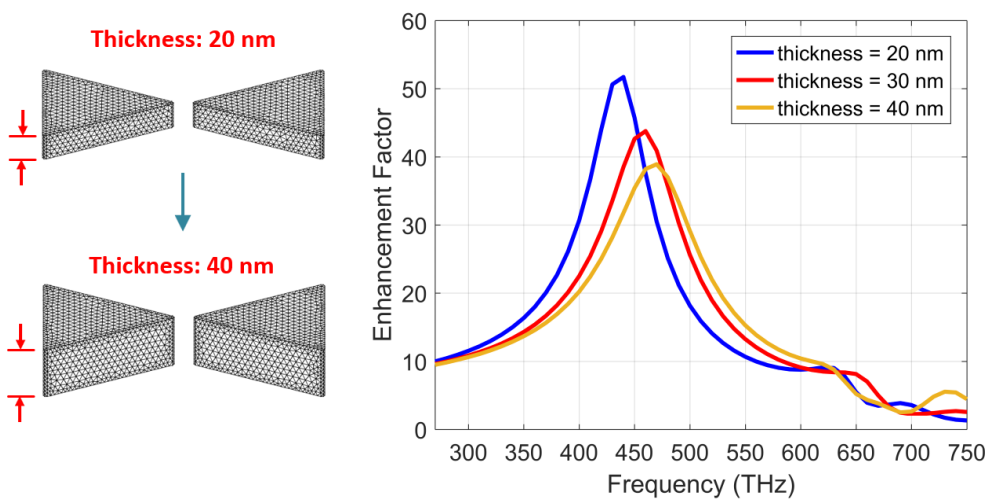

Figure 3.5: Frequency-dependent enhancement factor values for Ag bowtie nanoantennas with $20, 30,$ and 40 nm thicknesses.

3.2.6 The Effect of the Size

In various examples considered above, the effect of each design parameter has been demonstrated as isolated, i.e., when all other parameters are kept constant. In order to continue in the same manner, the effect of the size on the enhancement factor is examined with bowtie geometries for which only the upper and lower surface areas are scaled to avoid the contribution of the scaled thickness. However, it may be misleading to study the effect of the size on enhancement characteristics using only one type of metal. At radio frequencies, the resonance frequency of an antenna shifts inversely proportionally to its size. Since electrical properties of metals at optical frequencies depend on frequency (in fast, rapidly change in some frequency ranges), frequency-dependent characteristics of nanoantennas can change dramatically depending on their sizes. As an example, three nanoantennas with different sizes given in Figure 3.6 are simulated by considering both Au and Ag as the nanoantenna material. Dimensions of a single arm for nanoantenna geometries, called B1, B2, and B3 are $100 \times 100 \times 20$ nm, $125 \times 125 \times 20$ nm, and $150 \times 150 \times 20$ nm, respectively. The gap size is chosen as 30 nm for each geometry. The enhancement factor values obtained for these geometries with two different materials are given in Figure 3.7.

In Figure 3.7, we observe that, as the size of the nanoantenna increases, the resonance shifts toward lower frequencies, while the maximum enhancement factor increases. It can also be observed that smaller bowtie nanoantennas are more useful to obtain higher enhancement factors in the visible-light spectrum. Considering different materials, the very similar maximum enhancement values are observed for Au and Ag nanoantennas for when B3 is used. If the size of nanoantenna decrease from B3 to B1 dimensions, the resonance frequency of the Au nanoantenna is shifted by almost 60 THz with a decrease in the enhancement factor value of above 7. For the same dimensional changes, the resonance frequency of the Ag nanoantenna is shifted by 82 THz with a decrease in the enhancement factor value of nearly 4. Therefore, the type of the metal used, which is generally ignored in the radio-frequency antennas, must be considered carefully in dimensional modifications of nanoantennas.

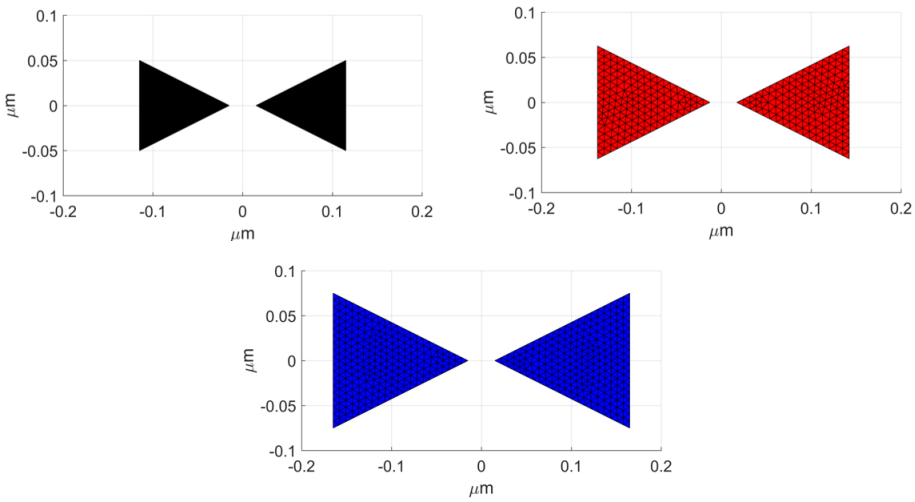

Figure 3.6: Bowtie geometries B1, B2, and B3 with single arm dimensions of $100 \times 100 \times 20$ nm, $125 \times 125 \times 20$ nm, and $150 \times 150 \times 20$ nm, respectively. The gap size is fixed to 30 nm.

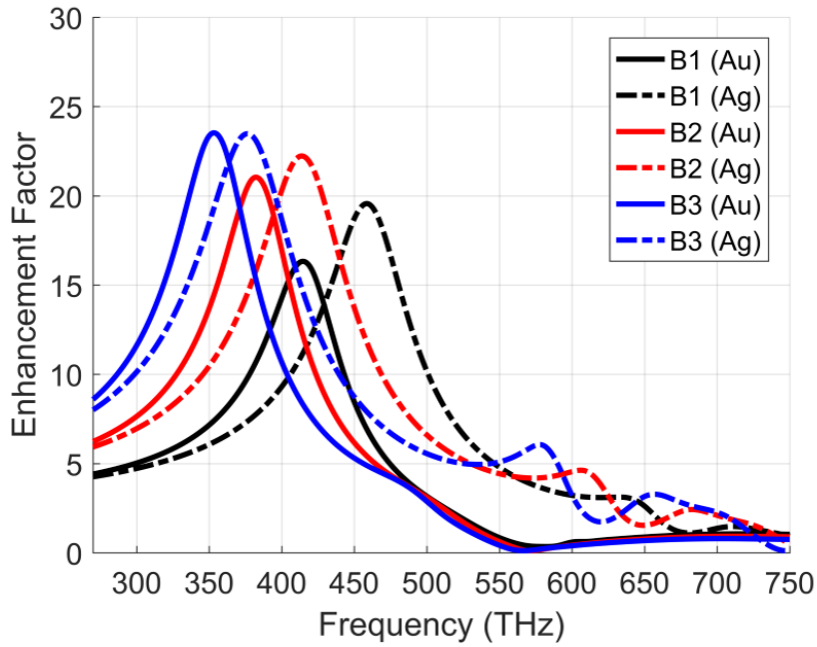

Figure 3.7: Frequency-dependent enhancement factor values of Au (solid lines) and Ag (dashed line) bowtie nanoantenna geometries B1, B2, and B3.

For further investigation of the effect of size on nanoantenna characteristics, we consider geometries with square elements. Each arm of nanoantenna geometries S1, S2, and S3 have $100 \times 100 \times 20$ nm, $125 \times 125 \times 20$ nm, and $150 \times 150 \times 20$ nm dimensions, respectively, while the gap size is chosen as 30 nm for each geometry. All designs are simulated with both Au and Ag materials. The generic shape of the nanoantennas is depicted on the left-hand side of Figure 3.8, while the computed enhancement factor values for all geometries and both materials are shown on the right-hand side of the same figure. As we can see, enhancement factor curves for the nanoantennas with the same dimensions but different materials are very similar with small frequency shifts. For bowtie nanoantennas, enlarging the geometry enables higher enhancement factor values, whereas this pattern cannot be observed for square nanoantennas. Among square nanoantennas, S2 geometry has the most powerful resonance for both Au and Ag materials. These results verify that the design of a nanoantenna is a complex process, where material, shape, size, and similar parameters must be considered together.

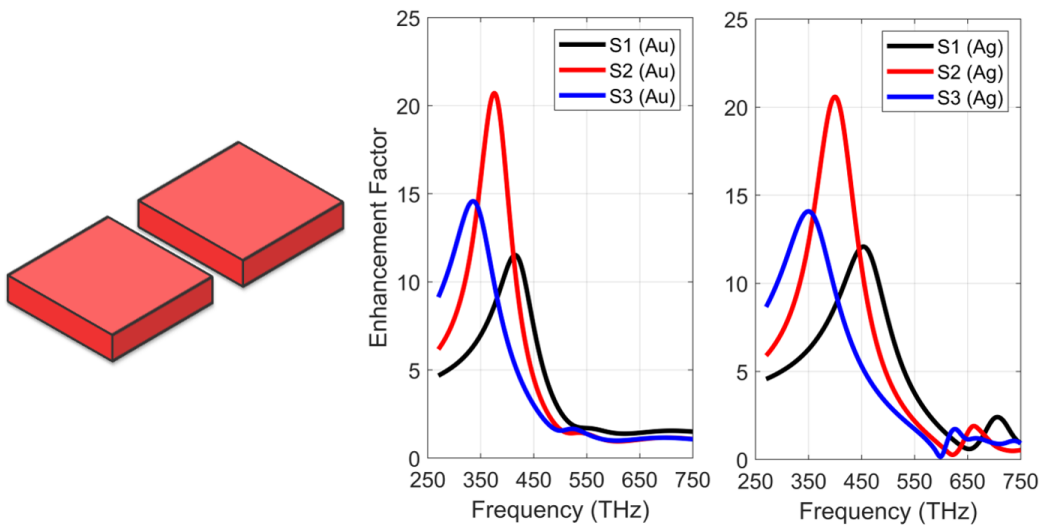

Figure 3.8: The generic shape of square nanoantennas (left) and frequency-dependent enhancement factor curves for Au and Ag S1, S2, and S3 designs (right).

3.2.7 The Effect of the Substrate

So far, nanoantennas are assumed to be floating in the free-space to reduce the computational costs and to observe effects of design parameters without the interference of complex interactions. However, in general, nanoantennas are fabricated on substrates. Although substrates may have different materials and thicknesses, a silicon substrate with 50 nm thickness, which can be fabricated in most setups, is considered in the following simulations. In addition, a chrome layer (always shaped in accordance with the considered nanoantenna) is included in the simulations, as this type of layers are often used to attach Au and Ag on substrates. Silicon substrates and additional chrome layers are tested for B1, B2, and B3 geometries, when these layers are scaled according to the nanoantennas. The resulting structure for B1 geometry is shown in Figure 3.9. With appropriate scalings, dimensions of substrates are determined as $300 \times 300 \times 50$ nm, $400 \times 400 \times 50$ nm, and $500 \times 500 \times 50$ nm, respectively, for B1, B2, and B3. The corresponding dimensions of chrome layers are $100 \times 100 \times 2$ nm, $125 \times 125 \times 2$ nm, and $150 \times 150 \times 2$ nm. In order to compare the effects of the added layers separately for each geometry, enhancement factor values are calculated and given in Figure 3.10. Since the electrical permittivity of silicon is at considerable levels at these frequencies (complex relative permittivies changes from 12+0i to 31+3.4i), we can observe improved focusing properties for all designs. However, the chrome layers that are added to make fabrications easier decrease plasmonic properties to some extent. Another remarkable effect of the substrate layers is

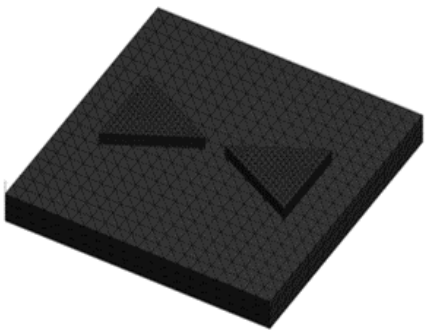

Figure 3.9: B1 nanoantenna geometry ($100 \times 100 \times 20$ nm) with silicon substrate ($300 \times 300 \times 50$ nm) and chrome layer ($100 \times 100 \times 2$ nm.

that frequencies for the maximum enhancement values shift towards lower frequencies. In fact, for B3 geometry, maximum enhancement frequency is out of the range. In general, the resonance frequency of a nanoantenna geometry designed in vacuum is expected to be shifted when it is located on a substrate (e.g., when it is fabricated and tested). Also, as shown in Figure 3.10, weak resonances tend to appear at higher frequencies due to interactions of nanoantennas with silicon and chrome layers.

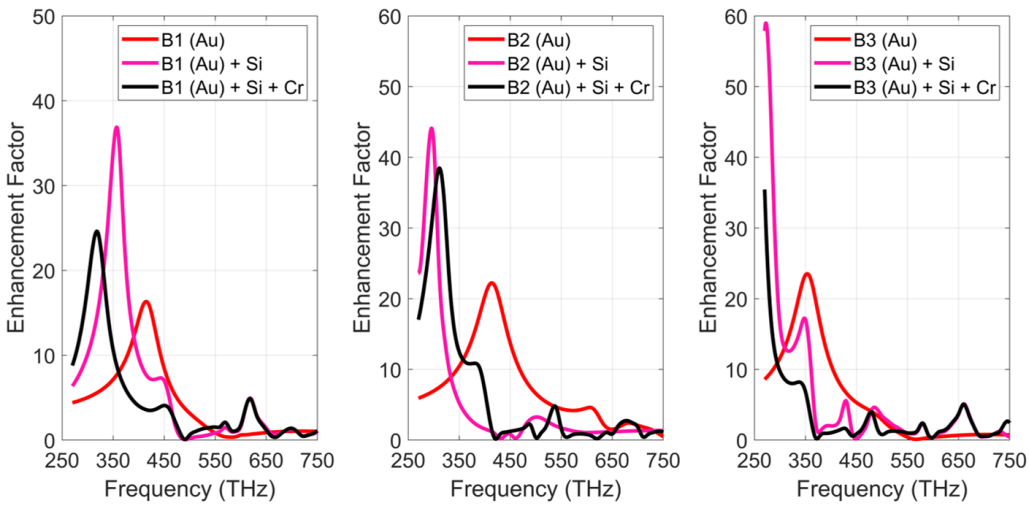

Figure 3.10: Frequency-dependent enhancement factors of Au bowtie nanoantennas B1, B2, and B3 with silicon substrates and chrome layers.

3.3 Numerical Analysis of Slitted Nanoantenna Designs with Multiband Characteristics

In the previous section, it is shown that quite wideband power enhancement characteristics at optical frequencies can be achieved with relatively simple nanoantenna designs. However, generating strong hot spots at multiple frequencies can provide extra advantages in some applications, such as energy harvesting and biosensing. In antenna applications, slitted antennas are frequently used to create multiband operations; this type of strategies are also adopted in our designs at optical frequencies. Since many factors are affecting the enhancement factor value, simulations with different slit parameters are performed to investigate the response of the designed slitted

nanoantennas.

The effect of slit parameters on the enhancement factor is examined by using nanoantennas B1, B2, and B3. First, the slit width is considered; $15, 25,$ and 35 nm slits are opened at the center of each arm of Ag B1 geometry. A description of geometries and the computed enhancement values with respect to frequency are given in Figure 3.11. Second, the slit position is examined by placing the mid-point of the slit at $25, 50,$ and 75 nm away from the tips. A description of B1 geometry with slits at different positions and the corresponding enhancement factors for Ag material are given in Figure 3.12. Finally, B1 geometry with a symmetrically located slit of width 15 nm is scaled to construct slitted B2 and B3 geometries, when their slit widths are 18.75 nm and 22.25 nm, respectively. In these trials, the slit orientation is also investigated by using slits on the same side and on opposite sides of the arms, which are called BSS and BOS, respectively. Both Ag and Au materials are considered to observe the effect of different materials. BSS1 and BOS1 geometries are illustrated on the left-hand side of Figure 3.13, while the enhancement factor curves for different designs and materials are given on the right-hand side of the same figure. Our comments on frequency-dependent enhancement factors of slitted nanoantenna designs (Figures

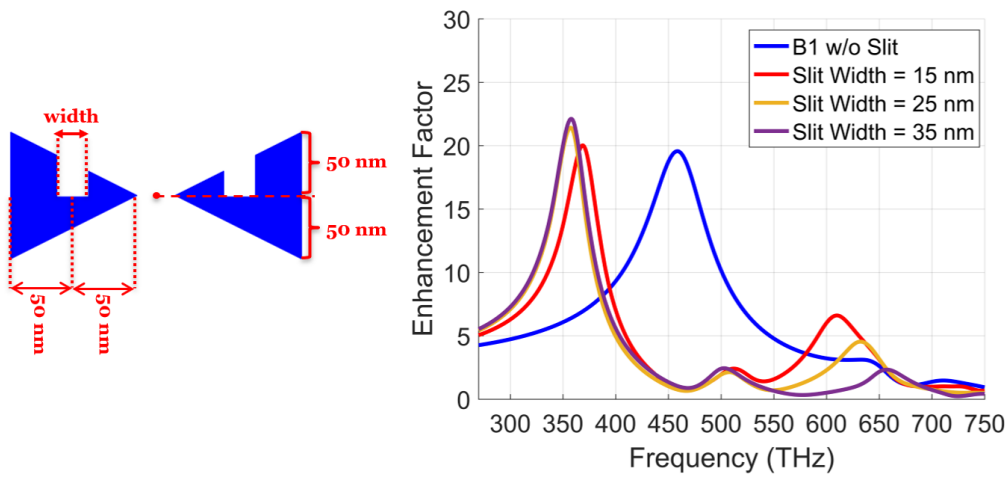

Figure 3.11: Slitted B1 geometry with varying slit width (left) and frequency-dependent enhancement factor values of slitted and ordinary Ag B1 geometries (right).

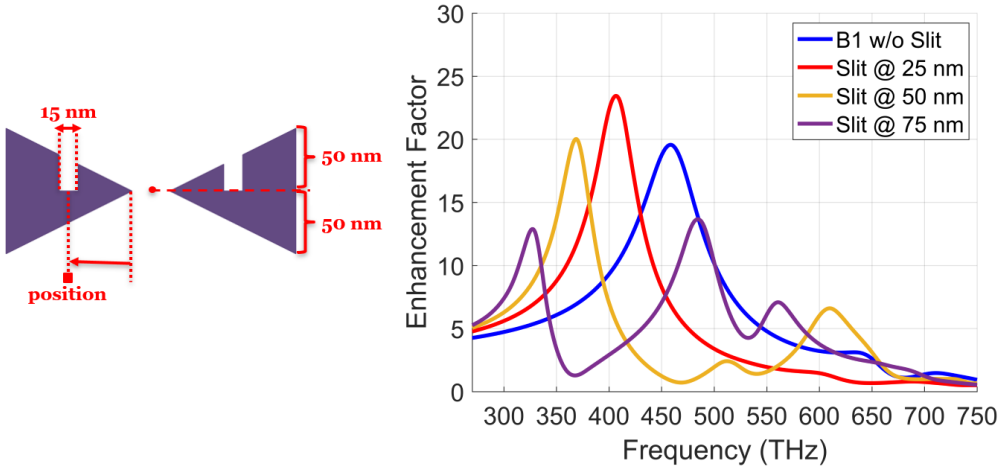

Figure 3.12: Slitted B1 geometry with varying slit positions (left) and frequency-dependent enhancement factor values of slitted and ordinary Ag B1 geometries (right).

3.11-3.13) are given below.

- In general, a secondary enhancement factor peak is achieved in almost all cases, i.e., whenever a slit is opened on an original nanoantenna. We can say that a well-known method at radio frequencies to create multiband frequency responses can be used for optical antenna designs.

- As shown in Figure 3.11, slits located at the centers of arms shift the peak frequency to lower frequencies. Also, the shifted primary resonances are stronger than the original one in terms of the maximum enhancement factor value. The magnitude of the enhancement factor in the second resonance is inversely proportional to the width of the slit. This may be due to the fact that a slit reduces the overall area of the illuminated surface of the nanoantenna. In addition, weak resonances are observed at 500 THz, while they do not seem to be significant in terms of power enhancement.

- As shown in Figure 3.12, a secondary resonance does not occur when slits are located very close to the tips, while even three resonances occur when they are located near the edges. In all cases, the main peak is shifted towards lower frequencies; in fact,the amount of the frequency shift is directly proportional to the

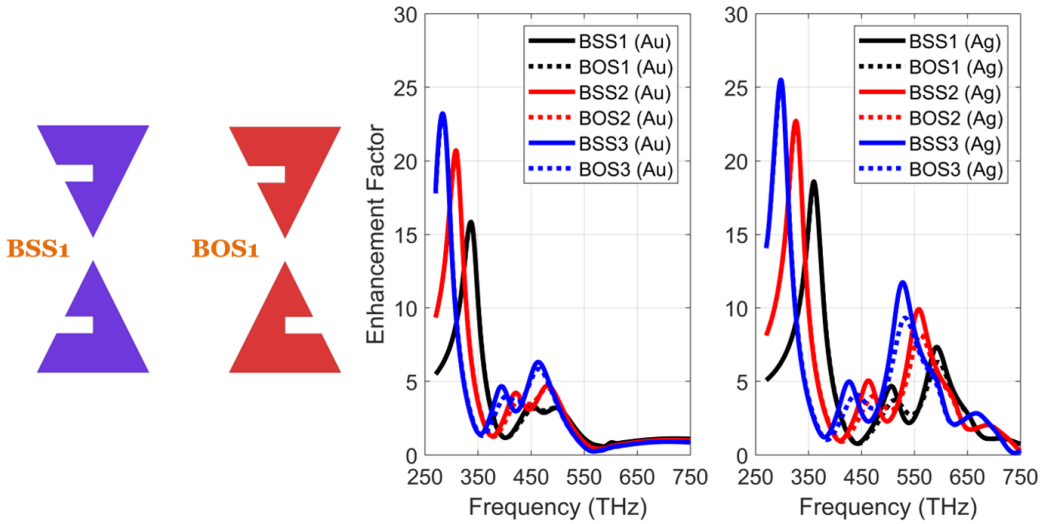

Figure 3.13: Same-side slitted (BSS1) and opposite-side slitted (BOS1) geometries (left) and frequency-dependent enhancement factor values of slitted Ag and Au B1, B2, and B3 geometries (right).

slit position. For the slits at 25 nm from the tips, the primary enhancement ability becomes even stronger in comparison to the original geometry. Although it demonstrates lower enhancement values compared to the original geometry, the slitted geometry with slits at 75 nm from the tips has three different resonances with similar strengths.

- As shown in Figure 3.13, when the size of the slitted geometry increases, the primary resonance shifts to lower frequencies such that it may even fall outside the interested frequency range. In addition, structures with Ag have stronger first and secondary resonances in comparison to Au structures. While the slitted Au nanoantennas show almost the same electromagnetic responses for different slit orientations, it is observed that the secondary resonances of Ag nanoantennas are stronger when using same-side slits rather than opposite-side slits.

To further investigate slitted nanoantenna designs with multiband characteristics, square nanoantenna structures, which are relatively easier to fabricate, are also considered. Opposite-sided slits are placed at the centers of the arms of S1, S2, and S3 geometries. The dimensions of the each arm of the resulting SS1, SS2, and SS3 geometries

are $100 \times 100 \times 20$ nm, $125 \times 125 \times 20$ nm, and $150 \times 150 \times 20$ nm, while they have 15, 18.75, and 22.25 nm slits, respectively. In addition, using 50 nm slit depth, a new geometry (SDS) with symmetrically located double slits on S3 is also designed. Using both Au and Ag (except for SDS design) materials, simulations are performed for slitted square nanoantennas, leading to the results given in Figure 3.14. The main resonance frequencies for SS2, SS3, and SDS geometries are all out of the frequency range. Since their secondary peaks are not sufficient enough, these designs are not as efficient as slitted bowties. Similar to the single-slitted geometries, SDS geometry has only a moderate second enhancement peak in the frequency range, which does not provide an alternative benefit.

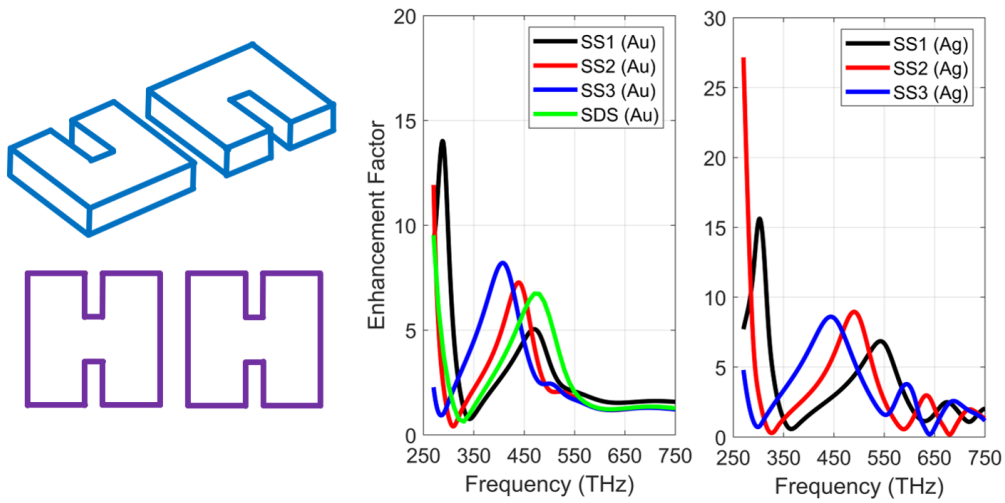

Figure 3.14: Opposite-side slitted square geometry SS1 and double-side slitted square geometry SDS (left), and frequency-dependent enhancement factor values of slitted Au SS1, SS2, SS3, and SDS geometries and Ag SS1, SS2, and SS3 geometries (right).

3.4 Shape Optimization of Nanoantennas

It has been shown in the previous section that the shape of a nanoantenna stands out as one of the most critical factors affecting its enhancement factor. Based on this observation, it is aimed to obtain improved power enhancement characteristics by making suitable alterations on simple nanoantenna geometries. Considering that

even small changes in the designs may have significant impacts on the enhancement factor, the multigrid scheme implemented with GAs is used to obtain the most successful geometries. Although the main goal in these optimization trials is to increase the enhancement value at any selected frequency, multiband or broadband responses are also sought by performing optimization simultaneously at multiple frequencies. In the following examples, geometries B1 and S1, which are easier to fabricate than others, are chosen as the primary geometries for which optimization trials are applied. Since nanostructures made of Au are more resistant to external factors, this material is selected for optimized designs, where even small details are important. The selected Au B1 and S1 geometries have relatively smaller power enhancement values compared to other designs; therefore, the impact of optimization can be shown more clearly on them.

The selected optimization surfaces for geometries B1 and S1 are given in Figure 3.15. Due to geometrical advantages, we perform side-surface optimization for the square nanoantenna and top-surface optimization for the bowtie nanoantenna. While deformation limits for optimization trials vary, the maximum deformation limits for top surface (at $z = 10$ nm) of the bowtie nanoantenna and side surface (at $y = -50$ nm) of the square nanoantenna are given as $[-10, 20]$ nm and $[-25, 15]$ nm. The number of bits, the number of individuals for each generation, and the maximum number of generations are chosen as 10, 40, and 100, respectively, for all optimization trials. For a single-frequency optimization, the cost function is determined as the calculated enhancement factor value at the gap center, as given in Equation 3.7. The cost function for a multi-frequency optimization is chosen as the multiplication of the enhancement factor values computed at all target frequencies.

First, we describe in detail the optimization sets based on the bowtie nanoantenna (B1). Single-frequency optimization trials are performed at $360, 415,$ and 500 THz, where the original B1 design has a moderate, high, and low power enhancement values, respectively. Besides, it is aimed to increase the bandwidth with multi-frequency optimization trials by using 400 and 430 THz, which are very close to the resonance frequency. Three different optimization sets using different parameters are constructed to increase the enhancement values at the given frequencies. The first

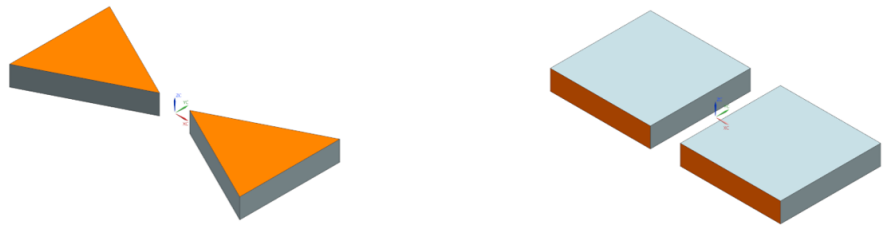

Figure 3.15: Selected deformation surfaces; upper surface at $z = 10$ nm shown with orange color for B1 (left) and side surface at $y = -50$ nm shown with orange color for S1 (right).

optimization set is constructed by using 9 grid nodes, while deformation limits are chosen as $z_d = [0, 20]$ nm for the top surface of the nanoantenna. In the second optimization set, the deformation limit range is widened as $z_d = [-10, 20]$ nm, while the number of grid nodes is kept constant. In the third optimization set, deformation limits of the second set are used, but the optimization space is expanded by increasing the number of grid nodes to 14.

In the following, the most successful geometries obtained by optimization trials are named as $\mathrm{BO}_{\mathrm{mn}}$, where BO represents the optimal bowtie geometry, m is the index of the optimization set $(1, 2, 3)$, and n is the optimization frequency index as $1, 2, 3$, and 4, corresponding to $360, 415, 500$, and 400-430 THz. The obtained cost function values with respect to generations (on the left-hand sides) and the final optimal geometries (on the right-hand sides) for optimization trials at $360, 415, 500$, and 400-430 THz are given in Figures 3.16, 3.17, 3.18, and 3.19, respectively.

Considering the results, we can first examine the relationship between the selected optimization set and the enhancement values obtained. We effectively increase the dimensions of the optimization space from the first optimization set to the third optimization set; therefore, the highest enhancement values (the multiplication of the enhancement values for the multi-frequency optimization) are obtained by the third optimization set for all cases, as expected. The second optimization set shows better results in comparison to the first optimization set with the advantage of wider

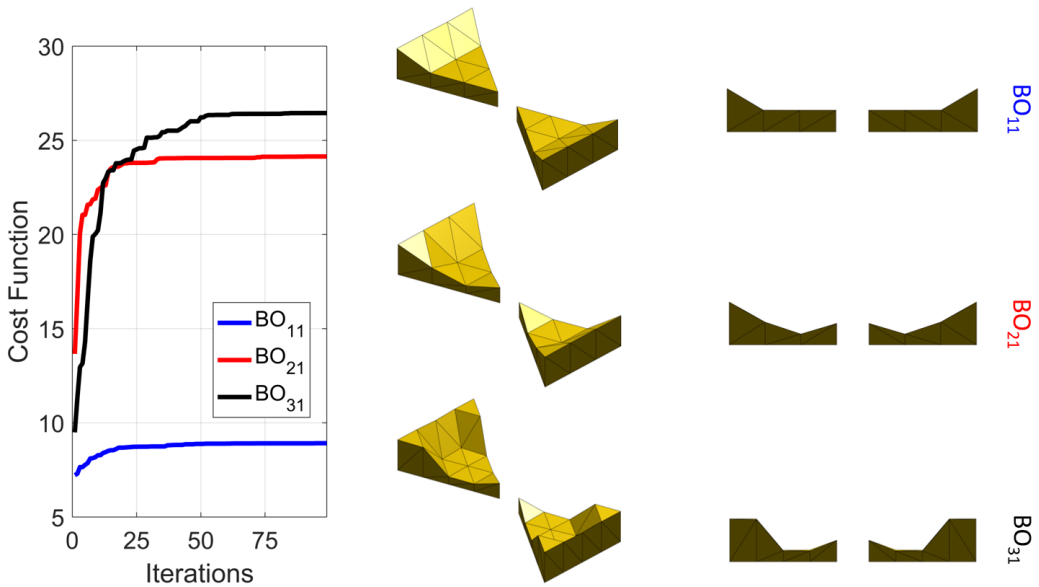

Figure 3.16: Cost function values versus generations for three optimization sets at 360 THz (left); trimetric and side views of the optimal geometries BO_{11}, BO_{21}, and BO_{31}, respectively, from top to bottom (right).

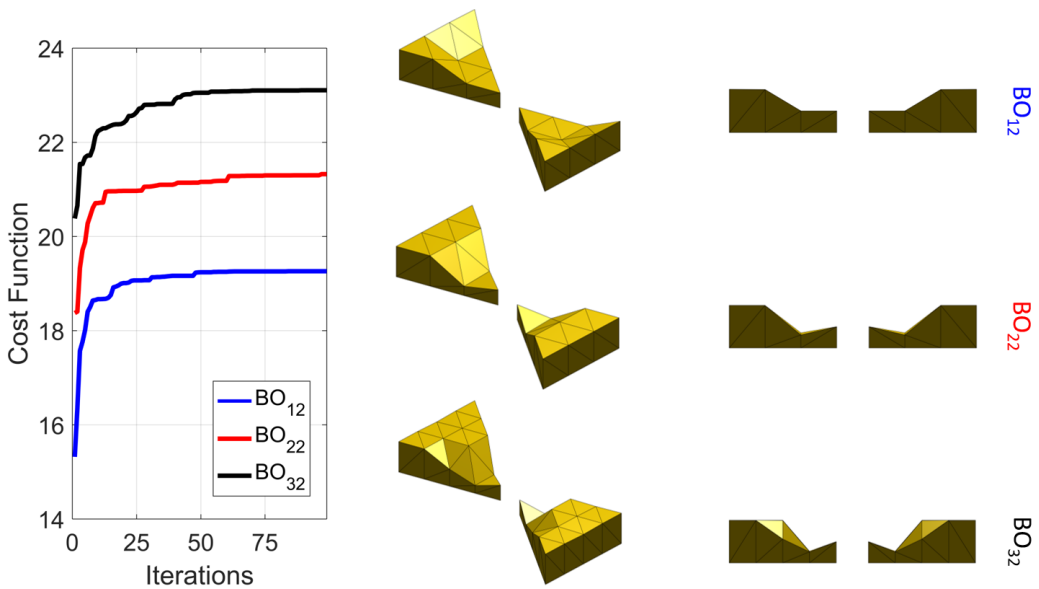

Figure 3.17: Cost function values versus generations for three optimization sets at 415 THz (left); trimetric and side views of the optimal geometries BO_{12}, BO_{22}, and BO_{32}, respectively, from top to bottom (right).

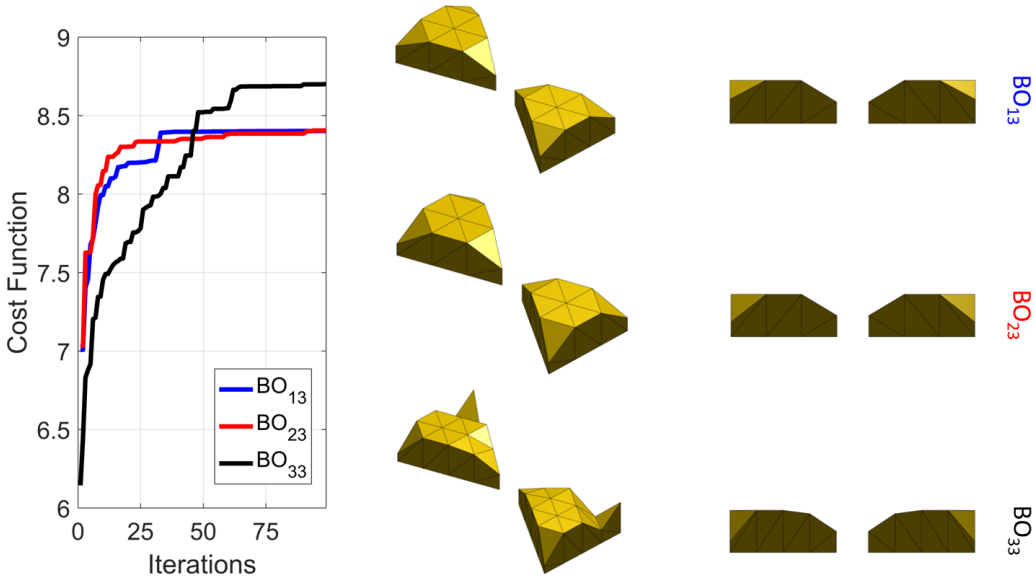

Figure 3.18: Cost function values versus generations for three optimization sets at 500 THz (left); trimetric and side views of the optimal geometries BO_{13}, BO_{23}, and BO_{33}, respectively, from top to bottom (right).

deformation intervals. However, the first optimization set generally has the fastest convergence rate to its maximum cost function value since it has a smaller optimization space with smaller deformation limits. If we consider different optimization sets at each frequency, there is a great similarity between the optimal geometries. Specifically, elevations and depressions in the final designs obtained with different optimization sets demonstrate specific characteristics depending on the optimization frequency. This is particularly obvious for the optimization trials at 500 THz, where thickening occurs at arm centers. Considering the increase in the enhancement values, the highest increment is surprisingly seen for BO_{31}, which is an optimal geometry at 360 THz, where a shift in the resonance frequency is also observed. Although the achieved values are still low at 500 THz, we can see that the original enhancement value of 3 is increased considerably with BO_{m3} geometries.

Since the cost function values in Figures 3.16-3.19 provide information only on the enhancement values at the optimization frequencies, it is generally difficult to make a comment on the characteristics of optimal geometries at other frequencies. Therefore,

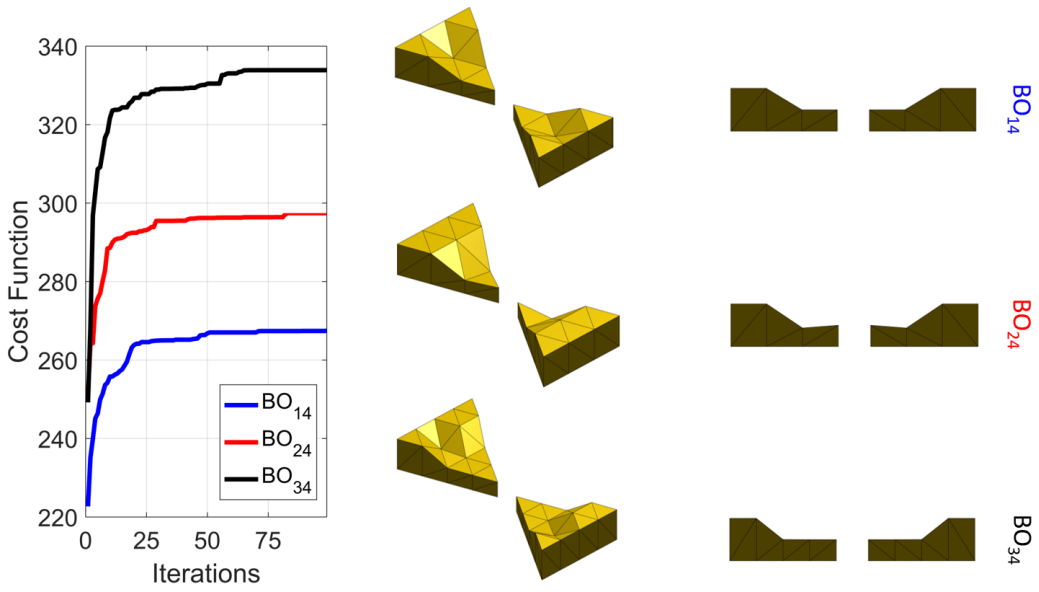

Figure 3.19: Cost function values versus generations for three optimization sets at 400-430 THz (left); trimetric and side views of the optimal geometries BO_{14}, BO_{24}, and BO_{34}, respectively, from top to bottom (right).

to gain more insight, frequency sweeps are performed for each geometry to investigate its overall frequency-dependent behavior. Enhancement factors at the gap center are computed for optimal geometries and compared with those of the original geometry in Figure 3.20.

The graphs in Figure 3.20 represent the results for the geometries obtained from the first, second, and third optimization sets, from left to right, respectively. It can be seen in the graph, the first optimization set that the optimized geometries at 360, 415, and 400-430 THz frequencies behave very similar to each other. However, if we look at the corresponding geometry images in Figures 3.16-3.19, we can actually observe significant discrepancies between the designs. While the resonance frequencies of these geometries remain nearly the same as the resonance frequency of the original geometry, 25% increase in the enhancement factor is achieved. Considering the same set, we observe that the optimization trial for 500 THz leads to a shift in the resonance frequency to 460 THz, while the enhancement factor at 500 THz is significantly increased. On the other side, considering the second and third opti-

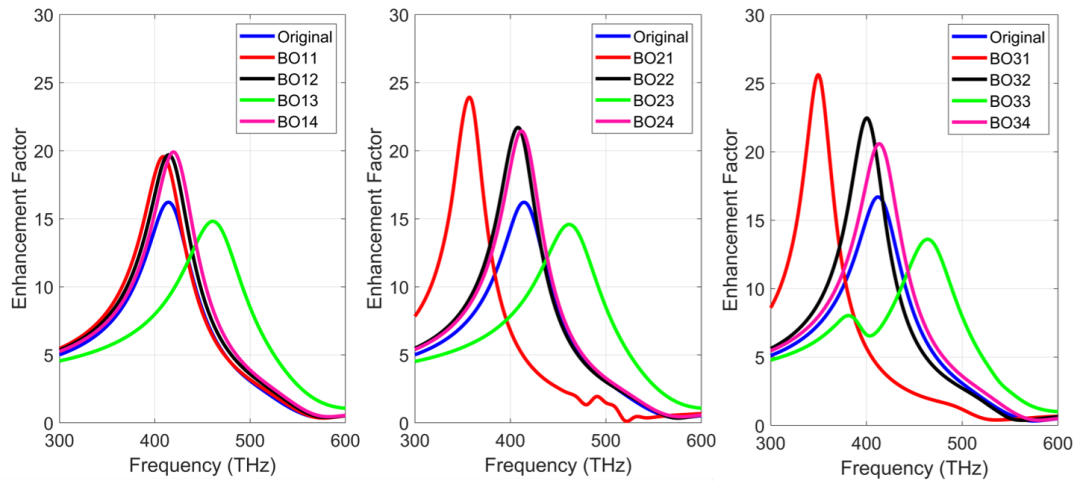

Figure 3.20: Frequency-dependent enhancement factor values for optimal geometries of the first optimization set (left), the second optimization set (middle), and the third optimization set (right) , in comparison to the enhancement of the original B1 geometry.

mization sets, the maximum enhancement values are observed at around 360 THz for BO_{21} and BO_{31} geometries, while the original resonance at 415 THz completely vanishes. Also, these geometries have the highest maximum enhancement factor values among all optimization trials made for B1 geometry. The second and third optimal geometries obtained at 415 THz (BO_{22} and BO_{32}) have stronger hot spots at the target frequency (415 THz) in comparison to the original nanoantenna; at the same time, for the third optimization set, the resonance frequency is shifted to 400 THz. While the second optimal geometry for the multi-frequency optimization (BO_{24}) has a higher peak value, the optimal geometry obtained in the third optimization set has a wider frequency band. In addition to all these, BO_{33} geometry shows a small resonance at around 380 THz, probably due to the interesting sharp jumps at the two corners of the geometry.

As already mentioned above, shape optimization is also applied to S1 geometry involving square elements. This time, the deformation surface is chosen as the side surface located at $y = -50$ nm. While the maximum number of generations and the number of bits are not changed (set as 100 and 10) in comparison to the bowtie optimization trials, the number of grid nodes is chosen as 10, and deformation limits

are set to $[-25, 0]$ nm for single-frequency optimization trials. These single-frequency optimization trials are performed at 360, 415, and 500 THz, leading to optimal geometries called SO_1, SO_2, and SO_3, respectively. As usual, the cost function is selected as the enhancement factor value at the gap centers. In Figure 3.21, in the top row from left to right, SO_1, SO_2, and SO_3 geometries are depicted, while the corresponding cost function values with respect to generations are shown in the bottom row.

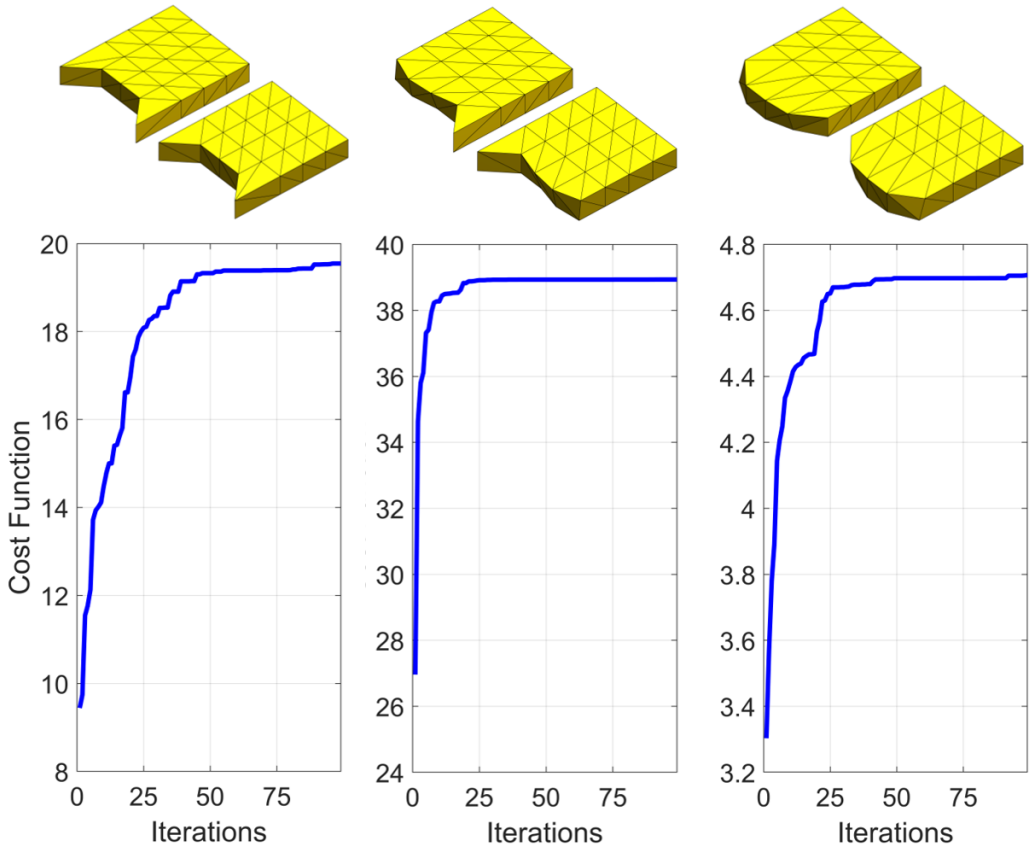

Figure 3.21: Trimetric views of the optimal geometries SO_1, SO_2, and SO_3 (top); cost function values with respect to generations for the optimal geometries with the same order (bottom).

Considering the results shown in Figure 3.21, the first discussion that can be made on the optimal geometries is that the applied modifications are relatively simple, and they are developed in a way that does not cause extreme difficulties in terms of fabrication. When the variation of the cost function with respect to generations is exam-

ined, it can be seen that the optimization trial for the SO_2 geometry is the fastest in terms of convergence to the optimal value. The enhancement factor values provided by the original geometry at the optimization frequencies are multiplied by $2.6, 3.4$, and 1.8 with SO_1, SO_2, and SO_3, respectively. SO_2 geometry, which demonstrates the greatest improvement, also stands out as the optimal geometry with the highest enhancement value obtained.

Similar to the bowtie nanoantenna, multi-frequency optimization is also applied to the square nanoantenna. In this case, deformation limits are expanded to $[-25, 15]$ nm, while the other optimization parameters are unchanged. Optimization trials are performed at 400-430 THz, 350-480 THz, 380-450 THz, and 475-565 THz, and the corresponding optimal geometries are named as SO_4, SO_5, SO_6, and SO_7, respectively. While frequencies 400-430 THz and 380-450 THz are used to increase the bandwidth of the main resonance, 350-480 THz is chosen to create new alternative peaks with possibly moderate values. On the other side, 475-565 THz is chosen to increase the enhancement factor in orange and green lights, considering that the original enhancements at these frequencies are very low. Optimal geometries obtained with the multi-frequency optimization trials, and the corresponding cost function values are given in Figure 3.22. It is seen that the modifications in the optimal geometries obtained in these optimization trials are more complex compared to the first three optimal geometries (in Figure 3.21), due to the relaxation of deformation limits. The optimization trials, in which SO_4 and SO_5 geometries obtained, show faster convergence trends than the trials for the other two geometries. Quantitatively, the enhancement factor values at the optimization frequencies are multiplied by $1.95, 4.52, 9.56$, and 1.87 by using SO_4, SO_5, SO_6, and SO_7, respectively.

The enhancement responses of optimal geometries in the entire frequency range are obtained and compared with the response of the original geometry for a more detailed examination. The enhancement factor values at the gap centers computed for S1 and optimum geometries are given in Figure 3.23. Since both cost functions and deformation limits are different, single-frequency and multi-frequency optimization trials are given in separate groups. On the left-hand side, frequency-dependent enhancement factor values for S1, SO_1, SO_2, and SO_3 nanoantennas are shown, while on the

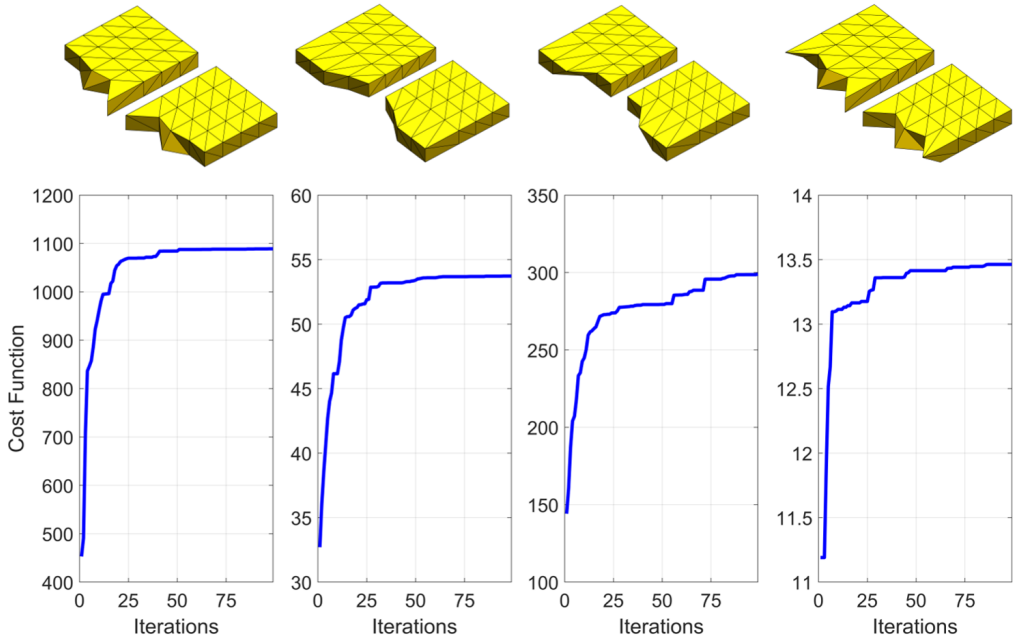

Figure 3.22: Trimetric views of the optimal geometries SO_4, SO_5, SO_6, and SO_7 (top); cost function values with respect to generations for the optimal geometries with the same order (bottom).

right-hand side, the corresponding values are demonstrated for S1, SO_4, SO_5, SO_6, and SO_7 geometries.

Considering the single-frequency optimization results in Figure 3.23, we observe that the obtained optimal geometries have much higher maximum enhancement values than the original geometry. Especially, the improvement in the enhancement factor achieved by SO_2 geometry is remarkable. Although SO_1 and SO_3 cannot provide new resonances at their optimization frequencies of 360 THz and 500 THz, respectively, they still provide shifted curves in accordance with their optimization targets. It is also interesting to note that SO_1 geometry has a lower enhancement factor value than S1 geometry at the main frequency where S1 resonates. Considering the results obtained with multi-frequency optimization trials, we observe that the obtained designs again provide much higher enhancement values than the original geometry. If the overall increase in the enhancement performance is considered, geometries obtained by multi-frequency optimization trials outperform the geometries obtained by the single-

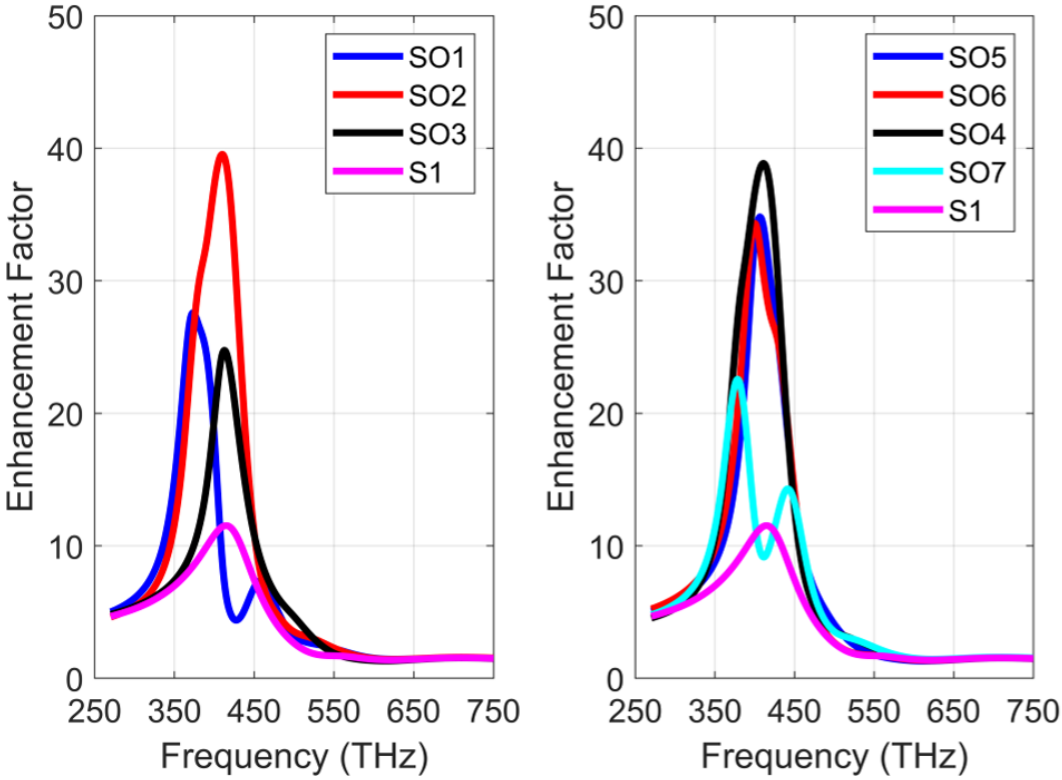

Figure 3.23: Frequency-dependent enhancement factor values for the optimal geometries of the single-frequency optimization trials (left) and the optimal geometries of the multi-frequency optimization trials (right) on the original S1 geometry.

frequency optimization trials, even though SO_2 has the highest enhancement factor value among all. It can be seen in Figure 3.23 that SO_5 and SO_6 nanoantennas have very similar enhancement responses, which is expected due to their geometrical similarities. SO_7 geometry, designed for completely different frequencies, interestingly shows a dual-band response at around the main frequency where the original geometry resonates.

In each result in Figures 3.20 and 3.23, the frequency-dependent enhancement factor is calculated at a single point, directly at the gap center ($x = 0, y = 0$, and $z = 0$). For better observation of electromagnetic responses of different designs, enhancement factor values are also obtained at multiple points on a cross-section in the x-y plane at $z = 0$. Specifically, in an area defined with limits $x = [-250, 250]$ nm and $y = [-250, 250]$ nm, enhancement factor values are calculated at 201 points

in both x and y directions using Equation 3.7. The obtained 201×201 matrices are visualized as near-zone images to observe the formed hot spots at around the nanoantennas. In these images, the enhancement factor values are limited between 0 and 30, and a colormap called "hot" is used to assign colors to values, where the highest value is expressed in white color and the lowest value in black color. The near-zone enhancement characteristics of the original bowtie geometry (B1) and the optimal bowtie geometries of the 3rd optimization set (BO_{31}, BO_{32}, BO_{33}, and BO_{34}) at excitation frequencies of $360, 400, 415, 430$, and 500 THz are given in Figure 3.24. Similarly, Figure 3.25 represents the near-zone enhancement factor images of the original square geometry (S1) and the optimal geometries obtained via single-frequency optimization (SO_1, SO_2, and SO_3) at excitation frequencies of $360, 415$, and 500 THz. Finally, in Figure 3.26, we present the near-zone enhancement factor values for the original square geometry (S1) and the optimal geometries obtained via multi-frequency optimization (SO_4, SO_5, SO_6, and SO_7) at excitation frequencies of $350, 380, 400, 430, 450, 480$, and 560 THz. Our observations are as follows.

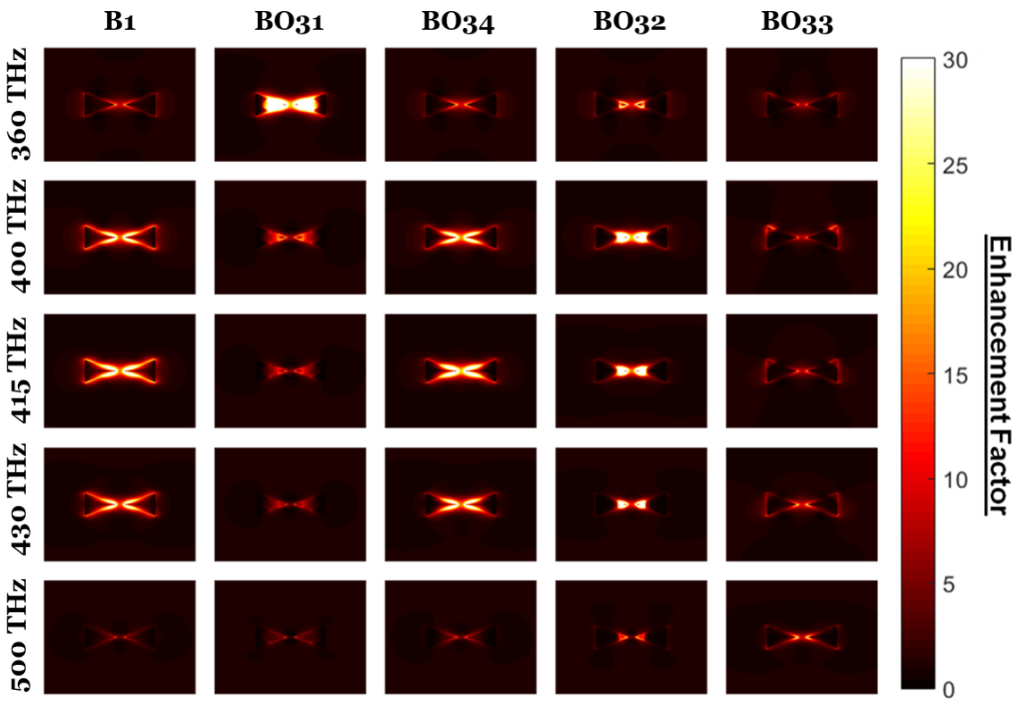

Figure 3.24: Near-zone enhancement characteristics of B1, BO_{31}, BO_{34}, BO_{32}, and BO_{33} geometries at $360, 400, 415, 430$, and 500 THz.

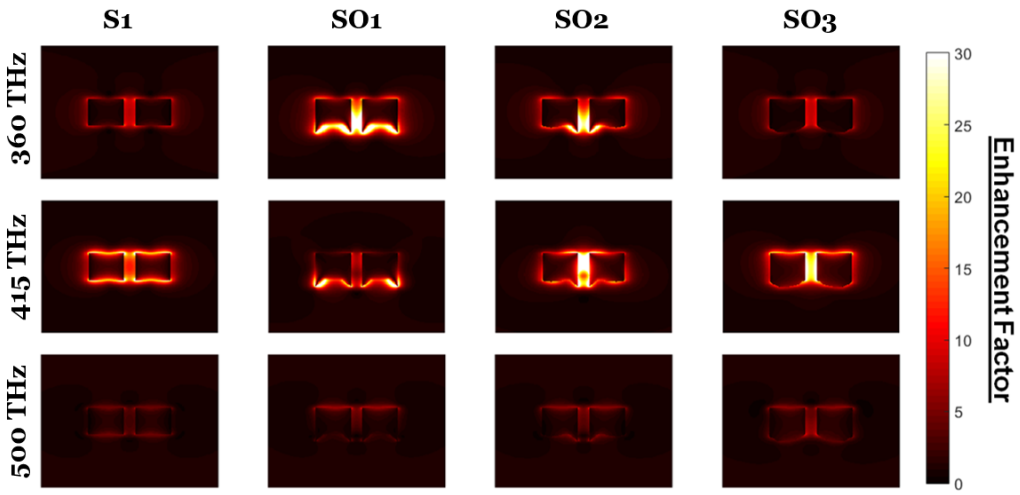

Figure 3.25: Near-zone enhancement characteristics of S1, SO_1, SO_2, and SO_3 geometries at $360, 415$, and 500 THz.

- All bowtie geometries form hot spots in their gaps between the sharp tips by localizing incoming electromagnetic waves. However, not only the intensity of the localized power, but also the position-dependent distribution pattern depends on the geometry. For example, while BO_{32} geometry shows the strongest responses in a small area between its tips, BO_{31} geometry focuses the incoming light wave in a way that it diffuses effectively into the structure. In contrast, the responses of the original geometry and BO_{34} demonstrate remarkable similarities, while relatively strong responses are observed in 400-430 THz range with the optimal geometry.

- The highest enhancement factor value for the original square nanoantenna is actually seen at around the opposing corners, rather than the center of the gap. It can be seen that this undesired characteristics can be eliminated completely with the geometries obtained via single-frequency optimization trials. While a one-sided field localization by SO_2 geometry at 360 THz is shaped at around the sharp surface extension, the focused electromagnetic wave by SO_3 geometry at 415 THz spreads quite evenly between the opposite edges. In addition, the spots where SO_1 geometry achieves the strongest enhancement factor value at 415 THz are sharp surface extensions that are far away from the gap.

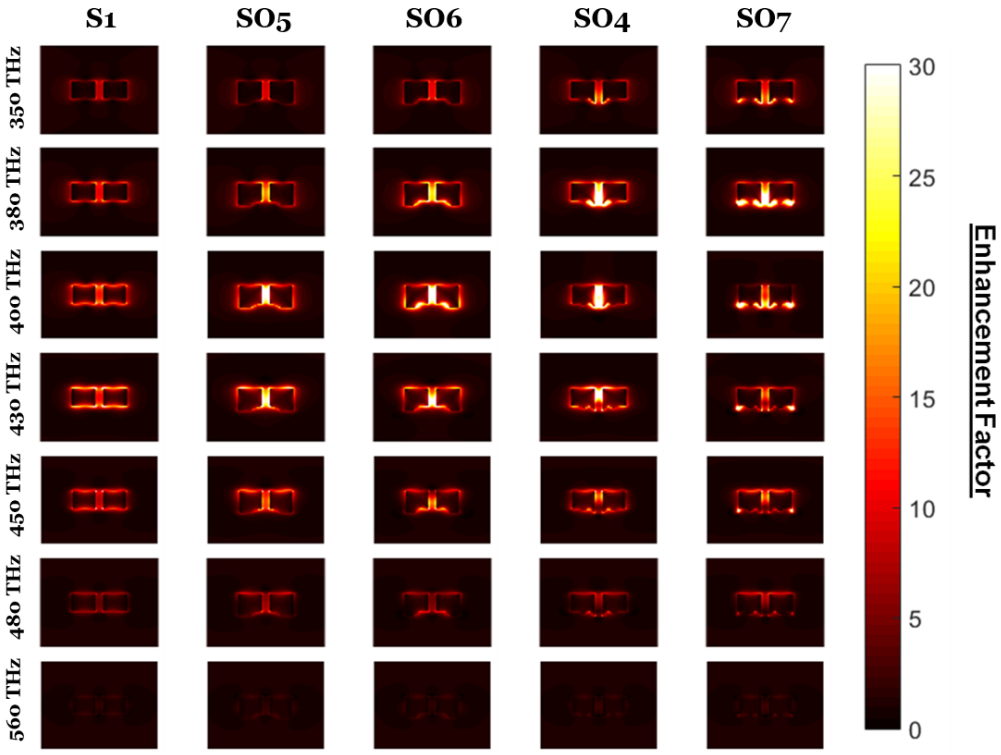

Figure 3.26: Near-zone enhancement characteristics of S1, SO_5, SO_6, SO_4, and SO_7 geometries at $350, 380, 400, 430, 450, 480$, and 560 THz.

- SO_5 and SO_6 geometries obtained in the multi-frequency optimization set show extremely similar characteristics in the frequency-dependent enhancement factor curves shown in Figure 3.23. When the near-zone characteristics of these geometries are analyzed, however, differences in the localized fields on the deformed edges are noticeable, while extremely similar responses are still observed at gap centers. While the most powerful hot spots are obtained with SO_4 geometry, it is possible to obtain hot spots in multiple locations with SO_7 geometry (e.g., at 380 THz).

3.5 Comparison of Nanoantenna Designs

In the previous sections, simple nanoantenna designs using different design parameters, as well as more complex nanoantenna designs obtained via slitting and shape

optimization are introduced. Some of these designs have strong power enhancement capabilities, some of them show multiband resonance properties, and others have relatively common characteristics, while they all stand out with their potential to be fabricated. In this section, we summarize the main properties of all designs and compare them with the available designs in the literature. Since plasmonic nanoantennas draw the attention of scientists from many different branches, there are several different definitions of the enhancement factor in the literature. In this respect, nanoantenna designs selected from the literature are simulated with the methods used in the thesis for consistent and fair comparisons.

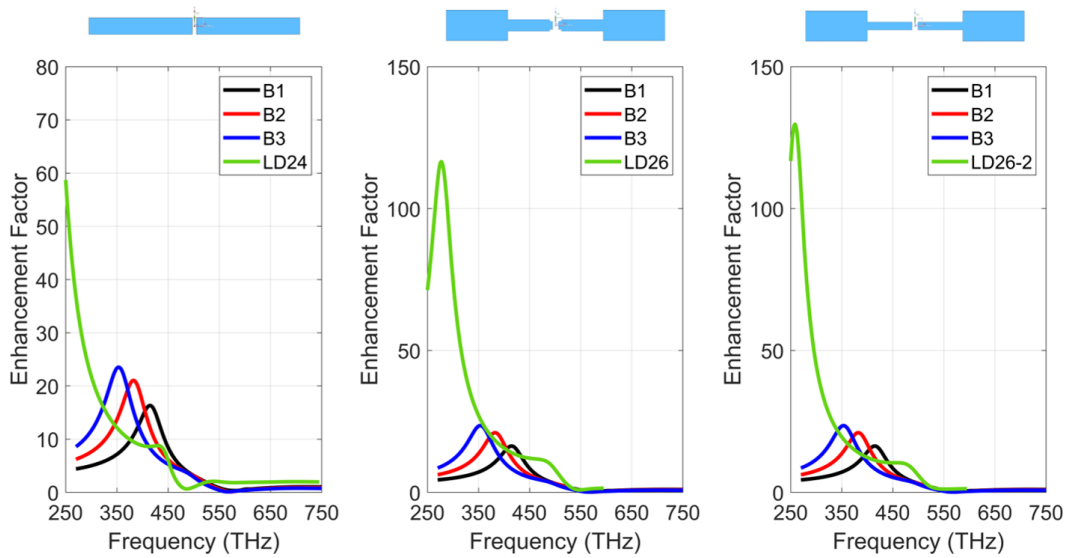

Figure 3.27: Top view of geometries LD24, LD26, and LD26-2 (top) frequency-dependent enhancement factor values (bottom).

Different sizes and shapes are preferred while selecting prominent geometries from the literature, while the material is selected as Au. Since the diversity is increased with these geometries, the advantages and disadvantages of the designs presented in this thesis become more clear. The geometries of the nanoantenna designs (LB3 and LB3-2 [20], LD7 [11], LB11 [39], LD13 [40], LB14 and LD14 [41], LD18 and LD18-2 [42], LD24 [43], LD26 and LD26-2 [4], LB33 [44], LB37 [45]) taken from the literature and the frequency-dependent enhancement factor values for these geometries are shown in Figures 3.27, 3.28, 3.29, and 3.30. While all details of these designs are included in the cited references,, parameters such as their maximum di-

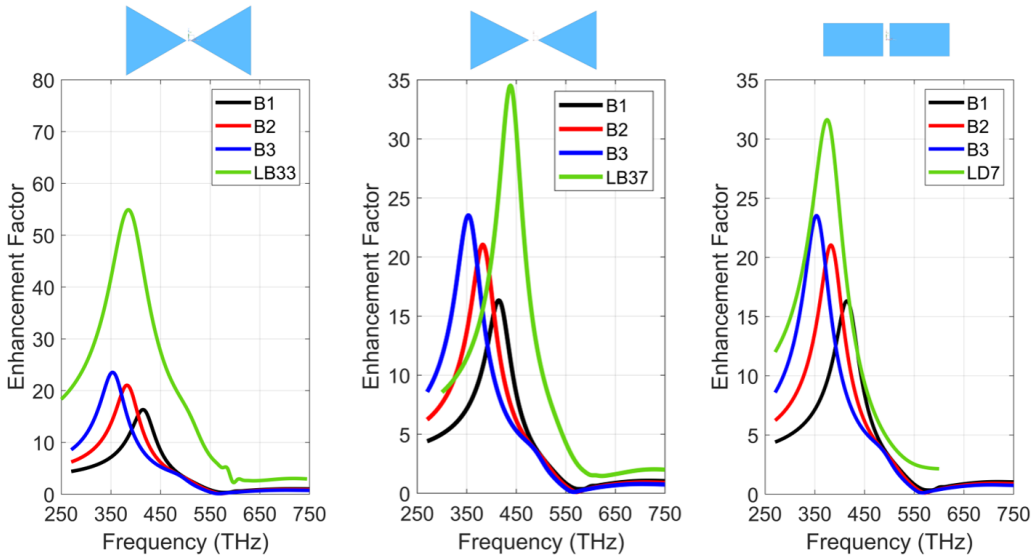

Figure 3.28: Top view of geometries LB33, LB37, and LD7 (top) frequency-dependent enhancement factor values (bottom).

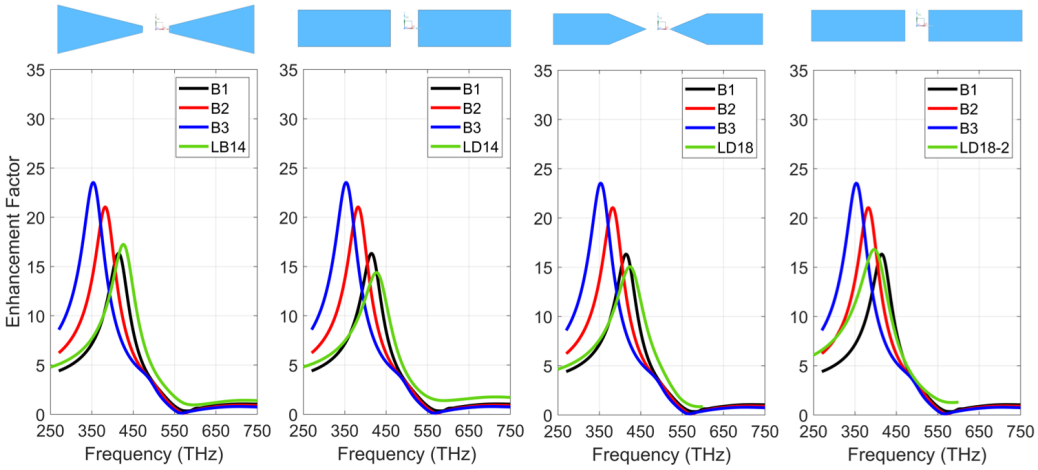

Figure 3.29: Top view of geometries LB14, LD14, LD18, and LD18-2 (top) frequency-dependent enhancement factor values (bottom).

mensions and gap sizes are further listed in Table 3.5.

The enhancement properties of the geometries from the literature are depicted together with the simple B1, B2, and B3 (bowtie) geometries to facilitate comparisons. In Figure 3.27, the responses of the geometries that have very small gap sizes and high aspect ratios are shown. These geometries achieve extremely high enhancement fac-

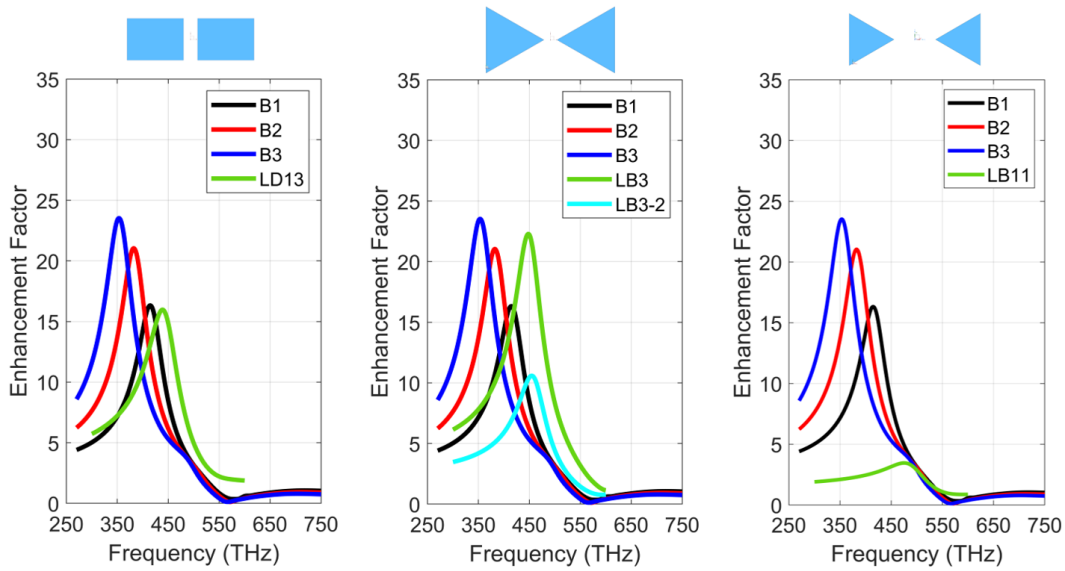

Figure 3.30: Top view of geometries LD13, LB3, LBD3-2, and LB11 (top) frequency-dependent enhancement factor values (bottom).

tor values while their resonance characteristics barely remain in the frequency range of interest. In fact, the resonance frequency of LD24 is completely out of the frequency regime. The enhancement characteristics of structures, which have smaller gap sizes but are geometrically similar to the geometries proposed in this thesis, are depicted in Figure 3.28. With very narrow gaps, these geometries can reach higher enhancement factors in comparison to the simple designs presented in this thesis. Nevertheless, optimized designs, such as SO_2, can provide better enhancements than LD37 and LD7, despite these optimized designs have much wider gaps. The enhancement factor values of designs, for which both maximum dimensions and gap sizes are similar to those of B1, B2, and B3 geometries, are shown in Figure 3.29. Obviously, these designs perform worse than the simple bowtie nanoantennas. In the last figure (Figure 3.30), geometries that do not show sufficient enhancement features due to their gap sizes and/or shapes are included, again in comparison to B1, B2, and B3.

In order to make quantitative comparisons between the presented nanoantenna geometries, all designs are listed in Tables 3.1, 3.2, 3.3, 3.4, and 3.5, including their enhancement factors. Each row in these tables includes nanoantenna tag, material, maximum dimension, gap size, lower and upper limits of the enhancement resonance

Table 3.1: Design parameters of simple bowtie and square nanoantenna geometries, and their frequency-dependent power enhancing characteristics.

NA	Material	Size	Gap	Band	Bandwidth	Enhancement
B1	Au	230 nm	30 nm	362-452 THz	90 THz	16.3
B2	Au	280 nm	30 nm	332-421 THz	89 THz	21.0
B3	Au	330 nm	30 nm	300-395 THz	95 THz	23.5
B1	Ag	230 nm	30 nm	405-502 THz	97 THz	19.6
B2	Ag	280 nm	30 nm	355-462 THz	107 THz	22.2
B3	Ag	330 nm	30 nm	315-428 THz	113 THz	23.5
S1	Au	230 nm	30 nm	319-462 THz	143 THz	11.5
S2	Au	280 nm	30 nm	323-416 THz	93 THz	20.7
S3	Au	330 nm	30 nm	270-395 THz	125 THz	14.6
S1	Ag	230 nm	30 nm	343-518 THz	175 THz	12.0
S2	Ag	280 nm	30 nm	336-454 THz	118 THz	20.6
S3	Ag	330 nm	30 nm	270-425 THz	155 THz	14.1

(double row in case of multiband characteristics), resonance bandwidth (double row in case of multiband characteristics), and maximum enhancement factor, respectively. The bandwidth is determined by the frequencies where the enhancement factor values are half of the maximum value. The multiband resonance feature of a nanoantenna design is determined by an increase of at least one-quarter after the maximum enhancement factor value decreases by at least 50%. Considering all results in the tables, we reach two fundamental conclusions:

- It is possible to obtain higher enhancement factors than presented in this thesis; but this is possible only with narrower gaps. Specifically, none of the designs in the literature can beat the optimized designs in this thesis, if the gap width is set to 30 nm. On the other hand, our selection of 30 nm is on purpose; this is a reasonable width for most fabrication setups. From this perspective, we believe that some of the extremely high enhancement results in the literature are impressive but misleading, as they provide results for single samples (with

Table 3.2: Design parameters of optimum bowtie nanoantenna geometries, and their frequency-dependent power enhancing characteristics.

NA	Material	Size	Gap	Band	Bandwidth	Enhancement
BO_{11}	Au	230 nm	30 nm	364-443 THz	79 THz	19.6
BO_{21}	Au	230 nm	30 nm	326-381 THz	55 THz	23.9
BO_{31}	Au	230 nm	30 nm	321-372 THz	51 THz	25.6
BO_{12}	Au	230 nm	30 nm	370-449 THz	79 THz	19.7
BO_{22}	Au	230 nm	30 nm	368-438 THz	70 THz	21.7
BO_{32}	Au	230 nm	30 nm	364-429 THz	65 THz	22.5
BO_{13}	Au	230 nm	30 nm	392-507 THz	115 THz	14.8
BO_{23}	Au	230 nm	30 nm	392-508 THz	116 THz	14.6
BO_{33}	Au	230 nm	30 nm	411-508 THz	97 THz	13.6
BO_{14}	Au	230 nm	30 nm	375-454 THz	79 THz	19.9
BO_{24}	Au	230 nm	30 nm	372-443 THz	71 THz	21.5
BO_{34}	Au	230 nm	30 nm	370-447 THz	77 THz	20.6

very narrow gaps) that are difficult to replicate, as well as to fabricate in mass amounts.

- None of the designs in the literature possess a multiband characteristics so that the slitted geometries presented in this thesis become unique designs that can provide multiband operations with relatively simple structures.

3.6 Concluding Remarks

In this chapter, design, simulation, and optimization of plasmonic nanoantennas are considered. When nanoantennas are excited by light, they enhance incoming power density in the subwavelength areas called hot spots. The choices of the nanoantenna design parameters, such as shape, material, size, thickness, gap size, and curved edges have massive impacts on the power enhancing property of nanoantennas. Although the effects of these parameters are shown separately, they should be considered as a

Table 3.3: Design parameters of optimum square nanoantenna geometries, and their frequency-dependent power enhancing characteristics.

NA	Material	Size	Gap	Band	Bandwidth	Enhancement
SO_1	Au	230 nm	30 nm	347-404 THz	57 THz	27.6
SO_2	Au	230 nm	30 nm	364-438 THz	74 THz	39.5
SO_3	Au	230 nm	30 nm	384-445 THz	61 THz	24.8
SO_4	Au	230 nm	30 nm	368-440 THz	72 THz	38.9
SO_5	Au	230 nm	30 nm	380-443 THz	63 THz	34.8
SO_6	Au	230 nm	30 nm	374-444 THz	70 THz	34.3
SO_7	Au	230 nm	30 nm	349-401 THz	52 THz	22.6

whole, which makes designs of nanoantennas with high enhancement factors quite tricky. Also, due to limitations in fabrication, it may not be possible to replicate ideal geometries of designs. A slit-opening method is implemented for multiband responses by relatively simple designs, and it is shown that secondary resonances effectively created by this approach. Furthermore, enhancement factors of simple nanoantenna designs are improved by utilizing GA optimization. We show that optimal square nanoantenna geometries exhibit excellent enhancement values. Finally, prominent nanoantenna designs from the literature are simulated and compared with the designs presented in this thesis. The results demonstrate the superior properties of the optimized nanoantennas (e.g., SO_4 in terms of maximum enhancement) in comparison to the designs with the same (reasonable) gap width from the literature.

Table 3.4: Design parameters of slitted bowtie nanoantenna geometries, and their frequency-dependent power enhancing characteristics.

NA	Material	Size	Gap	Band	Bandwidth	Enhancement
BSS_1	Au	230 nm	30 nm	301-355 THz	54 THz	15.9
BSS_2	Au	280 nm	30 nm	276-328 THz	52 THz	20.7
BSS_3	Au	330 nm	30 nm	270-304 THz 428-503 THz	34 THz 75 THz	23.2
BOS_1	Au	230 nm	30 nm	301-355 THz	54 THz	15.9
BOS_2	Au	280 nm	30 nm	276-328 THz	52 THz	20.7
BOS_3	Au	330 nm	30 nm	270-304 THz 384-503 THz	34 THz 119 THz	23.2
BSS_1	Ag	230 nm	30 nm	327-381 THz 563-634 THz	54 THz 71 THz	18.4
BSS_2	Ag	280 nm	30 nm	293-348 THz 529-602 THz	55 THz 73 THz	22.5
BSS_3	Ag	330 nm	30 nm	270-319 THz 499-576 THz	49 THz 77 THz	25.5
BOS_1	Ag	230 nm	30 nm	327-381 THz 558-664 THz	54 THz 86 THz	18.4
BOS_2	Ag	280 nm	30 nm	293-348 THz 526-619 THz	55 THz 93 THz	22.5
BOS_3	Ag	330 nm	30 nm	270-319 THz 497-594 THz	49 THz 97 THz	25.5

Table 3.5: Design parameters of nanoantenna geometries taken from the literature, and their frequency-dependent power enhancing characteristics..

NA	Material	Size	Gap	Band	Bandwidth	Enhancement
LB3	Au	180 nm	17 nm	392-486 THz	94 THz	22.3
LB3-2	Au	180 nm	30 nm	387-492 THz	105 THz	10.6
LD7	Au	247 nm	13 nm	308-421 THz	113 THz	31.6
LB11	Au	280 nm	80 nm	300-534 THz	234 THz	3.46
LD13	Au	180 nm	13 nm	399-464 THz	65 THz	16.3
LB14	Au	230 nm	30 nm	363-467 THz	104 THz	17.2
LD14	Au	230 nm	30 nm	347-472 THz	125 THz	14.4
LD18	Au	270 nm	30 nm	349-474 THz	125 THz	15.1
LD18-2	Au	270 nm	30 nm	314-446 THz	132 THz	16.8
LD24	Au	510 nm	10 nm	215-259 THz	44 THz	92.7
LD26	Au	179 nm	10 nm	240-309 THz	68 THz	117
LD26-2	Au	179 nm	10 nm	228-285 THz	57 THz	130
LB33	Au	310 nm	10 nm	309-450 THz	141 THz	54.9
LD37	Au	162 nm	12 nm	390-475 THz	85 THz	34.1

CHAPTER 4

DESIGN AND SIMULATION OF NANOANTENNA-BASED PLASMONIC STRUCTURES FOR IMAGING AND SENSING APPLICATIONS

This chapter is devoted for investigating the use of high power-enhancing nanoantenna-based structures for different imaging and sensing applications. Considering the followed strategies, the chapter is divided into two main sections. In the first section, near-zone imaging of subwavelength nanoparticles by using nanoantenna arrays is presented. In the second section, far-zone detection of even smaller particles by the nano-hole structures based on nanoantenna principles is presented. The results demonstrate the feasibility of single-particle detection and sensing using well-designed nanostructures.

4.1 Nanoantenna Arrays for Particle Detection

In this section, a computational study of nanoantenna arrays for the detection of nearby nanoparticles is presented. Nanoantenna arrays may enable sensing subwavelength nanoparticles based on their enhancement distribution responses to alterations in their host media. Even though other methods (e.g., involving light sources and photodetectors) are commonly used to detect the types of nanoparticles presented in this part, using nanoantenna arrays can greatly facilitate the detection process. Specifically, instead of directly measuring scattered fields of nanoparticles by carefully locating them at suitable positions, the effects of nanoparticles on the electromagnetic responses of nanoantenna arrays are investigated for both their detection and identification. Computational results demonstrate the capabilities of nanoarrays for this kind of novel detection and identification systems.

4.1.1 Simulation Environment

As for all results discussed in Chapter 3, simulations are carried out in the frequency domain assuming time-harmonic sources. The considered problems involve nanoarrays and nanoparticles that typically have different electrical parameters. Surfaces are discretized by using triangles, while equivalent electric and magnetic currents are expanded with the RWG functions. Scattering problems are formulated by using MCTF, which has been extended to composite (multi-region) scenarios as described in Chapter 2. Electrical parameters of Ag, which is the main material for nanoantennas, are extracted from Lorentz-Drude model. The considered nanoparticles are also modeled as penetrable, and typically as dielectrics that are generally difficult to detect in comparison to metallic particles. MLFMA is used with different tree structures in different regions, i.e., the host medium (vacuum), inside particles (dielectric), and inside nanoantennas (plasmonic). In plasmonic regions, MLFMA interactions are truncated whenever possible without sacrificing the accuracy. In these simulations, the Ag nanoantenna geometry (see Figure 3.1) with the dimensions of $214 \times 100 \times 20$ nm is used, where the gap size is 14 nm. The selected nanoantenna geometry is active with high enhancement factors in the 400-500 THz range. The frequency is fixed to 450 THz in the following results, while the nanoantenna arrays and nanoparticles are excited by light sources from the top.

4.1.2 Periodicity of Elements

Since array elements (bowtie nanoantennas) strongly interact with each other, distances between them are critical for their performances. Placing nanoantennas far away from each other would reduce the interactions between them, while this decreases the reliability of the particle detection, especially for small-scale objects. In fact, electromagnetic interactions between nanoantennas can be employed in a useful way to improve the performances of individual elements. As an example, Figure 4.1 presents the power enhancement factor at the gap of an Ag bowtie nanoantenna, when another identical nanoantenna is placed at different locations. The results show that the enhancement factor is quite sensitive to the distance between the nanoantennas when they are vertically aligned. Specifically, the enhancement factor can exceed 65,

which is higher than the enhancement by a single nanoantenna (approximately 45 at 450 THz, as shown in Figure 3.1), when the center-to-center distance is 475 nm. It is remarkable that placing nanoantennas horizontally always deteriorates the enhancement factor, which must be considered in two-dimensional arrangements. As shown in Figure 4.2 for a 2×2 array of Ag nanoantennas, the enhancement factor can be kept above 60 at around 445 THz, if the periodicity (in horizontal and vertical directions) is fixed to 450-500 nm.

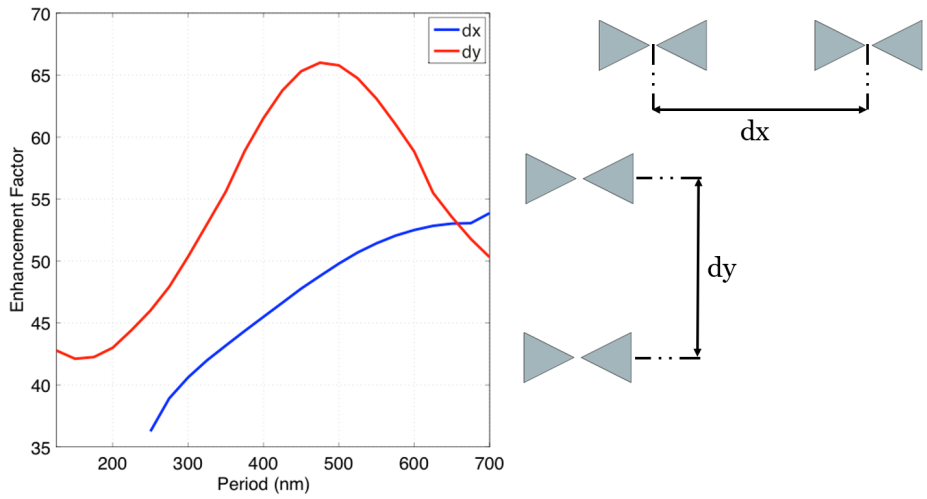

Figure 4.1: Frequency-dependent enhancement factor at the gap of an Ag bowtie nanoantenna, when another identical nanoantenna is placed at different nearby locations.

4.1.3 Plasmonic Nanoparticle Detection

As the first set of results about particle detection, spherical Ag particles with different diameters from 50 nm to 300 nm are considered. The particles are located in the plane of a 3×3 nanoantenna array. In addition to different sizes, different locations for the particles are considered in order to investigate their effects in the near-zone characteristics. Figure 4.3 presents the electric field intensity ($[-10, 20]$ dBV/m range), the magnetic field intensity ($[-60, -30]$ dBA/m range), and the power density ($[-40, -10]$ dBW/sm range), as well as the point-wise power enhancement factor distributions for 25 different cases. The near-zone samples are selected in the array plane

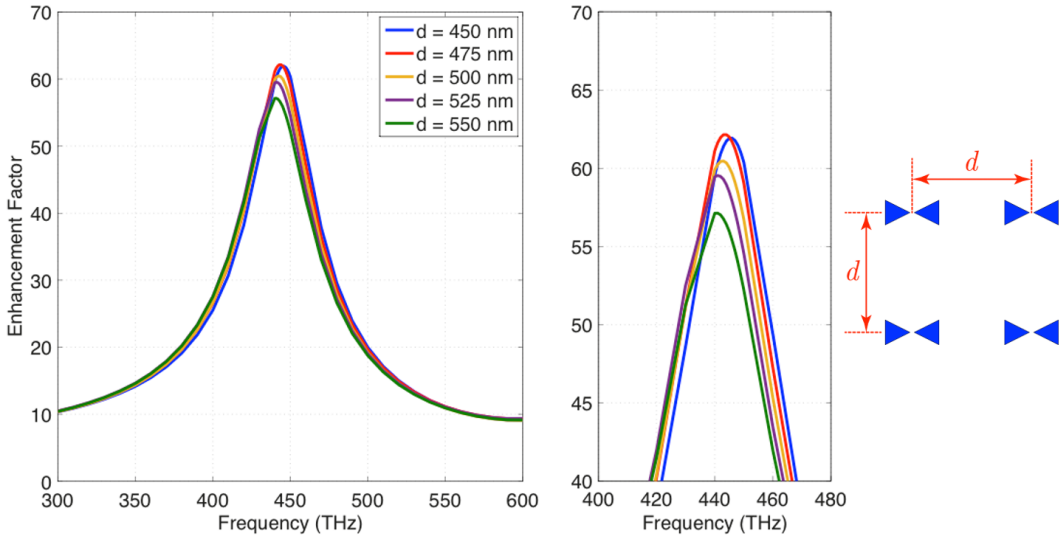

Figure 4.2: Frequency-dependent enhancement factor at the gap of an Ag bowtie nanoantenna in an arrangement of 2×2 nanoantennas with different periodicities.

($z = 0$) so that the particles are also seen as dark circles, while this does not directly mean detection since the sampling plane (that cuts the particles) may not be realistic for a detection application. On the other hand, the aim here is to observe the response of nanoantennas to the existence of particles. The smallest particle with 50 nm diameter does not lead to any visible response (first column in each panel), while near-zone field and density distributions significantly change as the particle size grows. This is particularly seen in the near-zone electric field intensity plots, where the coupling between the particles and nearby nanoantennas is observed as relatively large fields. In the power enhancement plots, nanoparticles lead to decreased enhancement values (faded hot spots), which can be interpreted as shadowing depending on the particle size.

Next, more realistic cases are considered, where a spherical particle is moving above a 5×5 array of nanoantennas. Figure 4.4 presents two different scenarios for the movement of a spherical Ag particle of diameter 600 nm. The bottom of the sphere is 10 nm away from nanoantenna surfaces. Figure 4.5 presents the electric field intensity, the magnetic field intensity, the power density, and the point-wise enhancement factor in the array plane, when the particle moves as depicted on the left-hand side of Figure 4.4. The movement of the particle is clearly observed as deteriorated near-

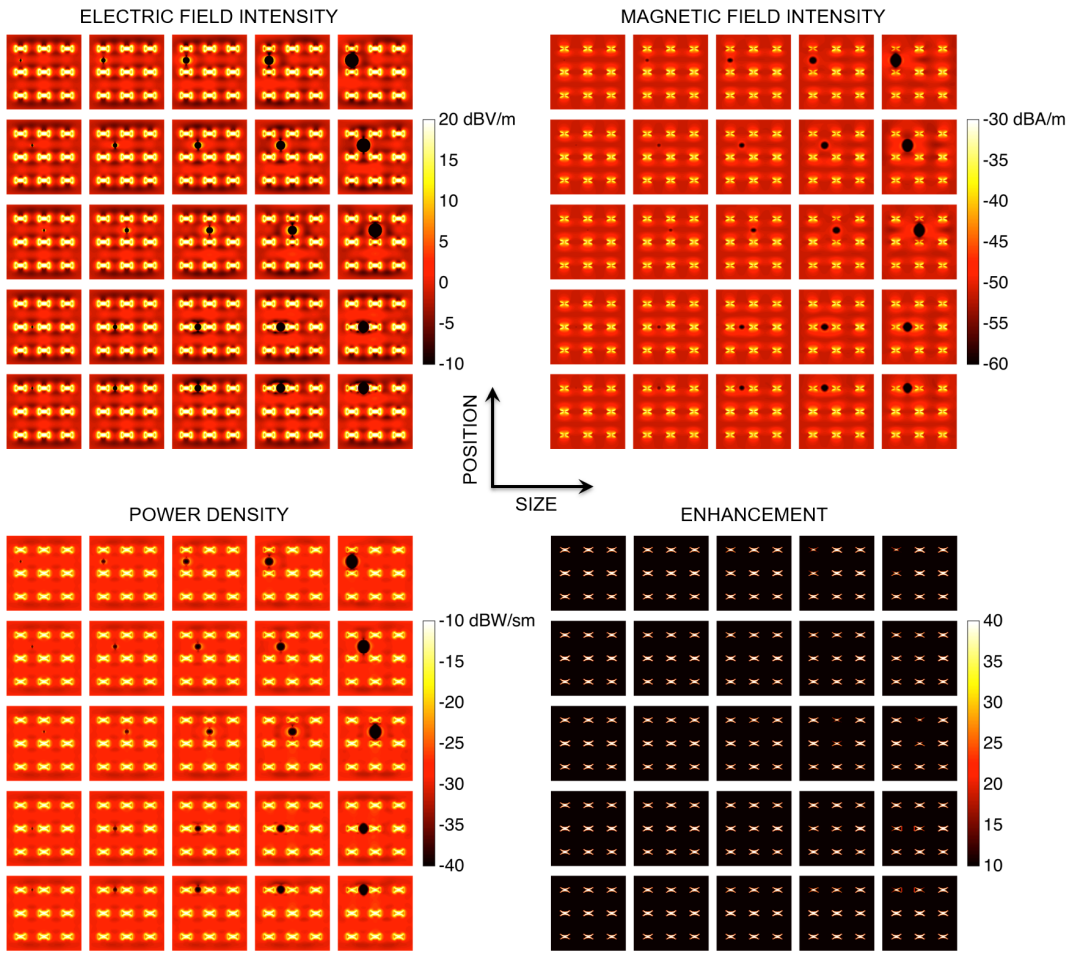

Figure 4.3: Near-zone characteristics of an array of 3×3 nanoantennas when Ag particles with different sizes are located in the array plane. The periodicity of the array is 500 nm, while the particle diameter changes from 50 nm to 300 nm (for the first three locations) or from 50 nm to 250 nm (for the last two locations).

zone distributions, particularly as shadowed nanoantennas. This shadowing effect is significant especially in the enhancement plots, where dark areas occur depending on the location of the particle. Figure 4.6 presents similar results when the movement of the particle is as described on the right-hand side of Figure 4.4. In addition to the successful tracking of the particle, it is remarkable that the results in Figure 4.6 differ from those in Figure 4.5, i.e., the vertical location of the particle can also be identified from near-zone distributions.

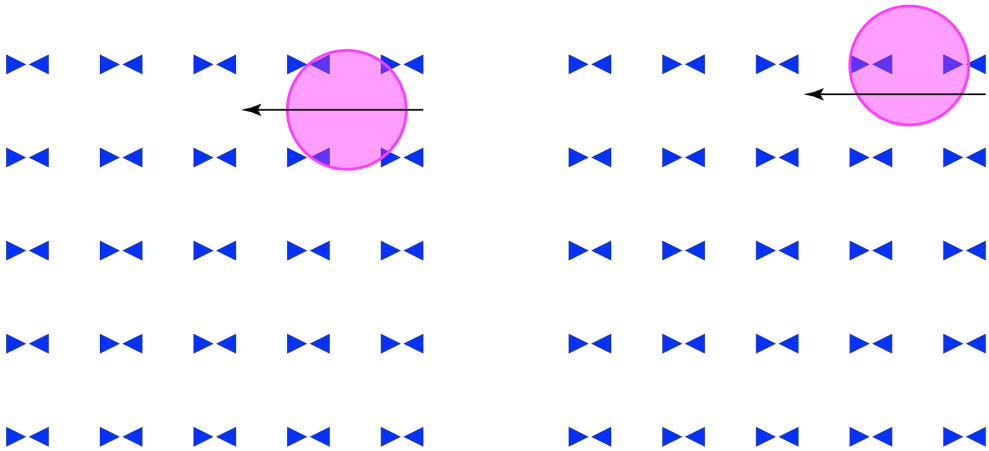

Figure 4.4: Movement of a spherical particle of diameter 600 nm above a 5×5 array of nanoantennas with 475 nm periodicity. Moving on a path between two rows (left). Moving on a path above the first row of nanoantennas (right).

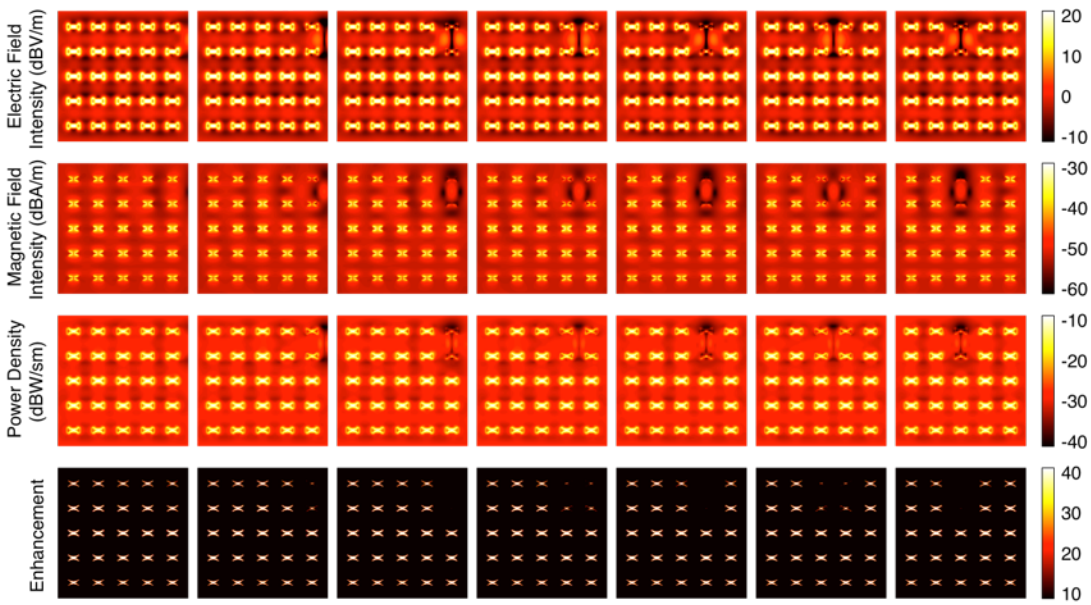

Figure 4.5: Near-zone characteristics of an array of 5×5 nanoantennas when an Ag particle of diameter 600 nm moves above the array as described in Figure 4.5 (left). The periodicity of the array is 475 nm. The bottom of the particle is 10 nm away from the top surface of the nanoantennas.

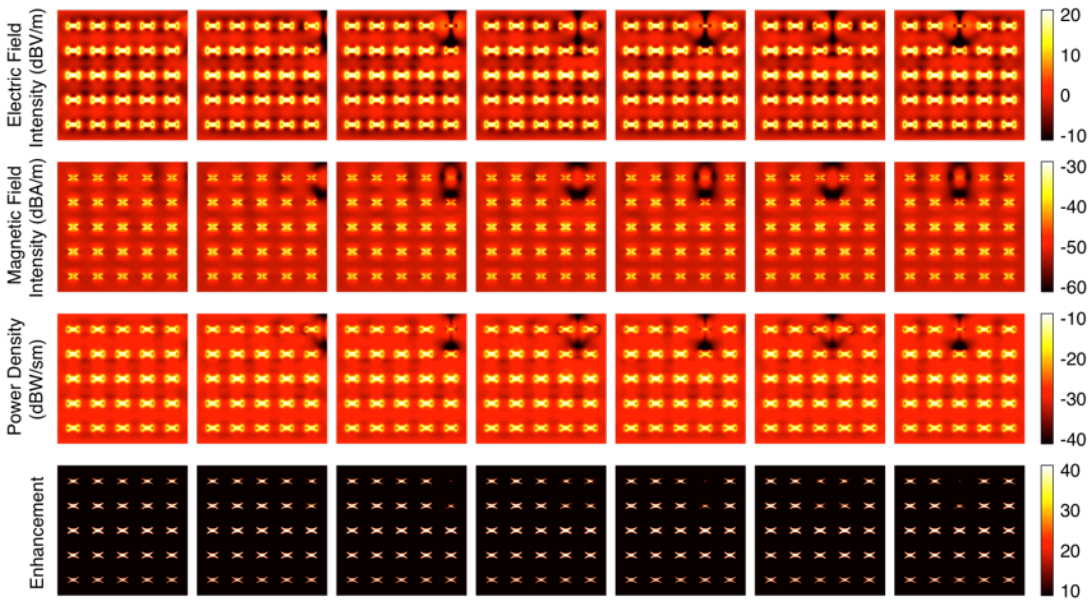

Figure 4.6: Near-zone characteristics of an array of 5×5 nanoantennas when an Ag particle of diameter 600 nm moves above the array as described in Figure 4.5 (right). The periodicity of the array is 475 nm. The bottom of the particle is 10 nm away from the top surfaces of the nanoantennas.

4.1.4 Detection of Dielectric Particles

The results so far involve metallic particles, specifically made of Ag, which are generally easier to detect. As the next set of results, dielectric particles with various permittivity values are considered. Figure 4.7 presents intensity, density, and enhancement distributions in the array plane when spherical dielectric particles of diameter 300 nm are located above a 3×3 array of nanoantennas. The distance between the spheres and nanoantenna surfaces is set to 90 nm. The relative permittivity (ϵ_r) is changed from 2 to 20. It is observed that the sphere with 2 relative permittivity has little effect on the near-zone distributions, while the detection becomes easier as the relative permittivity increases towards 9. Interestingly, the effect of the particle is not significant for some higher contrasts, particularly when $\epsilon_r = \{11, 12, 13\}$ and $\epsilon_r = \{17, 18, 19\}$. Hence, higher permittivity/contrast values do not necessarily indicate easier detection. Figure 4.8 presents another set of results, where particles with different sizes and permittivity values of 4, 6, and 8 are considered. Specifically, in these results, the diameter changes from 100 nm to 300 nm, while the distance between the spherical

particles and nanoantenna surfaces is selected as 20 nm. The results show that the detection is easier when the particle size is 200 nm or larger for all three permittivity values.

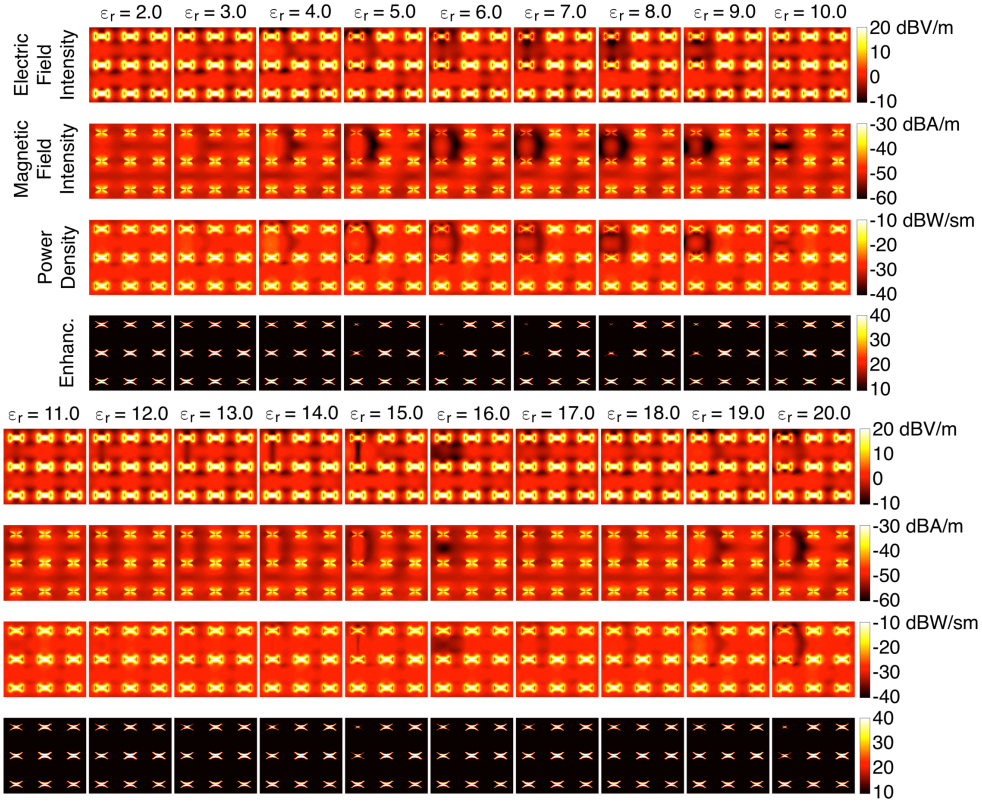

Figure 4.7: Near-zone characteristics of an array of 3×3 nanoantennas when dielectric particles of diameter 300 nm are located above the array. The periodicity of the array is 475 nm. The particles are 90 nm away from the top surfaces of the nanoantennas.

As shown in Figure 4.7, some dielectric particles, even with relatively high contrasts, may not be easily detected by considering field and density distributions in the array plane. While this is related to particle size and contrast, as well as particle-to-array distance, numerical investigations show that the relationship is not trivial. On the other hand, one may consider other planes, particularly the plane of incidence, to increase the reliability of detection. As an example, Figure 4.9 presents field, density, and point-wise enhancement distributions for spherical particles of diameter 300

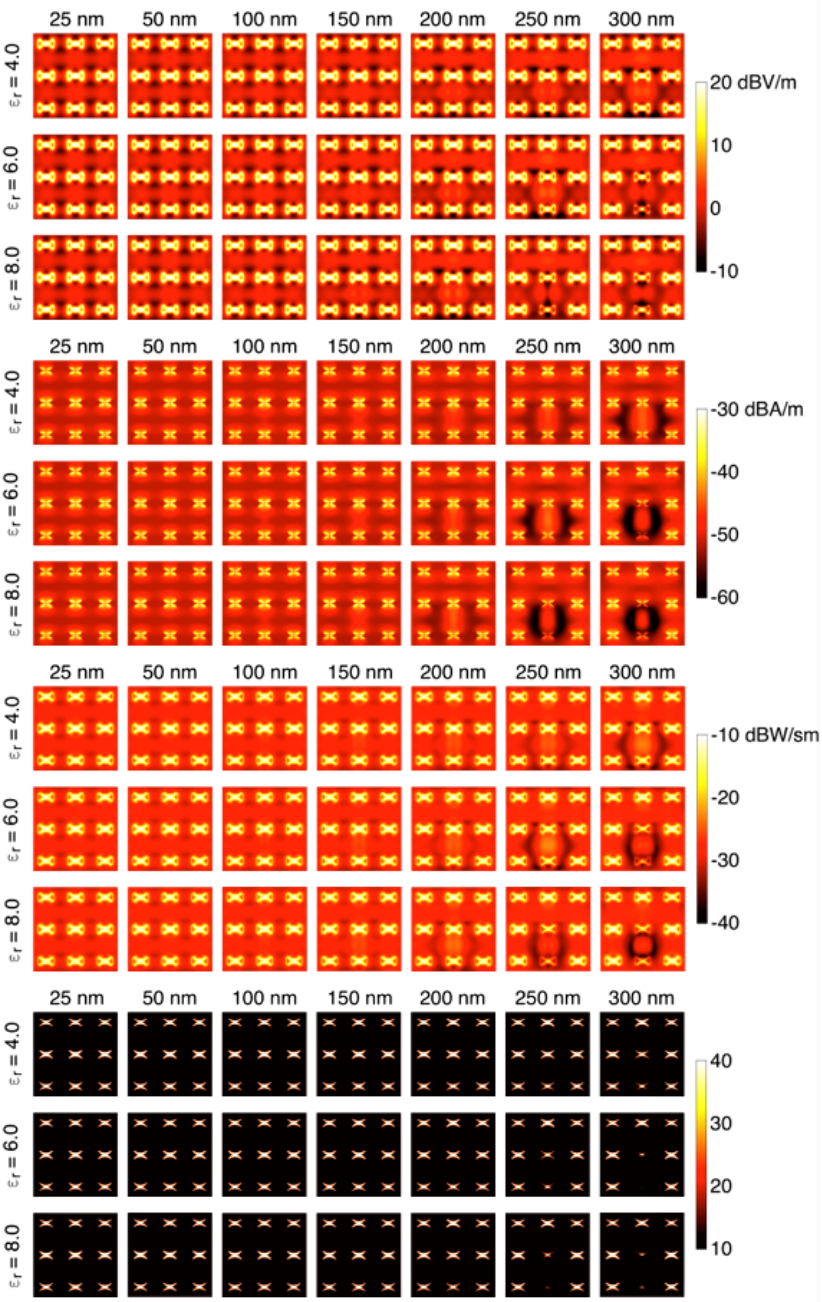

Figure 4.8: Near-zone characteristics of an array of 3×3 nanoantennas when dielectric particles with different sizes (25-300 nm diameter) and permittivity values of 4,6, and 8 are located above the array between middle and bottom rows. The distance between the particles and surfaces of nanoantennas is 20 nm.

nm with relative permittivity values of 3, 6, and 10. In the plane of array, which is now called Plane 1, the particle with $\epsilon_r = 6$ is easily detected, while the others have limited effects on the near-zone characteristics. In the plane of incidence (Plane 2),

however, the particles lead to unique distributions (except for the enhancement plots) such that all of them become detectable. Note that distributions outside the particles should be considered for detection purposes since sampling inside particles may not be possible depending on the application.

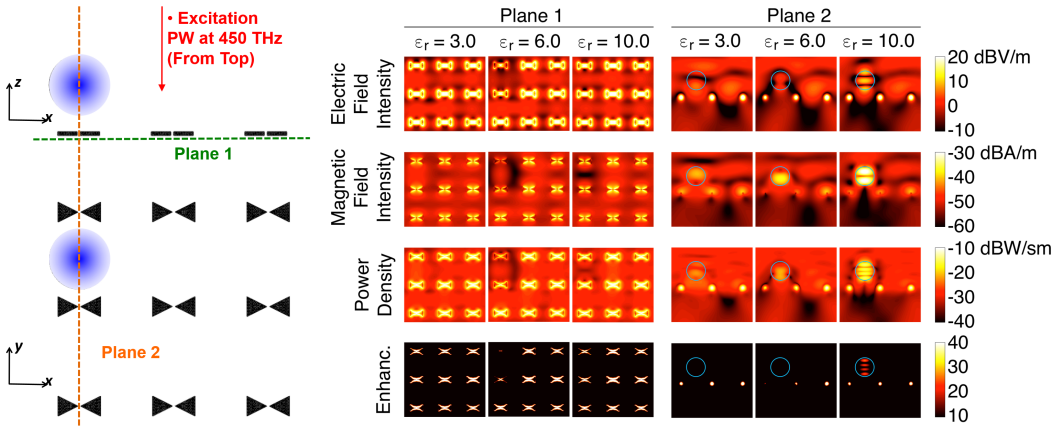

Figure 4.9: Near-zone characteristics of an array of 3×3 nanoantennas when dielectric particles (with $\epsilon_r = 3, 6, 10$) of diameter 300 nm are located above the array. The periodicity of the array is 475 nm. The particles are 90 nm away from the top surfaces of the nanoantennas.

In many applications, not only the existence but also the shape of nanoparticles is critical to be identified. This can be possible if the obtained near-zone distributions are compared with reference results in a database. Different-shaped particles, each of which can be fitted into a box with a volume of $300 \times 300 \times 300$ nm, are positioned on the top of the nanoantenna array as depicted in Figure 4.10. In order to demonstrate the feasibility of geometric identification, Figure 4.11 shows near-zone distributions when dielectric particles with different shapes exist above the nanoantenna array. The relative permittivity of the particles is set to 8. In each case, the distance between the particle and the array surface is 50 nm. The results in Figure 4.11 show that, despite similarities, particles lead to different field, density, and/or enhancement distributions. This means that geometric identification can be possible even with arrays involving small numbers of nanoantennas.

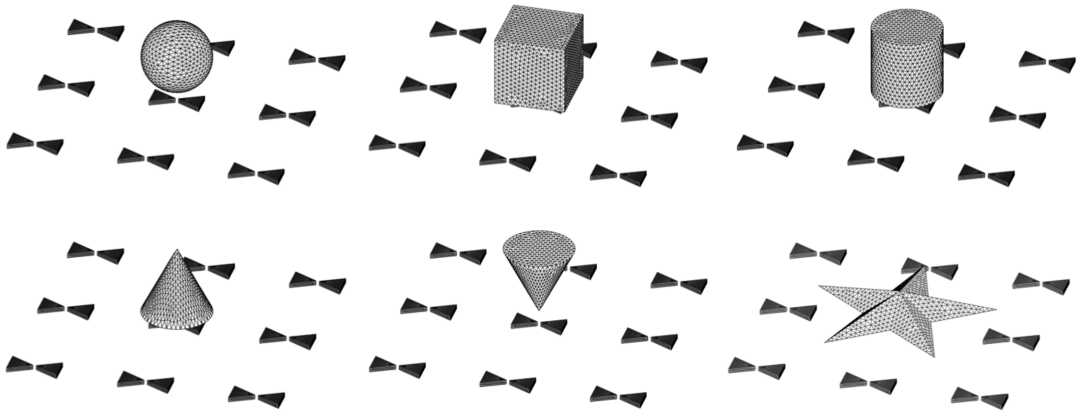

Figure 4.10: An array of 3×3 nanoantennas when dielectric particles with sphere, cube, cylinder, cone 1, cone 2, and star shapes are located above the array.

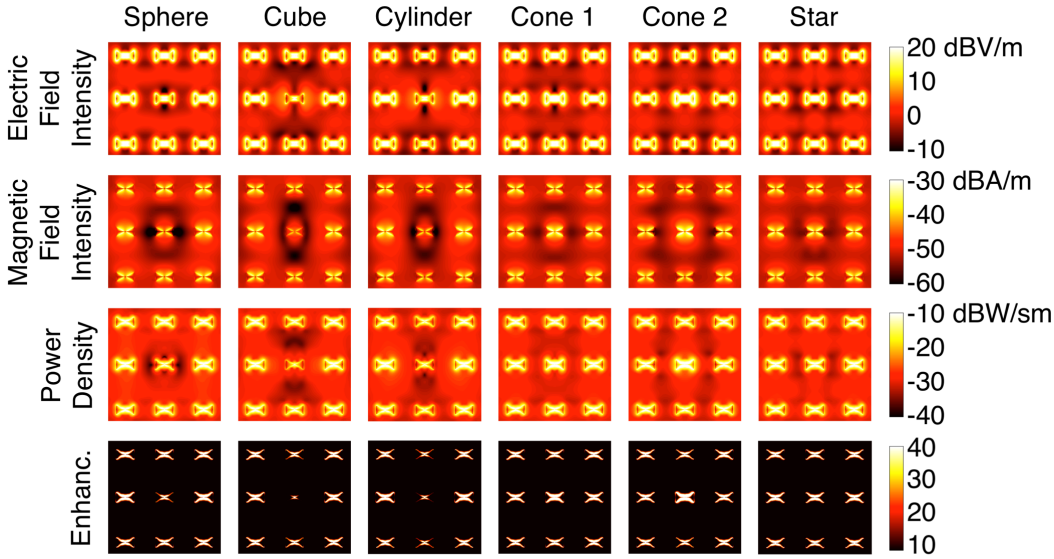

Figure 4.11: Near-zone characteristics of an array of 3×3 nanoantennas when dielectric particles with different shapes are located above the array. The periodicity of the array is 475 nm. The particles are 50 nm away from the top surfaces of the nanoantennas, while their relative permittivity is 8.

4.1.5 Improved Identification of Dielectric Particles by Background Substraction

As shown in the previous discussions, particles introduce perturbations in field and density distributions, while their effects are visible mainly as shadowing in the en-

hancement factor distributions. Nevertheless, even for relatively large particles, it can be difficult to detect and identify them via field, density, and enhancement characteristics. Therefore, we further compute a difference factor as $DF(\boldsymbol{r}) = 100 \times |e_{array}(\boldsymbol{r}) - e_{array+particle}(\boldsymbol{r})|/e_{array}(\boldsymbol{r})$ as a function of position $\boldsymbol{r}$, where $e_{array}(\boldsymbol{r})$ represents enhancement factor values obtained without particles (when the array is excited alone) and $e_{array+particle}(\boldsymbol{r})$ represents the corresponding values when particles exist. These post-processing calculations are applied for situations similar to previous examples and their results are reported in this section.

Firstly, an arrangement of 3×3 Ag bowtie nanoantennas, which can be a part

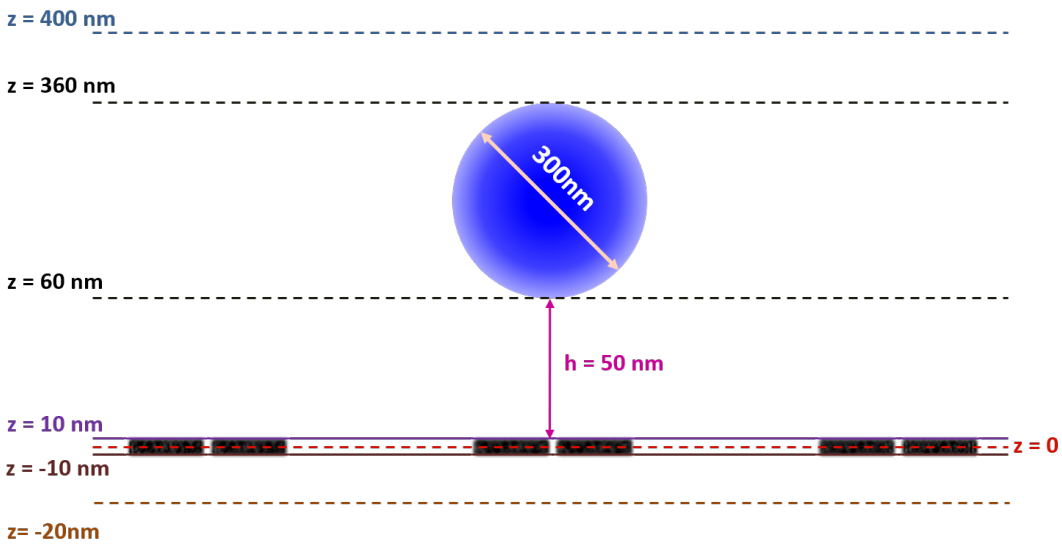

Figure 4.12: Dielectric particle located above an array of 3×3 nanoantennas and the sampling planes located at $z = -20$ nm and $z = 400$ nm.

of a larger array is considered. In the following results, the frequency is fixed to 450 THz. The center-to-center distance is set to 475 nm, which is larger than $\lambda/2$, where λ is the wavelength. As also illustrated in Figure 4.10, dielectric particles with different shapes i.e., sphere, cube, cylinder, as well as cones with two different orientations are considered, which are symmetrically located above the array. All particles fit into $300 \times 300 \times 300$ nm^3 volumes, while they are 50 nm away from nanoantenna surfaces. In the results presented below, the relative permittivity of the particles is selected as 8, while they are assumed to be non-magnetic. The overall structures (array and par-

ticles) are illuminated by a 1 V/m linearly polarized plane wave from the top. In addition, sampling planes at $z = -20$ nm and $z = 400$ nm, which are also depicted in Figure 4.12, are selected in order to achieve more practical visualizations. Figures 4.13 and 4.14 present the electric field intensity ($[-10, 20]$ dBV/m), the magnetic field intensity ($[-60, -30]$ dBA/m), the power density ($[-40, -10]$ dBW/sm), as well as the power enhancement (unitless) and the difference factor (unitless) at two different planes. It can be observed in the fifth column of Figure 4.13 that particles lead to diverse difference factors, making them distinguishable from each other. The results are more remarkable in Figure 4.14, where the sample plane is at 400 nm such that field, density, and enhancement plots are quite uniform, while the position-dependent difference factor makes it possible to identify the shape of the particles. Also, depending on the application, sampling far away above the array (e.g., at 400 nm) may

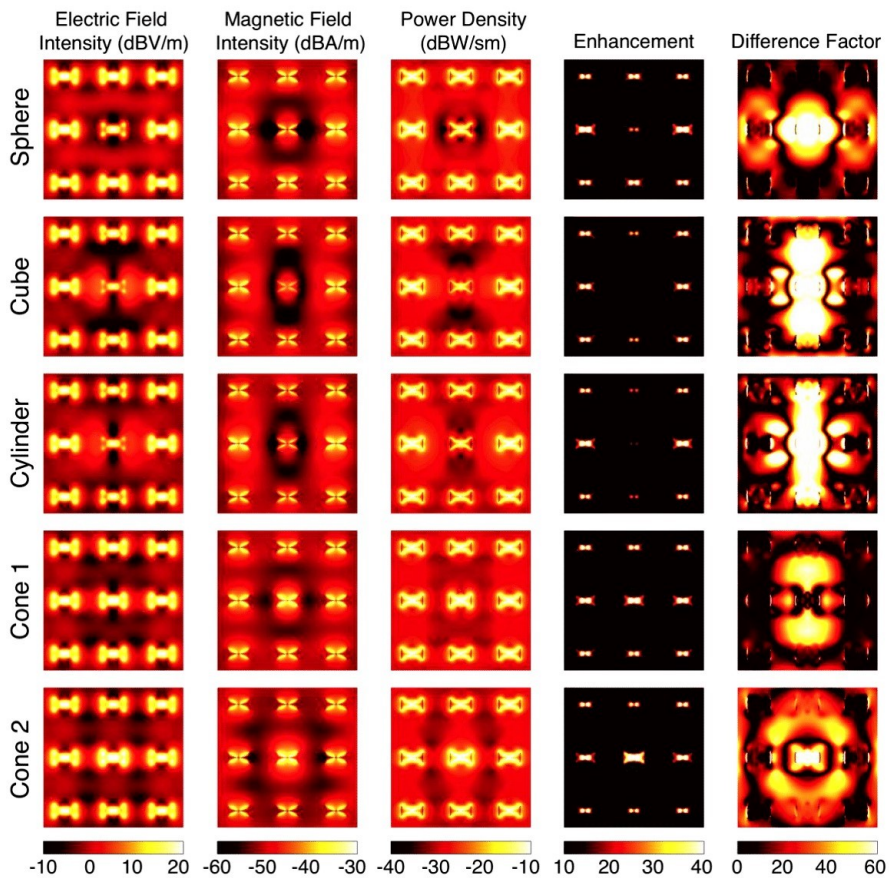

Figure 4.13: Intensity, density, enhancement, and difference factor distributions on the $z = -20$ nm plane for the scenarios depicted in Figure 4.10.

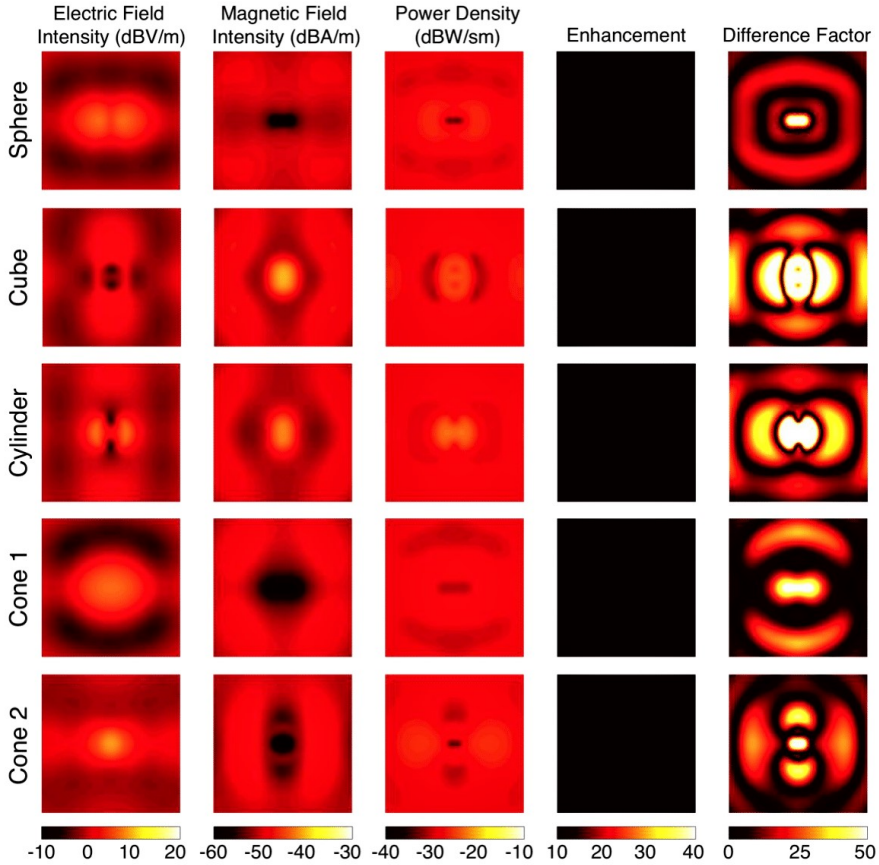

Figure 4.14: Intensity, density, enhancement, and difference factor distributions on the $z = 400$ nm plane for the scenarios depicted in Figure 4.10.

be more practical and feasible than sampling close to the array (e.g., at -20nm).

Now, we consider further scenarios involving the detection of different particles via the background subtraction (post-processing) described above. In these scenarios, the setup shown in Figure 4.12 is considered in all simulations in order to observe the effects of the particles more clearly. Figure 4.15 depicts the difference factor distributions on the $z = 400$ nm and $z = -20$ nm planes when spherical dielectric particles with relative permittivity values from 2 to 8 are located above a 3×3 nanoantenna array. Considering the large difference factor scale (0-50%), even the particles with relatively small permittivity values exhibit distributions that can easily be observed in both planes. Specifically, the post-processing method provides better observation opportunities than direct approach shown in Figure 4.7 wwith remarkably strong and

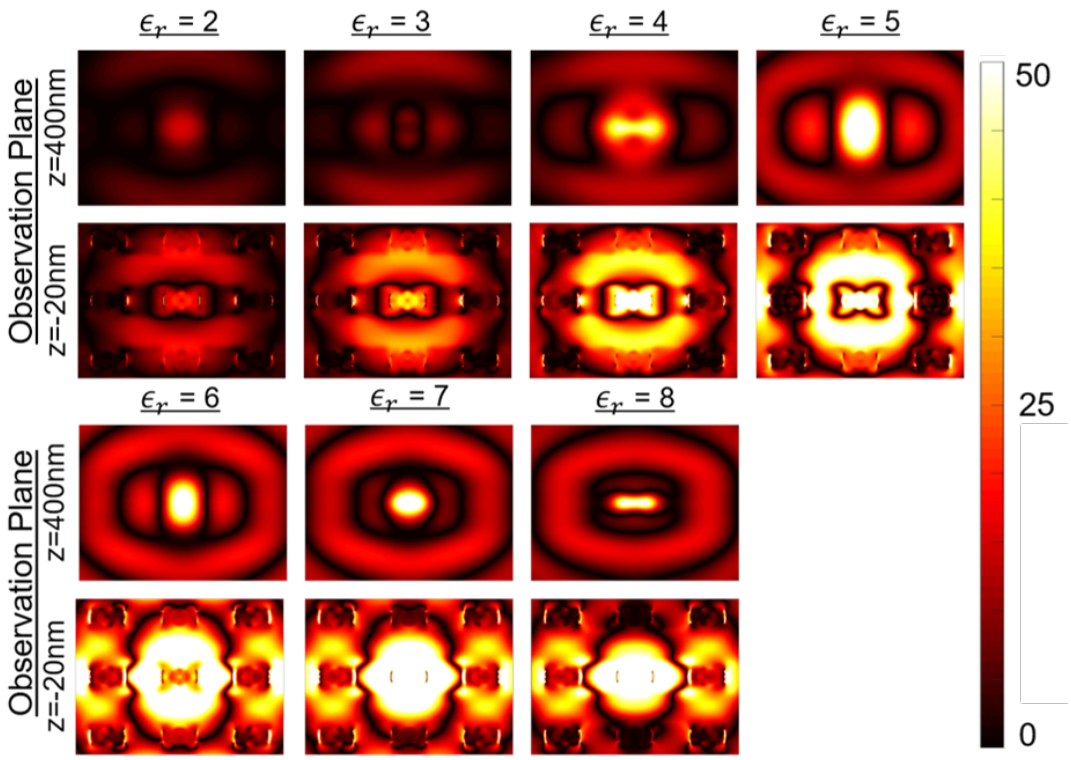

Figure 4.15: Difference factor distributions (on the $z = 400$ nm and $z = -20$ planes) for sphere particles with different relative permittivities above an 3×3 nanoantenna array (such as depicted in Figure 4.12).

distinguishable patterns in both observation planes. In Figure 4.16, particle size is investigated by locating spherical particles with 8 relative permittivity values 50 nm away from the top surface of the nanoantennas. In this figure, two different scales (0-10% and 0-50%) are used for the difference factor to make the distributions for small particles more visible. We observe that, even for tiny nanoparticles, the difference factor provides an opportunity for detection and identification, whereas it becomes increasingly easier to categorize particles as they become larger. Finally, the position of a spherical particle with a diameter of 300 nm is studied, , when its relative permittivity is fixed to 8. Both positions difference factor distributions in the two planes are shown in Figure 4.17. It is observed that the position of the particle can easily be detected, thanks to the difference factor distributions in both planes.

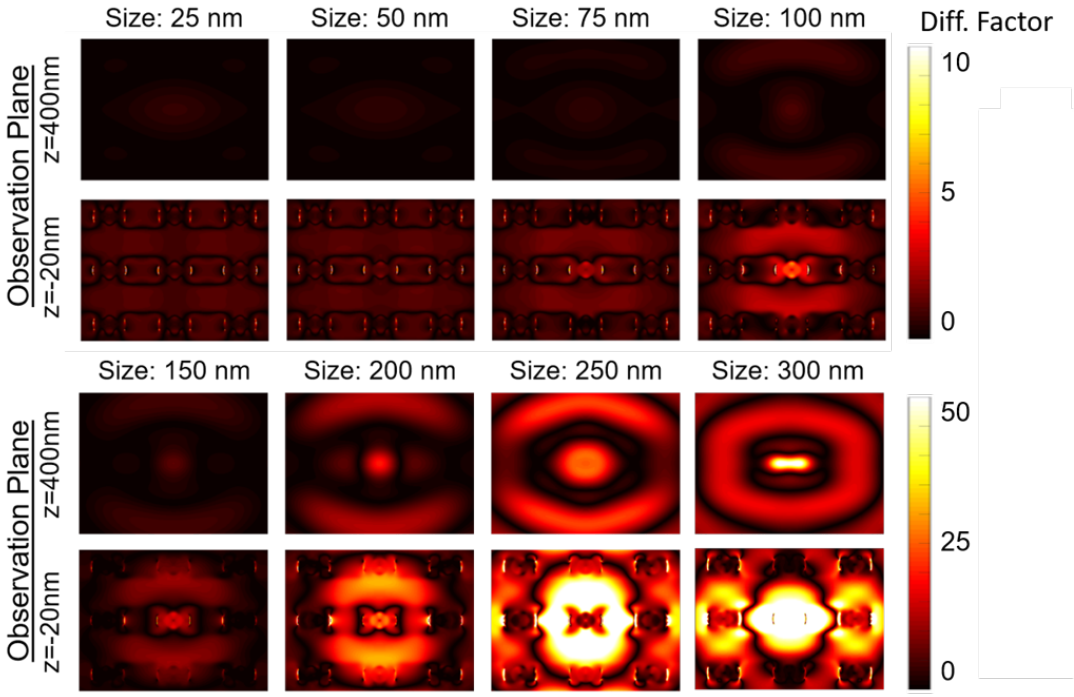

Figure 4.16: Difference factor distributions (on the $z = 400$ nm and $z = -20$ planes) for sphere particles with different sizes above an 3×3 nanoantenna array (such as depicted in Figure 4.12).

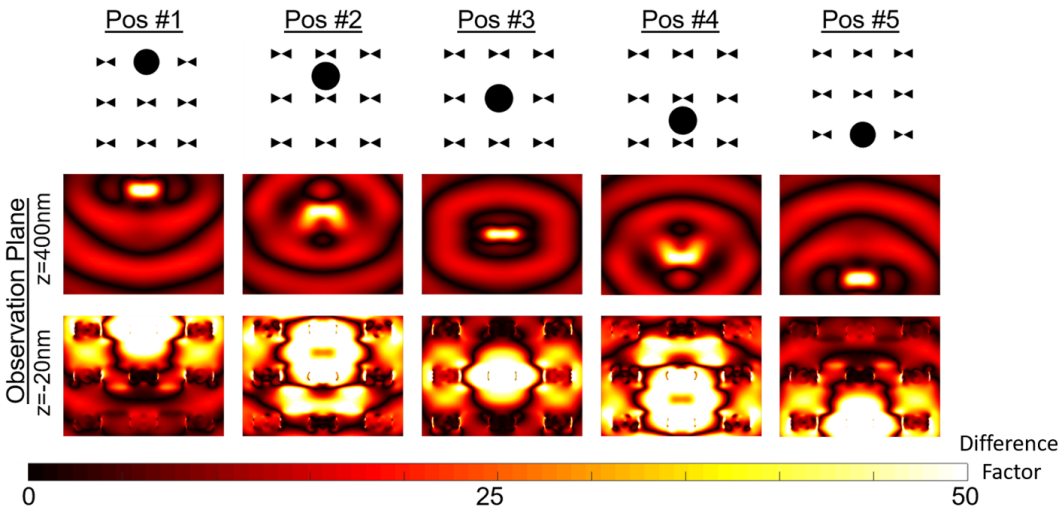

Figure 4.17: Difference factor distributions (on the $z = 400$ nm and $z = -20$ planes) for sphere particles with different positions above an 3×3 nanoantenna array (such as depicted in Figure 4.12).

4.2 Improved Nano-optical Traps for Single-Particle Sensing Applications

In this part, numerical design and simulations of nano-optical traps for single-particle sensing applications are presented. While commonly used nano-holes with circular shapes are suitable for physically trapping nanoparticles to be detected and identified, they generate relatively weak signals in the far zone, especially when nanoparticles are small. It is shown that optical sensitivity of nano-holes can be enhanced significantly by using well-designed bowtie-shaped nanoantenna geometries such that metallic and dielectric nanoparticles can be detected and identified based on far-zone scattering data. Numerical simulations are performed to test the designed nano-holes and demonstrate their excellent performances in various scenarios.

4.2.1 Simulations of Nano-Holes

Due to their relatively large electrical sizes similar to nanoantenna arrays, all simulations and optimization processes are performed by using the efficient and accurate implementation of MLFMA in the frequency domain. As usual, problems are formulated via SIEs, particularly with MCTF, while nano-hole structures and formulations are discretized with the RWG functions defined on triangular domains. Frequency-dependent complex permittivity values of metals are extracted from the Lorentz-Drude model. All electromagnetic interactions are computed with maximum 1% relative error, while the target residual error for satisfactory iterative convergence is set to 0.0001 in all simulations.

4.2.2 Improved Nano-hole Designs

In the numerical examples presented below, nano-holes that are made of Ag are particularly focused, while they are considered to be located in vacuum. After presenting examples of improved designs, nanoparticle detection scenarios based on far-zone scattering characteristics are considered.

Figure 4.18 presents six different nano-hole designs, each involving two sharp tips

close to each other. Considering slabs with single nano-holes, dimensions are 314×300 nm (Design 1), 314×200 nm (Design 2), 330×280 nm (Design 3), 330×330 nm (Design 4), 330×430 nm (Design 5), and 314×336 nm (Design 6), while each has a thickness of 20 nm. These units cells are simply arranged periodically in array configurations. The geometries are designed such that they are highly sensitive to nanoparticles approaching the tip regions. First, in order to demonstrate the basic responses of these nano-holes, their near-zone characteristics, i.e., power enhancement values at their centers (gaps between tips) when they are excited by plane waves from 250 THz to 600 THz are investigated. Figure 4.19 depicts the power enhancement factor, which is calculated by evaluating the ratio of the power density at the tip locations to the incident power. It can be observed that very high enhancement values can be obtained at some frequencies, e.g, reaching 50 at around 300 THz, making these nano-holes suitable even for energy harvesting. Although enhancement values are always larger than unity in the entire frequency range, there are also frequencies (e.g., 450 THz for all nano-holes other than Design 5), at which enhancement is not strong. At these frequencies, the nano-holes can be considered to be less sensitive to

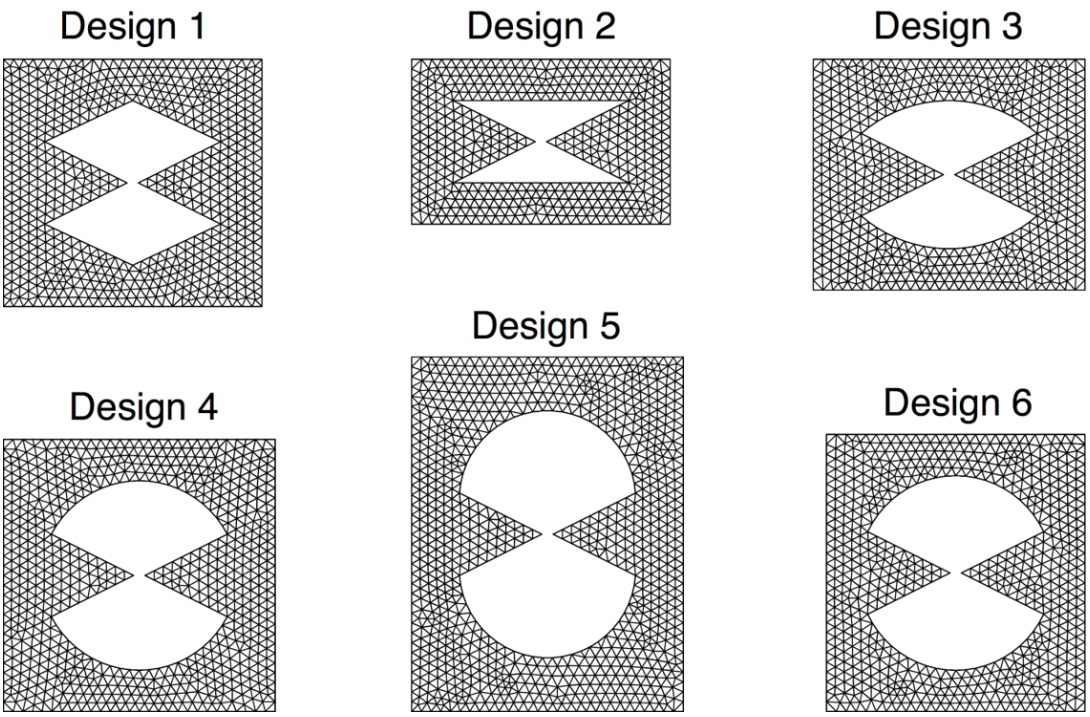

Figure 4.18: Six different improved nano-hole designs that are sensitive to nanoparticles.

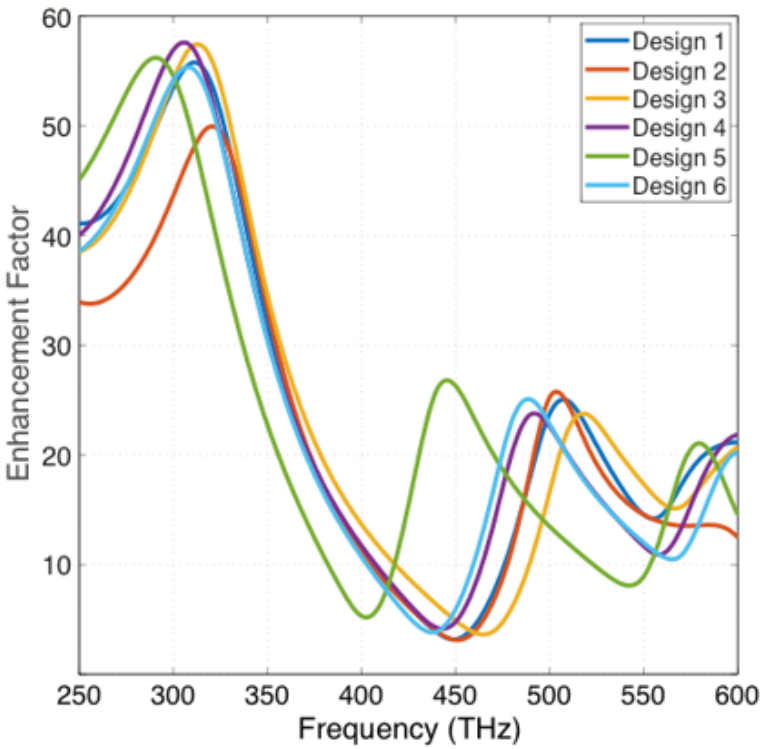

Figure 4.19: Frequency-dependent power enhancement factors for the six different nano-hole designs in Figure 4.18.

their environment, including nearby nanoparticles.

In single-particle detection and sensing applications, it is often desirable to detect and sense particles based on far-zone scattering characteristics. In fact, relatively high sensitivity of the nano-hole designs described above facilitates this task by providing quite different scattering responses in the absence and existence of nanoparticles. As a set of examples, we consider cylindrical Ag nanoparticles at the gap locations of Design 1, Design 3, and Design 4, as depicted in Figure 4.20. The height and the diameter of the cylinders are 60 nm and 8 nm, respectively, while they are located symmetrically between the tips. The nano-holes with and without nanoparticles are excited by 1 V/m plane waves with normal incidence from 250 THz to 600 THz. Figure 4.21 presents the far-zone electric field intensity (i.e., electric field intensity multiplied with the distance, as the distance goes to infinity) in the backscattering direction, as well as in a side-scattering direction (30° off-axis in the E-plane). As expected, electric field values tend to be stronger in the backscattering direction, while

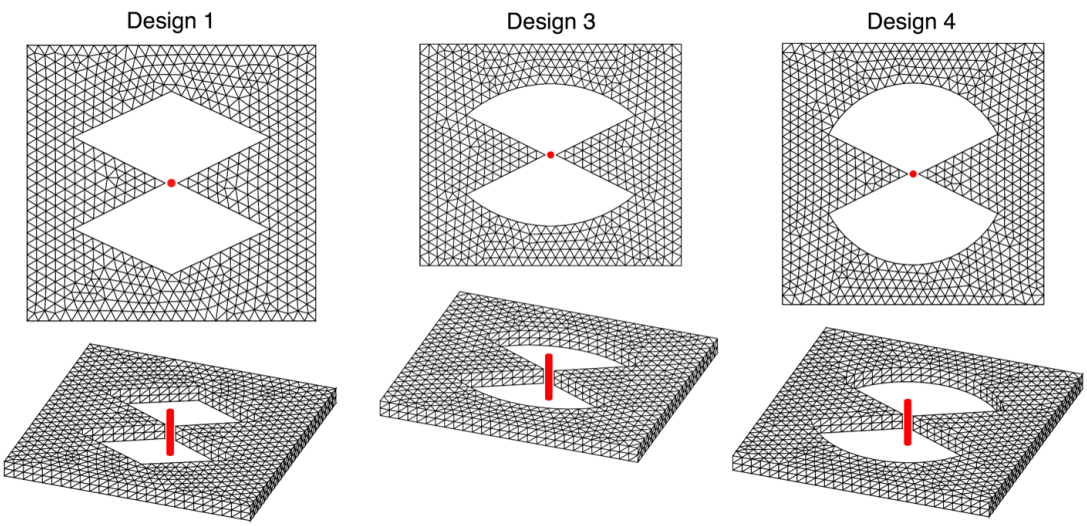

Figure 4.20: Cylindrical nanoparticles located at the gap locations of Design 1, Design 3, and Design 4.

side-scattering values are also significant in terms of detection. In general, the effect of nanoparticles is clearly visible as perturbed electric field values, particularly at frequencies lower than 350 THz and higher than 500 THz. As shown below, perturbation values, rather than the direct absolute values, can provide significant information on the existence of a nanoparticle, as well as its characteristics (e.g., size, geometry, and material properties).

Even when using well-designed and highly sensitive nano-holes, nanoparticle detection can be challenging, especially when considering far-zone scattering values. In order to facilitate detection, as well as identification, one can perform a subtraction operation on the received signals obtained with and without nanoparticles. This can be seen as a calibration with background signal (similar to background subtraction performed for detections with nanoantenna arrays), i.e., the electromagnetic response of the used nano-hole when the environment is clean. As an example, Figure 4.22 presents the far-zone electric field intensity values for Design 3, i.e., intensity values with/without the cylindrical Ag nanoparticle and absolute differences between them. For comparisons, a circular nano-hole (radius: 90 nm) with the same setup is also considered. The difference values obtained with Design 3 are significantly larger than those obtained with the circular nano-hole. In fact, for the circular nano-hole

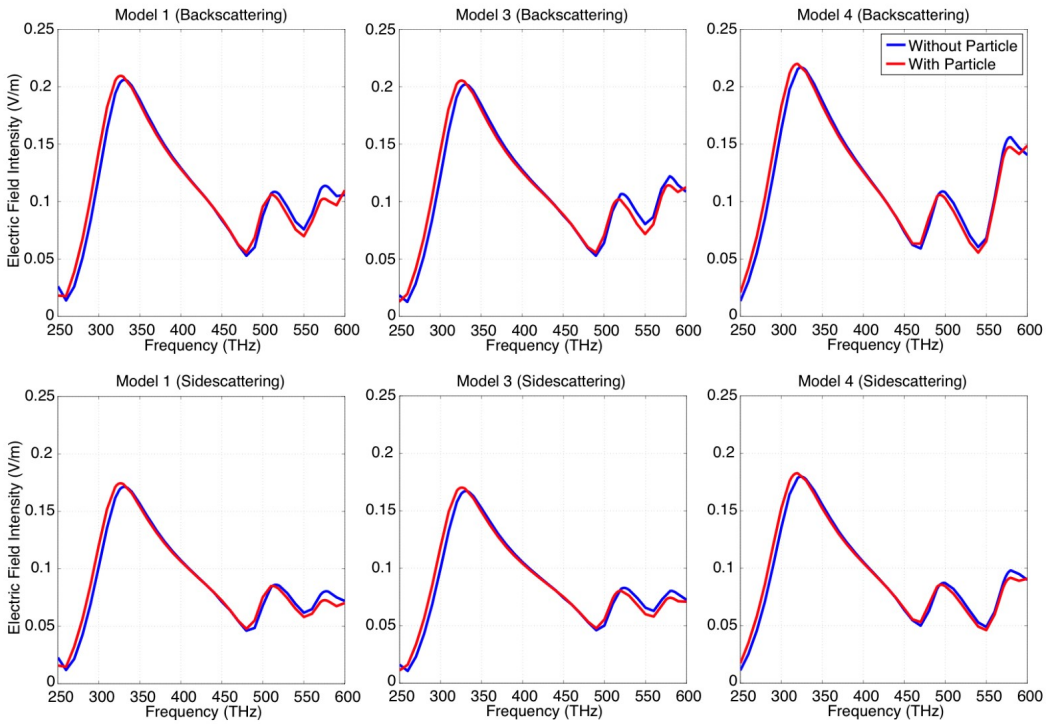

Figure 4.21: Far-zone electric field intensity with respect to frequency scattered from Design 1, Design 3, and Design 4, with and without cylindrical Ag nanoparticles. In addition to backscattered intensity values (first row), results for 30° off-axis side-scattering (second row) are considered.

case, existence of the nanoparticle creates almost no difference in the scattering characteristics.

In Figure 4.22, the performance of the designed nano-holes is shown, specifically considering Design 3, for Ag nanoparticles. Now, more challenging cases involving dielectric nanoparticles that possess weaker electromagnetic responses and interactions with their environments are considered. Figure 4.23 presents the results for Design 3 and cylindrical dielectric nanoparticles, again in comparison to the circular nano-hole. The height and the diameter of the cylinders are again 60 nm and 8 nm, respectively, while three different refractive index values as $n = 1.6$, $n = 1.7$, and $n = 1.8$ are considered. The electromagnetic scattering response of the isolated cylindrical particle with refractive index $n = 1.7$ is also given in Figure 4.23 with the intensity differences obtained by the nanotrap and nano-hole designs. In com-

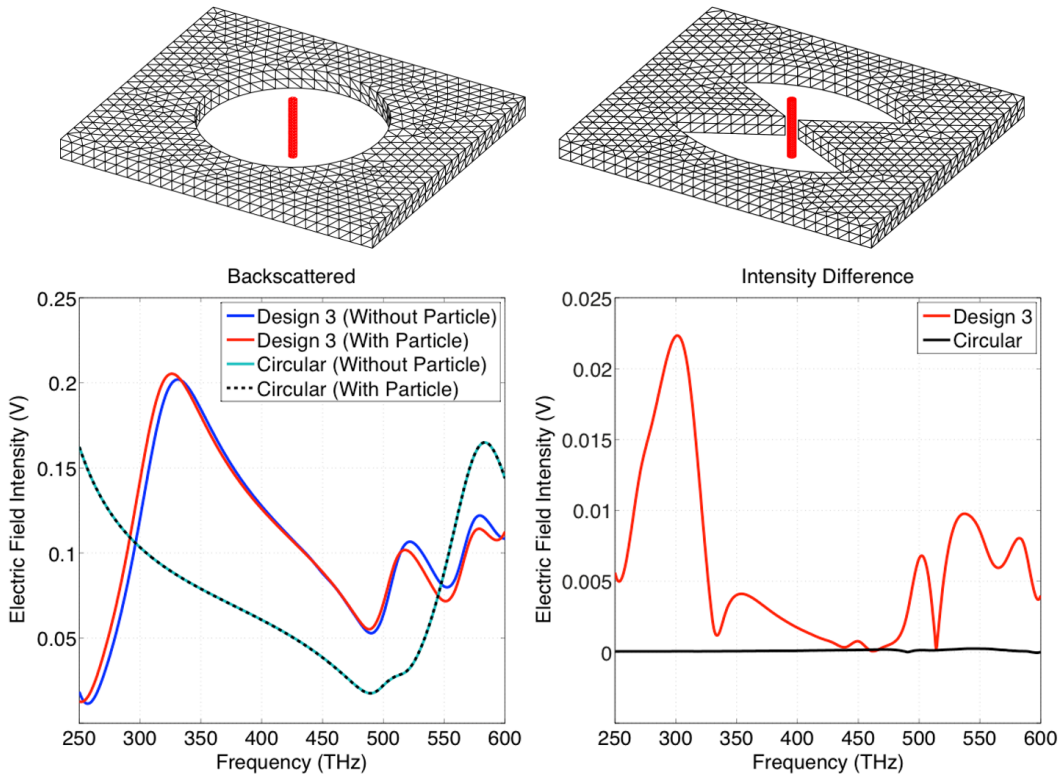

Figure 4.22: Electric field intensity values with and without cylindrical Ag nanoparticles for Design 3 and for a circular nano-hole. For each nano-hole, in addition to backscattering values (left), difference values (right) that are obtained by taking the difference of backscattering values obtained with and without the nanoparticle are shown.

parison to the Ag nanoparticle, dielectric nanoparticles are more difficult to detect, i.e., electric field intensity values change slightly in the presence of the nanoparticles so that difference values drop down. At the same time, nanoparticles are still much easier to detect when using the improved design instead of the circular nano-hole. Besides, Figure 4.23 shows that even 0.1 difference in the refractive index may be sensed based on intensity difference plots. It must be highlighted that each intensity difference response has a higher amplitude with respect to the backscattering of the isolated nanoparticle, which proves the necessity of these types of sensors. Figure 4.24 presents further results when cylindrical nanoparticles (60 nm height and 8 nm diameter) with different relative permittivity values, i.e., 2, 8, 16, exist at the center of Design 3. Considering difference plots, nanoparticles with different electrical pa-

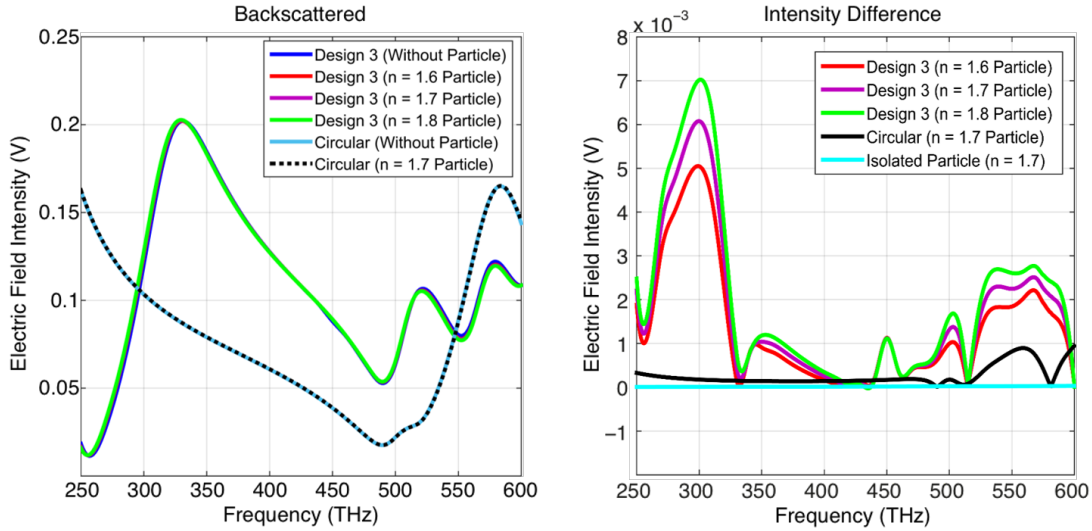

Figure 4.23: Electric field intensity values with and without cylindrical dielectric nanoparticles for Design 3 and a circular nano-hole. For both nano-holes, in addition to backscattering values (left), difference values (right) that are obtained by taking the difference of backscattering values obtained with and without the nanoparticle are shown.

rameters can be identified, provided that a suitable range of frequencies is considered, e.g., if the observation is not restricted to a narrow range at around 450 THz.

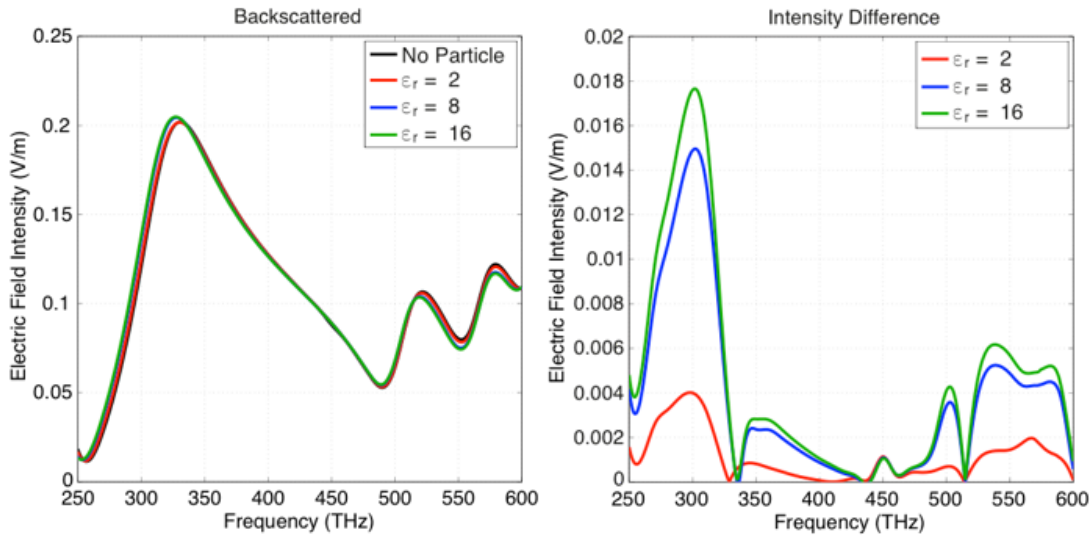

Figure 4.24: Electric field intensity values with and without cylindrical dielectric nanoparticles for Design 3. Three different permittivity values are considered.

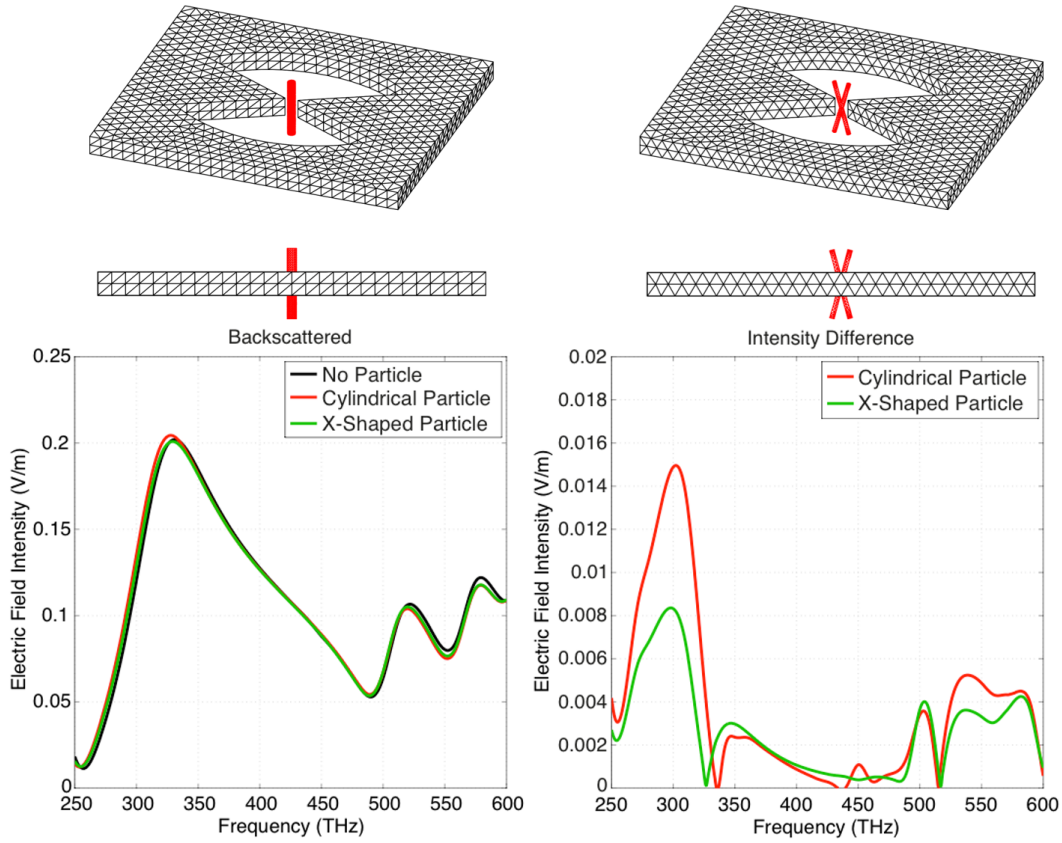

Figure 4.25: Electric field intensity values with and without dielectric nanoparticles for Design 3. Two different geometries are considered, while the relative permittivity is set to 8.

So far, it is shown that difference plots can be used to identify nanoparticles with different electrical characteristics. Now, an example of identification of nanoparticles based on their shapes is considered. Once again, focusing on Design 3, we investigate its response when an X-shaped nanoparticle exists at its center. The permittivity of the nanoparticle is set to 8. In Figure 4.25, the electric field intensity in the backscattering direction is shown with and without the X-shaped nanoparticle, as well as with a cylindrical nanoparticle (60 nm height and 8 nm diameter) that also has a relative permittivity of 8. Considering the difference plots, the X-shaped and cylindrical nanoparticles lead to quite different responses, not only in terms of amplitude but also in terms of shape. Hence, based on the received backscattering signal, it may be possible to identify or at least categorize the nanoparticle that is trapped inside the nano-hole.

In the cases discussed above, it is assumed that the nanoparticles are located at the hole centers for both the improved and circular nano-hole structures. In fact, locating the given nanoparticle at the hot spot of the design is the best scenario for a detection. On the other hand, it may not be always possible to keep a nanoparticle exactly at the center and the detection ability needs to be maintained even when it is located off-center. In order to test this, the locations of the particles for both improved and circular nano-holes are shifted along the y-axis by $+22.5$ nm while keeping their locations constant in the other two axes. In Figure 4.26, the electric field intensity in the backscattering direction is shown with and without the cylindrical (60 nm height and 8 nm diameter) and X-shaped (60 nm height and 4 nm diameter for each arm) nanoparticles, while the refractive index of the nanoparticles is set to 2. Furthermore, the intensity difference plots for the same trials are depicted in Figure 4.27. Considering the difference plots, we observe that the improved design (Design 3) significantly improves the detection ability in comparison to the circular nano-hole, while the deteriorated signal levels due to off-center positioning of the nanoparticles are clearly visible.

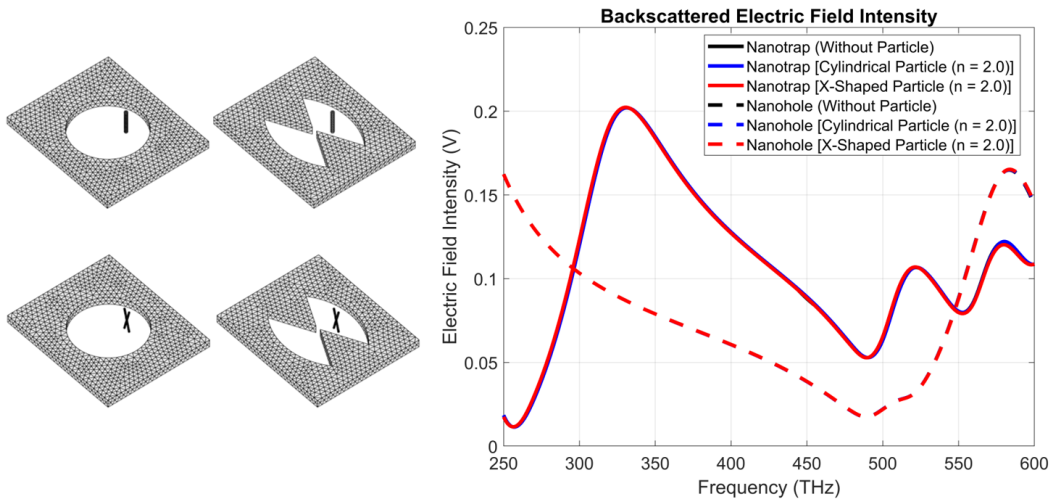

Figure 4.26: Electric field intensity values with and without the off-center-located dielectric nanoparticles for Design 3 (nanotrap) and circular nano-hole. Two different particles are considered, while the refractive index is set to 2.

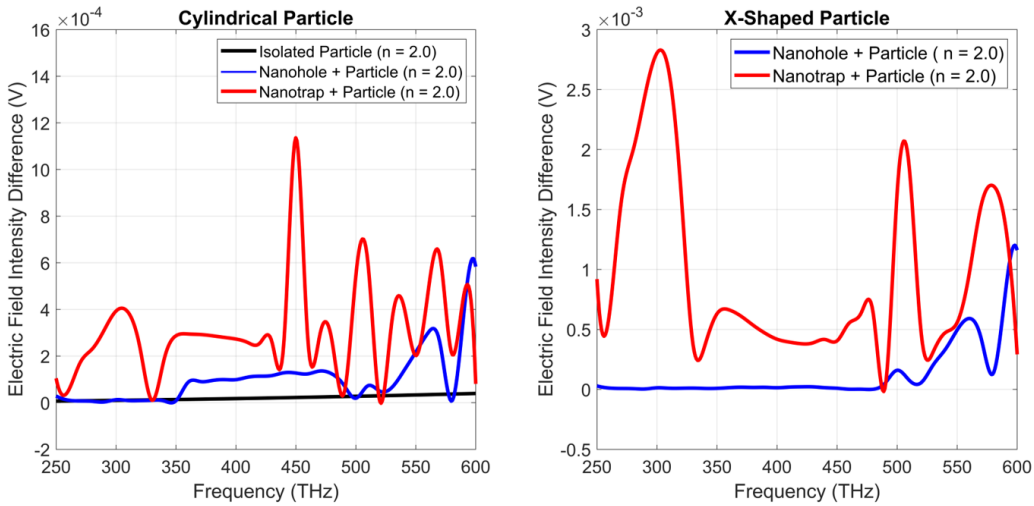

Figure 4.27: Intensity difference values for dielectric nanoparticles that are located off-center inside Design 3 (nanotrap) and circular nano-hole. Two different particles are considered, while the refractive index is set to 2.

In order to better understand the electromagnetic characteristics of the improved nano-hole designs, a near-zone analysis is carried out using different particle shapes. Three different particles that can fit into a cylinder of 60 nm height and 8 nm diameter and the setups for their detection are depicted in Figure 4.28. Similar to the previous examples, Design 3 is selected for the experiments. The refractive index of the particles is set to 1.7.

First, electromagnetic scattering responses of the particles when using the improved design (Design 3) are shown in Figure 4.29. It can be seen that the nanoparticles lead to quite different responses; in fact, the multiband characteristics of the improved nano-hole design enhance the unique responses of the particles. For example, it can be observed in the difference plot that there is a maximum at around 330 THz for Particle 2, while the other particles cause minimal changes in the scattering characteristics of the structure, which may be used to distinguish Particle 2 from others.

Next, near-zone electric field characteristics are investigated by selecting observation points on x-y (at $z = 0$), x-z (at $y = 0$), and y-z (at $x = 0$) planes at 330 THz. In each plane, a 250×250 nm are is sampled at 201×201 points. Near-zone electric

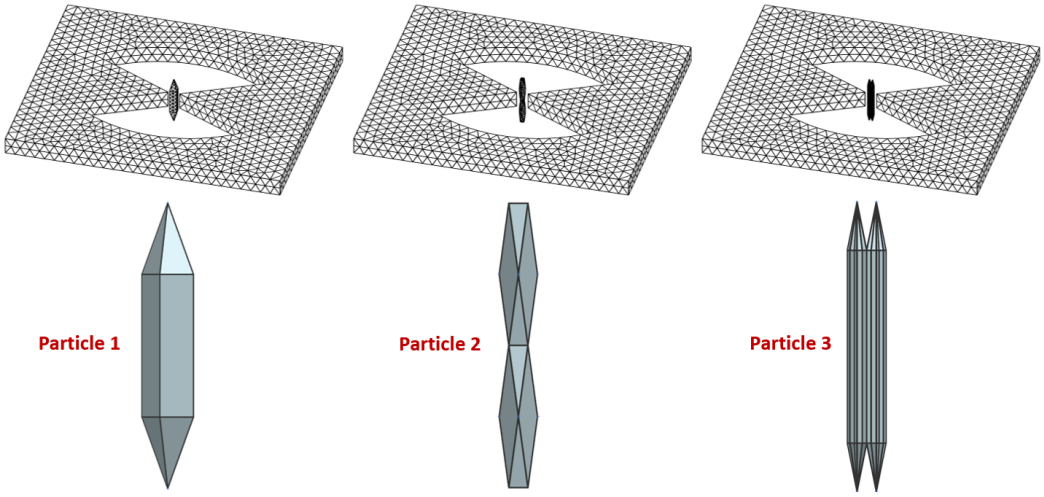

Figure 4.28: Three different particles that can fit into a cylinder of 60 nm height and 8 nm diameter, and the setups to detect them.

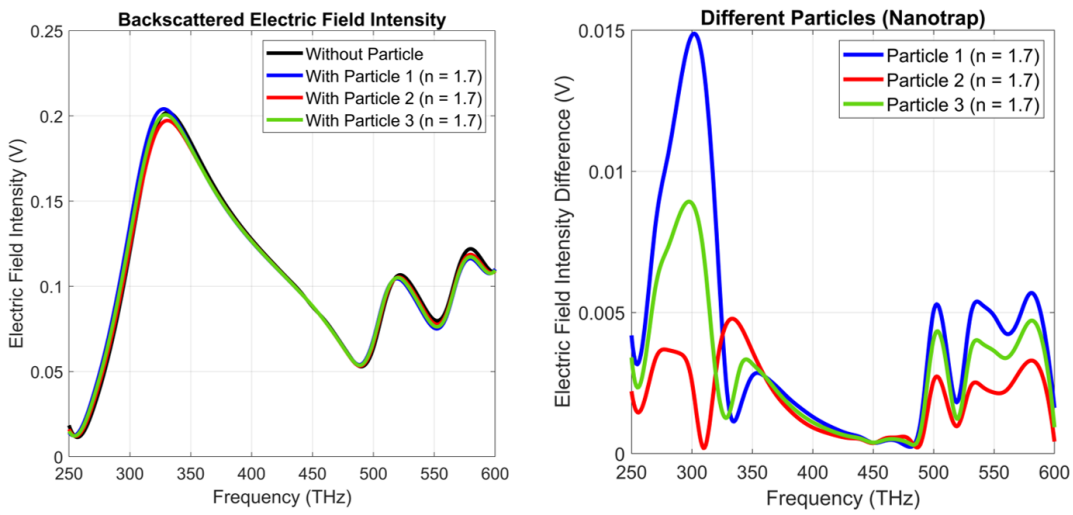

Figure 4.29: Electric field intensity values with and without Particle 1, Particle 2, and Particle 3 for Design 3. For each case, in addition to backscattering values (left), difference values (right) that are obtained by evaluating the difference of backscattering values obtained with and without the nanoparticles are shown.

field characteristics of the improved nano-hole design (Design 3) with and without particles are depicted in Figure 4.30. Even though the effect of the existence of a particle is visible in each plot, it is nearly impossible to identify differently shaped

particles without any post-processing. Hence, the background subtraction method is applied by evaluating the differences in near-zone electric field values obtained with and without the nanoparticles, leading to the plots given in Figure 4.31. When different planes in these images are considered together, the effect of differently shaped nanoparticles on the hot spot pattern becomes evident.Specifically, by applying the background subtraction, we are able the distinguish different nanoparticles based on near-field data, even when these particles have the same electrical parameters and they are remarkably small.

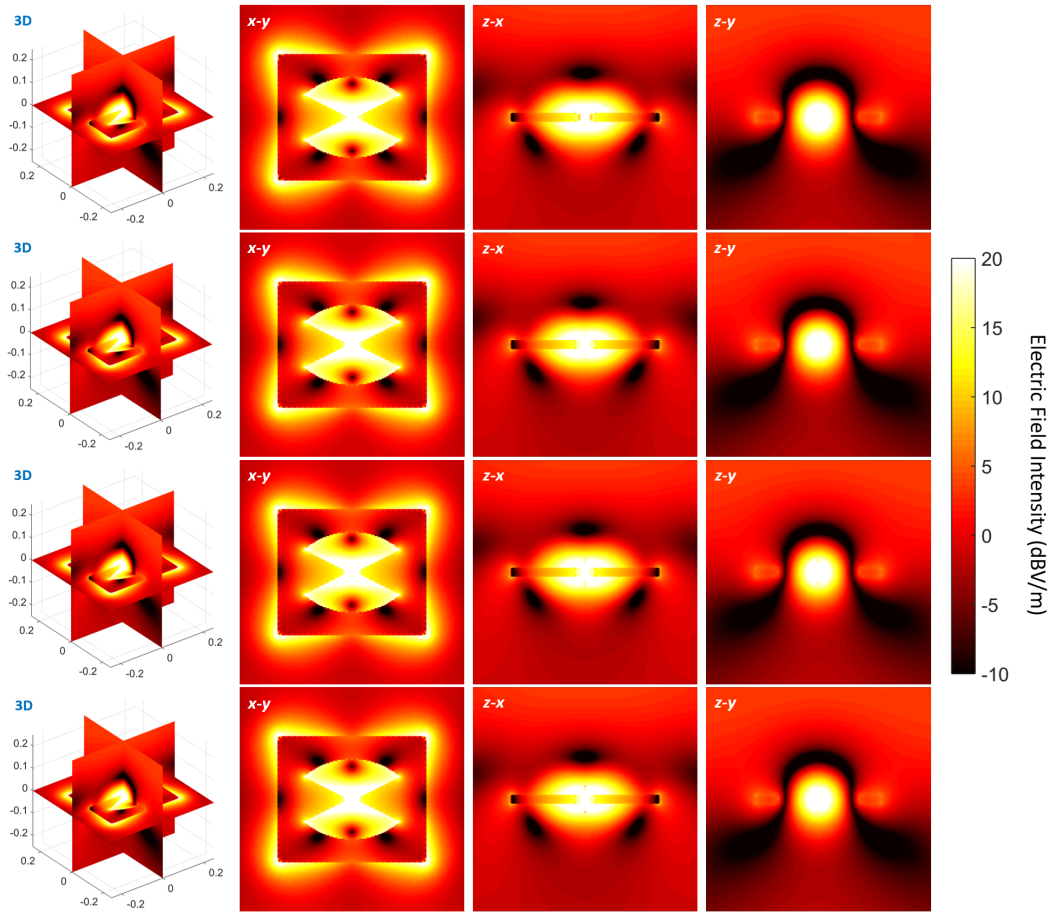

Figure 4.30: Near-zone electric field characteristics of the improved nano-hole structure (Design 3) without particle (top row), Particle 1 (second row), Particle 2 (third row), and Particle 3 (last row). The particles are located at the center.

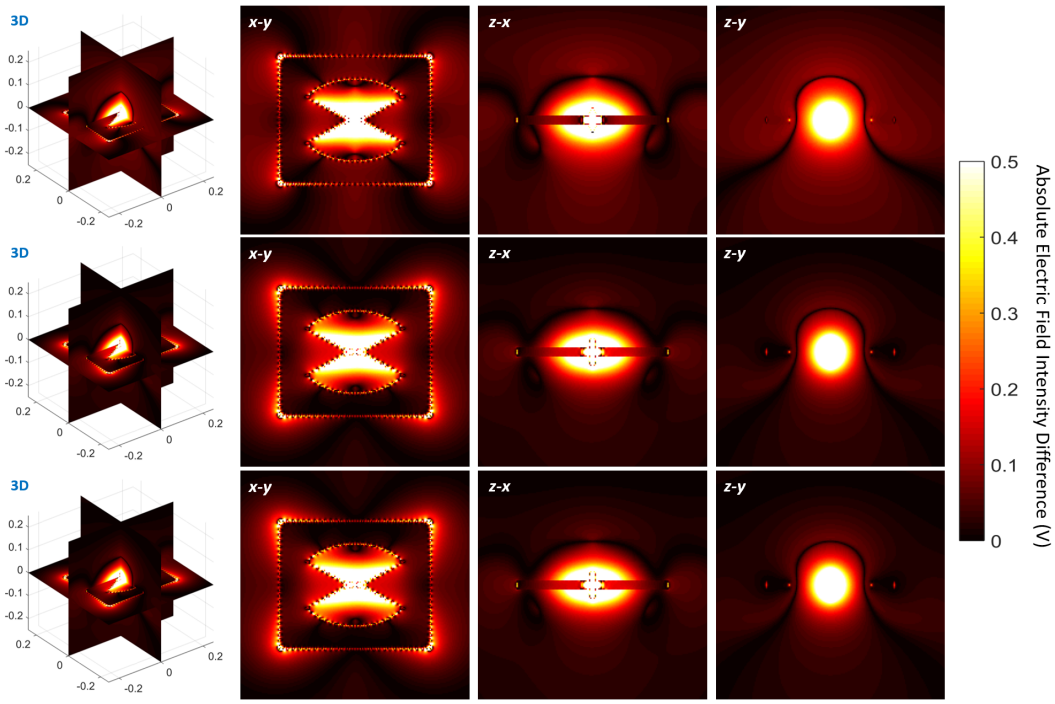

Figure 4.31: Near-zone electric field intensity difference characteristics of the improved nano-hole structure (Design 3) with Particle 1 (top row), Particle 2 (second row), and Particle 3 (last row). The particles are located at the center.

4.3 Concluding Remarks

In the first section of this chapter, design and computational analyses of nanoantenna arrays for particle detection applications are presented. By using a highly accurate simulation environment, alternative nanoantenna arrays and nearby nanoparticles are investigated in diverse scenarios. The results demonstrate the feasibility of sensing and imaging of metallic and dielectric particles, even of subwavelength sizes at optical frequencies. In order to improve the detection of nanoparticles, a background subtraction method is applied, leading to an ability to distinguish particles in addition to detecting their existence. Estimations of particle shape, size, material, and position from difference factor distributions are investigated in detail.

In the second section, effective nano-optical traps for reliable detection and identification of nanoparticles in single-particle sensing applications are discussed. Novel

nano-hole geometries, which are highly sensitive to trapped nanoparticles, are designed and investigated in various scenarios. In comparison to the standard nano-holes with circular shapes, the designed geometries provide satisfactory scattering values, which can be used to detect and even to identify nanoparticles in terms of type, geometry, and electrical parameters.

CHAPTER 5

CONCLUSION

In this study, design, optimization, and computational analyses of plasmonic nanoantennas with strong power-enhancing abilities are presented. Furthermore, utilization of nanoantennas in array arrangements and improved nano-hole structures are discussed in the context of nanoparticle detection and sensing.

A major backbone of this thesis is the rigorous simulation environment that enables accurate and efficient solutions of three-dimensional nanostructures. As the measurement data and harmonic oscillator models indicate, unique electrical properties of metals at optical frequencies must be handled carefully to obtain accurate numerical results. The behavior of metals at optical frequencies necessitates their penetrable models; in this context, various SIE formulations are tested to achieve both reliable and fast solutions. Numerical analyses based on analytical solutions show that the recently developed MCTF is the best option to deal with electromagnetic problems involving plasmonic nanoantennas.

For the purpose of designing single nanoantennas, the impact of different design parameters on the enhancement factor is investigated in detail. The results show that combinations of design parameters, such as shape, material, and size, as well as fabrication factors (like curved edges and tips) and additional substrate layers, can significantly affect the response of a nanoantenna. These factors also help us to engineer nanoantennas for achieving desired responses. For example, we introduce slitted nanoantennas for multiband frequency characteristics, while different options for the slit position, width, and orientation still need to be considered, depending on the application. In addition to slitted structures, a major novelty of this study is shape

optimization of nanoantennas for desired electromagnetic characteristics. We show that high enhancement factor values can be achieved with the help of optimization via GAs. The introduced nanoantenna designs are compared with each other and with examples from the literature in terms of enhancement factor, bandwidth, and multiband characteristics. The results show that the designed nanoantennas in this study exhibit favorable enhancement characteristics, while having higher potential for fabrication in massive amounts with their relatively wide gaps and rough details.

A simple bowtie nanoantenna geometry, which has an excessive electromagnetic field confinement ability, can be used to improve optical sensitivity in particle detection applications. It is shown that an array arrangement of such a bowtie nanoantenna can enable easier detection of single particles based on near-zone responses, while an improved nano-hole structures inspired by nanoantenna geometries can significantly enhance particle detection in comparison to standard nano-holes. Besides sensing the existence of nanoparticles, the possibility of identifying particles is further investigated by examining various detection cases involving different nanoparticle shapes, sizes, and electrical properties. Numerical results show that detection and even identification of nanoparticles with different properties are possible with the proposed background-subtraction method for both nanoantenna arrays and nano-holes.

Although this study can be seen as a robust step in the nanoantenna engineering area, there is still much room for improvement. The first one is obviously the fabrication of the novel nanoantenna designs, which exhibit powerful enhancement characteristics. Even though the fabrication process was one of the goals of this thesis study, usual issues, observed in all experimental researches, caused delays in fabrication of nanoantennas and their extensive tests. Hence, we had to complete this thesis without including any experimental result, while the studies are still ongoing to demonstrate the favorable properties of the designs in practice. The second future work is designing nanoantennas with broader bandwidths, especially to cover the visible spectrum as much as possible. The results presented in this thesis show that this may be possible with the developed optimization mechanism by using suitable cost functions. The resulting designs may provide unprecedented levels of bandwidths and solve frequency-related issues in energy harvesting. Finally, particle sensing applications involving

real-life nanoparticles (e.g., viruses, proteins, bacteria) can be investigated in the context of the presented detection methods. The background subtraction method, as well as improved post-processing techniques based on signal processing, can be useful to further enhance detection and identification of such challenging geometries towards more robust nanostructures for imaging and sensing.

REFERENCES

[1] S. A. Maier, *Plasmonics: Fundamentals and Applications*. Springer, 2007.

[2] J. Alda, J. M. Rico-Garcia, J. M. Lopez-Alonso, and G. Boreman, "Optical antennas for nano-photonic applications," *Nanotechnology*, vol. 16, pp. 230–234, Mar. 2005.

[3] Y. Nishijima, L. Rosa, and S. Juodkazis, "Surface plasmon resonances in periodic and random patterns of gold nano-disks for broadband light harvesting," *Optics Express*, vol. 20, pp. 11466–11477, May 2012.

[4] Y. M. El-Toukhy, M. Hussein, M. F. O. Hameed, A. M. Heikal, M. M. Abdelrazzak, and S. S. A. Obayya, "Optimized tapered dipole nanoantenna as efficient energy harvester," *Optics Express*, vol. 24, pp. 1107–1122, Jul. 2016.

[5] T. Kosako, Y. Kadoya, and H. F. Hofmann, "Directional control of light by a nano-optical yagi-uda antenna," *Nature Photonics*, vol. 4, pp. 312–315, Mar. 2010.

[6] E. G. Mironov, A. Khaleque, L. Liu, I. S.Maksymov, and H. T. Hattori, "Enhancing weak optical signals using a plasmonic yagi-uda nanoantenna array," *IEEE Photonics Technology Letters*, vol. 26, pp. 2236–2239, Nov. 2014.

[7] D. M. Solis, J. M. Taboada, F. Obelleiro, and L. Landesa, "Optimization of an optical wireless nanolink using directive nanoantennas," *Optics Express*, vol. 21, pp. 2369–2377, Jan. 2013.

[8] Q. L. Y. Yang and M. Qiu, "Broadband nanophotonic wireless links and networks using on-chip integrated plasmonic antennas," *Scientific Reports*, vol. 6, Jan. 2016.

[9] A. Kinkhabwala, Z. Yu, S. Fan, Y. Avlasevich, K. Müllen, and W. Moerner, "Large single-molecule fluorescence enhancements produced by a bowtie nanoantenna," *Nature Photonics*, vol. 3, pp. 654–657, Oct. 2009.

[10] T. Lohmüller, L. Iversen, M. Schmidt, C. Rhodes, H.-L. Tu, W.-C. Lin, and J. Groves, "Single molecule tracking of supported membranes with arrays of optical nanoantennas," *Nano Letters*, vol. 12, pp. 1717–1721, Feb. 2012.

[11] K. Crozier, W. Zhu, D. Wang, S. Lin, M. Best, and J. Camden, "Plasmonics for surface enhanced raman scattering: nanoantennas for single molecules," *IEEE Journal of Selected Topics in Quantum Electronics*, vol. 20, pp. 152–162, May 2014.

[12] M. Alavirad, L. Roy, and P. Berini, "Optimization of plasmonic nanodipole antenna arrays for sensing applications," *IEEE Journal of Selected Topics in Quantum Electronics*, vol. 20, pp. 7–14, May 2014.

[13] Y. Wu, L. Li, and B. Liu, "Gold bow-tie shaped aperture nanoantenna: Wide band near-field resonance and far-field radiation," *IEEE Transactions on Magnetics*, vol. 46, pp. 1918–1921, Jun. 2010.

[14] H. İbili, S. Güler, B. Karaosmanoğlu, and Ö. Ergül, "Penetrable numerical modeling of metallic nanoparticles at terahertz frequencies," in *2018 Progress in Electromagnetics Research Symposium (PIERS)*, (Toyama, Japan), Aug. 2018.

[15] A. D. Rakić, A. B. Djurivsić, J. M. Elazar, and M. L. Majewski, "Optical properties of metallic films for vertical-cavity optoelectronic devices," *Applied Optics*, vol. 37, pp. 5271–5283, Aug. 1998.

[16] B. Karaosmanoğlu, A. Yılmaz, and Ö. Ergül, "A comparative study of surface integral equations for accurate and efficient analysis of plasmonic structures," *IEEE Transactions on Antennas and Propagation*, vol. 65, pp. 3049–3057, Jun. 2017.

[17] S. M. Rao, D. R. Wilton, and A. W. Glisson, "Electromagnetic scattering by surfaces of arbitrary shape," *IEEE Transactions on Antennas and Propagation*, vol. 30, pp. 409–418, May 1982.

[18] Ö. Ergül and L. Gürel, *The Multilevel Fast Multipole Algorithm (MLFMA) for Solving Large-Scale Computational Electromagnetics Problems*. Wiley-IEEE, 2014.

[19] Ö. Ergül, G. Işıklar, İ. Çetin, and M. Algun, "Design and analysis of nanoantenna arrays for imaging and sensing applications at optical frequencies," *Advanced Electromagnetics*, vol. 8, pp. 18–27, Feb. 2019.

[20] D. P. Fromm, A. Sundaramurthy, P. J. Schuck, G. Kino, and W. E. Moerner, "Gap-dependent optical coupling of single "bowtie" nanoantennas resonant in the visible," *Nano Letters*, vol. 4, pp. 957–961, 2004.

[21] G. Işıklar and Ö. Ergül, "Computational analysis of nanoantenna arrays for nanoparticle detection," in *2019 IEEE International Conference on Microwaves, Antennas, Communications and Electronic Systems (COMCAS)*, pp. 1–2, Nov. 2019.

[22] M. Estevez, M. Otte, B. Sepulveda, and L. Lechuga, "Trends and challenges of refractometric nanoplasmonic biosensors: a review," *Analytica Chimica*, vol. 806, pp. 55–73, Jan. 2014.

[23] L. Guo, J. A. Jackman, H.-H. Yang, P. Chen, N.-J. Cho, and D.-H. Kim, "Strategies for enhancing the sensitivity of plasmonic nanosensors," *Nano Today*, vol. 10, pp. 213–239, Apr. 2015.

[24] G. Işıklar, M. Algun, and Ö. Ergül, "Improved nano-optical traps for single-particle sensing applications," in *2019 Photonics Electromagnetics Research Symposium*, pp. 3626–3633, 2019.

[25] A. J. Poggio and E. K. Miller, "Integral equation solutions of three-dimensional scattering problems," in *Computer Techniques for Electromagnetics* (R. Mittra, ed.), ch. 4, pp. 159–264, Oxford: Pergamon Press, 1973.

[26] Y. Chang and R. F. Harrington, "A surface formulation for characteristic modes of material bodies," *IEEE Transactions on Antennas and Propagation*, vol. 25, pp. 789–795, Nov. 1977.

[27] T. K. Wu and L. L. Tsai, "Scattering from arbitrarily-shaped lossy dielectric bodies of revolution," *Radio Science*, vol. 12, pp. 709–718, Sep.-Oct. 1977.

[28] P. Ylä-Oijala, M. Taskinen, and S. Järvenpää, "Surface integral equation formulations for solving electromagnetic scattering problems with iterative methods," *Radio Science*, vol. 40, Nov. 2005.

[29] P. Ylä-Oijala and M. Taskinen, "Application of combined field integral equation for electromagnetic scattering by dielectric and composite objects," *IEEE Transactions on Antennas and Propagation*, vol. 53, pp. 1168–1173, Mar. 2005.

[30] K. Cools, F. P. Andriulli, and E. Michielssen, "A Calderón multiplicative preconditioner for the PMCHWT integral equation," *IEEE Transactions on Antennas and Propagation*, vol. 59, pp. 4579–4587, Dec. 2011.

[31] W. C. Gibson, *The Method of Moments in Electromagnetics*. Boca Raton: Chapman and Hall/CRC, 2007.

[32] R. F. Harrington, *Field Computation by Moment Methods*. New York: Macmillan, 1968.

[33] R. Coifman, V. Rokhlin, and S. Wandzura, "The fast multipole method for the wave equation: a pedestrian prescription," *IEEE Antennas and Propagation Magazine*, vol. 35, pp. 7–12, Jun. 1993.

[34] J. Song, C.-C. Lu, and W. C. Chew, "Multilevel fast multipole algorithm for electromagnetic scattering by large complex objects," *IEEE Transactions on Antennas and Propagation*, vol. 45, pp. 1488–1493, Oct. 1997.

[35] P. B. Johnson and R. W. Christy, "Optical constants of the noble metals," *Physical Review B*, vol. 6, pp. 4370–4379, Dec. 1972.

[36] Ö. Ergül and L. Gürel, "Discretization error due to the identity operator in surface integral equations," *Computer Physics Communications*, vol. 180, p. 1746–1752, Oct. 2009.

[37] D. Goldberg, *Genetic Algorithms in Search, Optimization, and Machine Learning*. Artificial Intelligence, Addison-Wesley, 1989.

[38] Y. Rahmat-Samii and E. Michielssen, *Electromagnetic Optimization by Genetic Algorithms*. Wiley, 1999.

[39] M. Ono, E. Kuramochi, G. Zhang, H. Sumikura, Y. Harada, D. Cox, and M. Notomi, "Nanowire-nanoantenna coupled system fabricated by nanomanipulation," *Opt. Express*, vol. 24, pp. 8647–8659, Apr. 2016.

[40] O. L. Muskens, V. Giannini, J. A. Sánchez-Gil, and J. Gómez Rivas, "Strong enhancement of the radiative decay rate of emitters by single plasmonic nanoantennas," *Nano Letters*, vol. 7, no. 9, pp. 2871–2875, 2007.

[41] H. Fischer and O. J. F. Martin, "Engineering the optical response of plasmonic nanoantennas," *Opt. Express*, vol. 16, pp. 9144–9154, Jun. 2008.

[42] J. L. Stokes, Y. Yu, Z. H. Yuan, J. R. Pugh, M. Lopez-Garcia, N. Ahmad, and M. J. Cryan, "Analysis and design of a cross dipole nanoantenna for fluorescence-sensing applications," *J. Opt. Soc. Am. B*, vol. 31, pp. 302–310, Feb. 2014.

[43] M. Hussein, N. Fayez, M. Hameed, and S. Obayya, "Design of flower-shaped dipole nano-antenna for energy harvesting," *IET Optoelectronics*, vol. 8, pp. 167–173, Aug. 2014.

[44] L. Lin and Y. Zheng, "Optimizing plasmonic nanoantennas via coordinated multiple coupling," *Scientific Reports*, vol. 5, Oct. 2015.

[45] A. Weber-Bargioni, A. Schwartzberg, M. Schmidt, B. Harteneck, D. Ogletree, P. Schuck, and S. Cabrini, "Functional plasmonic antenna scanning probes fabricated by induced-deposition mask lithography," *Nanotechnology*, vol. 21, p. 065306, Feb. 2010.